

論文 / 著書情報  
Article / Book Information

題目(和文)	
Title(English)	Particle Preparation using Electrical Discharge in Liquid Nitrogen
著者(和文)	ParkYoon Sik
Author(English)	Yoon Sik Park
出典(和文)	学位:博士(工学), 学位授与機関:東京工業大学, 報告番号:甲第12066号, 授与年月日:2021年9月24日, 学位の種別:課程博士, 審査員:関口 秀俊,久保内 昌敏,下山 裕介,森 伸介,青木 才子
Citation(English)	Degree:Doctor (Engineering), Conferring organization: Tokyo Institute of Technology, Report number:甲第12066号, Conferred date:2021/9/24, Degree Type:Course doctor, Examiner:,,,,,
学位種別(和文)	博士論文
Type(English)	Doctoral Thesis

Doctoral Thesis Academic Year 2021

**Particle Preparation using Electrical Discharge  
in Liquid Nitrogen**

Yoon Sik Park

Supervisor

Professor Hidetoshi Sekiguchi

**Department of Chemical Engineering  
Graduate School of Science and Engineering  
Tokyo Institute of Technology**

# CONTENTS

<b>CHAPTER 1 INTRODUCTION</b>	<b>1</b>
1.1 Plasma	2
1.1.1 Classification of plasmas	2
1.1.2 Generation of plasma	4
1.1.3 Arc discharge plasma	5
1.1.3.1 Voltage-Current Characteristic of DC discharge	5
1.1.3.2 Characteristic of arc discharge plasma	7
1.1.3.3 Classification of arc plasma by pressure	8
1.2 Plasma in liquid	9
1.3 Particle preparation using in-liquid plasma	11
1.4 Motivation	13
1.5 Objectives and research approach	14
1.6 Structure of this thesis	15
<b>Chapter 2 An Experimental study on submerged electrical discharge in deionized water</b>	<b>18</b>
2.1 Introduction	19
2.2 Experimental	19
2.2.1 Particle preparation using submerged discharge in deionized water	19
2.2.2 Characterization	22
2.3 Results and discussion	23
2.3.1 Morphology of the prepared particles in deionized water discharge	23
2.3.2 Chemical composition of a prepared particle in deionized water discharge	28
2.3.2.1 SAED pattern	28
2.3.2.2 XPS analysis	29
2.3.3 Formation mechanism of CuO nanoparticles in deionized water discharge	31

2.4 Summary	36
-------------	----

### **Chapter 3 Effect of power supplies on particle preparation using liquid nitrogen discharge** **38**

3.1 Introduction	39
3.2 Experimental	39
3.2.1 Preparation of Cu particles using AC transformer in liquid nitrogen discharge	39
3.2.2 Preparation of Cu particles using bipolar pulse power supply in liquid nitrogen discharge	41
3.2.3 Preparation of Cu particles using DC power supply in liquid nitrogen discharge	44
3.2.4 Experiment procedure in liquid nitrogen discharge	47
3.2.5 Characterization	47
3.3 Results and discussion	48
3.3.1 Morphologies of the prepared particles in liquid nitrogen discharge	48
3.3.2 Crystallite phase of the synthesized particles	59
3.3.3 Formation phenomena of Cu/CuO/Cu <sub>2</sub> O composite in liquid nitrogen discharge	61
3.4 Summary	65

### **Chapter 4 Variation in metal electrodes for the particle preparation using liquid nitrogen discharge** **66**

4.1 Introduction	67
4.2 Experimental	67
4.2.1 Experimental setup	67
4.2.2 Materials and method	68
4.2.3 Characterization	71
4.3 Results and discussion	72
4.3.1 Synthesis of Al/AlN particles	72
4.3.1.1 Morphologies of the prepared Al-based nanoparticles	72



4.3.1.2 Crystallite phase of the synthesized Al/AlN particles	76
4.3.2 Synthesis of TiN particles	78
4.3.2.1 Morphologies of the prepared Ti-based nanoparticles	78
4.3.2.2 Crystallite phase of the synthesized TiN particles	83
4.3.3 Synthesis of Zn/ZnO/Zn <sub>3</sub> N <sub>2</sub> particles	86
4.3.3.1 Morphologies of the prepared Zn-based nanoparticles	86
4.3.3.2 Crystallite phase of the synthesized Zn/ZnO/Zn <sub>3</sub> N <sub>2</sub> particles	89
4.3.4 Particle preparation using different electrode combinations	91
4.3.4.1 Morphologies of the prepared particles	91
4.3.4.2 Crystallite phase of the synthesized particles	93
4.3.4.3 Generation ratio of the produced particle	97
4.4 Summary	102
<b>Chapter 5 Mechanism of particle formation</b>	<b>105</b>
5.1 Introduction	106
5.2 Thermodynamic approach to the nitridation	106
5.2.1 Analysis	106
5.2.2 Gibbs standard free energy calculation	107
5.3 Sustainable arc discharge for stable particle preparation process	108
5.4 Particle formation mechanism	112
5.4.1 Surface morphologies of Al, Cu, Ti, and Zn electrode	112
5.4.2 Formation phenomena of synthesized particles in liquid nitrogen discharge	119
5.5 Summary	122
<b>Chapter 6 Conclusions</b>	<b>123</b>
<b>References</b>	<b>127</b>
<b>Acknowledgements</b>	<b>137</b>

# LIST OF FIGURES

Figure 1–1. Classification of plasmas [16].....	3
Figure 1–2. Generation of artificial plasma .....	4
Figure 1–3. Voltage-current characteristic of the DC electrical discharge [19] .....	6
Figure 1–4. Applications of plasma in solid, gas, and liquid [20].....	11
Figure 1–5. Illustration of nitrogen triple bond .....	13
Figure 1–6. Schematic of the structure of thesis.....	17
Figure 2–1. Schematic diagram of the reactor using a bipolar pulse power supply (upper) and actual picture of the experimental setup (bottom).....	20
Figure 2–2. FE–SEM images of (a) PLP and (b) PHP. ....	23
Figure 2–3. TEM images of (a, b, c) PLP and (d, e, f) PHP .....	25
Figure 2–4. Particle size distribution obtained from TEM images; (a) PLP, (b) PHP	27
Figure 2–5. Diffraction patterns of (a) PLP and (b) PHP both corresponding to copper oxide.....	28
Figure 2–6. Cu2p spectra of the electrode after discharging at (a) the low power mode and (b) the high power mode analyzed by XPS.....	30
Figure 2–7. Surface morphologies of the electrode (a) before discharging and after discharging at (b) the low–power mode and (c) the high–power mode...	32
Figure 2–8. The supposed mechanism for the generation of CuO nanoparticles at (a) the low–power mode.....	33
Figure 2–9. The supposed mechanism for the generation of CuO nanoparticles at (b) the high–power mode.....	34
Figure 3–1. Schematic diagram of the experimental using an AC step–up transform (upper) and actual picture of the apparatus (bottom).....	40
Figure 3–2. Schematic diagram of the reactor using a bipolar pulse power supply (upper) and actual picture of the experimental setup (bottom).....	42
Figure 3–3. Voltage and current waveform of plasma generated by AC 50 Hz (left) and bipolar pulse with 20 kHz (right) .....	43
Figure 3–4. Illustration of in–liquid arc plasma reactor using DC power supply.....	45
Figure 3–5. A picture of the experimental setup for particle preparation using DC in liquid nitrogen.....	46

Figure 3–6. FE–SEM images of the particles prepared by AC power. SU4300: (a) x1,500; (b) x5,000 .....	51
Figure 3–7. FE–SEM images of the particles prepared by DC power. 7500F: (a, b) DC 5 A, (c, d) DC 30 A, SU9000: (e, f) DC 5 A, (g, h) DC 30 A. The inserted figure in the yellow circle part is the low magnification image of the (e) and (g), respectively.....	52
Figure 3–8. FE–SEM images of the particles prepared by bipolar pulse power. SU4300: (a) 9 kV, 20 kHz, (b) 9 kV, 60 kHz .....	53
Figure 3–9. Particle size distribution of prepared Cu particle in liquid nitrogen discharge by a) AC, b) DC 5 A and c) DC 30 A.....	54
Figure 3–10. TEM images (a, b) and SAED patterns (c) of liquid nitrogen discharge sample in the operating condition of 9 kV, 20 kHz .....	56
Figure 3–11. TEM images (a, b) and SAED patterns (c) of liquid nitrogen discharge sample in the operating condition of 9 kV, 40 kHz .....	57
Figure 3–12. TEM images (a, b) and SAED patterns (c) of liquid nitrogen discharge sample in the operating condition of 9 kV, 60 kHz .....	58
Figure 3–13. XRD patterns of samples treated by DC power. (a) Cu raw material (electrode surface), (b) Cu treated by DC 5 A, (c) Cu treated by DC 30 A samples. The inserted figure is the PDF card of the Cu XRD patterns in the range of $2\theta = 10^\circ\sim 80^\circ$ . Individual crystalline phases are represented by the following characteristic peaks. (■: Cu, ○: CuO, □: Cu <sub>2</sub> O) .....	60
Figure 3–14. Surface structure change of Cu electrodes after discharge by AC and bipolar pulse power.....	63
Figure 3–15. Surface structure change of Cu electrodes after discharge by DC 30 A	64
Figure 4–1. Pictures of the prepared samples. (a) Coarse particles from liquid nitrogen discharge using DC power, (b) Some samples of fine particles dispersed and collected by ethanol, (c) debris .....	69
Figure 4–2. FE–SEM images of Al–based nanoparticles without osmium coating (a, b) low current mode, Al 5 A, and (c, d) high current mode, Al 30 A.....	73
Figure 4–3. FE–SEM images of Al–based nanoparticles with osmium–coated sample. (a, b) the low current mode, Al 5 A, and (c, d) high current mode, Al 30 A.....	74

Figure 4–4. Particle size distribution of prepared Al–based nanoparticles, (a) low current mode, Al 5 A, and (b) high current mode, Al 30 A .....	75
Figure 4–5. X–ray diffraction patterns of synthesized samples. (a) Al raw material (b) Al 5 A, (c) Al 15 A, (d) Al 30 A, (●) AlN, (■) Al.....	77
Figure 4–6. FE–SEM images of prepared Ti–based nanoparticles. (a, b) the low current mode, Ti 5 A, and (c, d) high current mode, Ti 30 A .....	79
Figure 4–7. FE–SEM images of prepared Ti–based nanoparticles. (a, b) the low current mode, Ti 5 A, and (c, d) high current mode, Ti 30 A .....	80
Figure 4–8. FE–SEM images (left) and EDS mapping images of the prepared samples. Low current mode, Ti 5 A (upper) and high current mode, Ti 30 A (bottom).....	81
Figure 4–9. Particle size distribution of Ti–based nanoparticles, (a) low current mode, Ti 5 A, and (b) high current mode, Ti 30 A.....	82
Figure 4–10. X–ray diffraction patterns of prepared samples. (a) Ti raw material, (b) Ti 5 A, (c) Ti 15 A, (d) Ti 30 A, (●) TiN, (■) TiN <sub>0.76</sub> , (○) TiO <sub>2</sub> , (□) α–TiN <sub>0.3</sub> .....	85
Figure 4–11. FE–SEM images of prepared Zn–based nanoparticles. (a, b) the low current mode, Zn 5 A, and (c, d) high current mode, Zn 30 A .....	87
Figure 4–12. FE–SEM images of prepared Zn–based nanoparticles. (a, b) the low current mode, Zn 5 A, and (c, d) high current mode, Zn 30 A .....	88
Figure 4–13. X–ray diffraction patterns of prepared samples. (a) Zn raw material, (b) Zn 5 A, (c) Zn 15 A, (d) Zn 30 A, (●) Zn <sub>3</sub> N <sub>2</sub> , (■) Zn, (□) ZnO.....	90
Figure 4–14. The morphology and size of the prepared particles. (a) Ti–Cu, and (b) Cu–Ti .....	92
Figure 4–15. X–ray diffraction patterns of the Ti–Cu sample. (a) Ti electrode raw material, (b) Ti–Cu 30 A, (●) TiN, (○) TiO <sub>2</sub> , (□) α–TiN <sub>0.3</sub> .....	94
Figure 4–16. Melted copper electrode after the 30A reaction (a) Ti–Ti, (b) Cu–Cu, (c) Ti–Cu, (d) Cu–Ti, and (f) Cu–Ti before cutting the melting part.....	95
Figure 4–17. X–ray diffraction patterns of the Cu–Ti sample. (a) Cu electrode raw material, (b) Cu–Ti 30 A, (■) Cu .....	96
Figure 4–18. Dendrite structure of the coarse particle and debris. ....	98
Figure 4–19. Illustration of the arc discharge mechanism in this reaction .....	99

Figure 5–1. Gibbs standard free energy for synthesizing nitrides from Al, Ti, and Zn electrodes .....	108
Figure 5–2. Linear function of minimum current density for stable arc discharge and the relationship between temperature and work function. Individual sphere mark indicates thermionic emission at a work function, and the color describes the boiling or melting point of the materials.....	111
Figure 5–3. After the reaction, the titanium electrode was covered with the golden or yellowish color of titanium nitride.....	112
Figure 5–4. Al particle forming on the anode surface (a), (b), (c), Al coarse particle (d), (e), and Al fine particle (f), (g).....	115
Figure 5–5. Cu particle forming on the anode surface (a), (b), (c), Cu coarse particle (d), (e), and Cu fine particle (f), (g).....	116
Figure 5–6. Ti particle forming on the anode surface (a), (b), (c), Ti coarse particle (d), (e), (f), and Ti fine particle (g), (h), (i).....	117
Figure 5–7. Zn particle forming on the anode surface (a), (b), (c), Zn coarse particle (d), (e), and Zn fine particle (f), (g), (h).....	118
Figure 5–8. Mechanism of the nitride particle formation .....	120
Figure 5–9. Illustration of the particle formation in the submerged arc discharge process.....	121

# LIST OF TABLES

Table 1–1. Plasma parameters of non-thermal and thermal arc discharges [19].	6
Table 1–2. Comparison of glow and arc discharge [17].	13
Table 2–1. Detailed operating conditions for preparation of Cu particles.	21
Table 2–2. Specification and physical properties of copper	21
Table 3–1. Detailed operating conditions for preparation of Cu particles.	43
Table 3–2. Average particle size and standard deviation of prepared Cu particles depending on the AC and DC power supply	55
Table 4–1. Experimental conditions	68
Table 4–2. Specification and physical properties of the electrode materials.	70
Table 4–3. Physical properties of the nitride materials and their applications [81–90]	70
Table 4–4. Average particle size and standard deviation of prepared Al–based particles depending on the current mode	76
Table 4–5. Average particle size and standard deviation of prepared Ti–based particles depending on the current mode	81
Table 4–6. Lattice parameter and nitrogen content of TiN samples.	86
Table 4–7. Particle generation ratio and loss of the particle formation process	100
Table 4–8. Summary of characteristic observation on the prepared particle in this study	102
Table 5–1. The crystalline phase of the synthesized particle.	107

# **CHAPTER 1**

## **Introduction**

## 1.1 Plasma

Plasma is considered the ionized gas, widely known as the fourth state of matter, followed by solid, liquid, and gas [1, 2]. It consists of a mixture of electrons, ions, and neutral species. Due to the electrons and ions existing in plasma, plasma is electrically conductive. However, plasma is still neutral because of the balance between negative and positive charges [3].

Ionized gas can be easily obtained when the source of free electron is dominant with supplying energy. The free electrons can be generated by supplying heat energy or a high electrical field. The electrons are accelerated by high voltage and move from cathode to anode. Then some accelerated electrons collide with gas molecules. When a colliding electron has enough energy to ionize gas molecules, the molecule is dissociated to electron and heavy particles (ion, radical). Newly generated electrons move forward to the anode, colliding with other molecules again, which eventually leads to the ionization process [4]. Plasma can be sustained if there is a continuous source of energy to maintain the required degree of ionization. The degree of ionization of plasma is the proportion of electron density ( $n_e$ ) to that of the gas ( $n$ ). And this is mostly affected by the change in the temperature. It can vary from 100% (fully ionized gases) to low values (e.g.,  $10^{-4}$ – $10^{-6}$ ; partially ionized gases) [5].

Nowadays, there are many applications using plasmas in daily life to the industrial levels, such as fluorescent lamps, neon signs, welding, display panel, toxic gas and wastewater treatment, functional material surface treatment, semiconductor integrated circuit processing, nuclear fusion power generation [6–8].

### 1.1.1 Classification of plasmas

Plasma can be divided into two groups, thermal plasma (equilibrium) and non-thermal (non-equilibrium) plasma [2]. Thermal plasma is an equilibrium state, which means that



electrons, ions, and neutrals are nearly at the same temperature. Generally, a high temperature or high pressure is required for thermal (equilibrium) plasma. Thermal plasma has a higher temperature ( $>10^4$  K) and higher reactivity than non-thermal (non-equilibrium) plasma [1, 9]. The typical applications of thermal plasma are the synthesis of fine particles and the decomposition of pollutants [10–12].

On the other hand, non-thermal plasma is not in an equilibrium state, which means that the temperatures of the electrons, ions, and neutral species are different. Electron temperature is much higher than heavy particles (ions, atoms, molecules). Applications of non-thermal plasma are etching, deposition, surface modification, and the treatment of heat-sensitive material, including polymers and biomaterials [13–15].

Electron density, electron temperature, and pressure are important factors to determine the properties of plasma. The classification of plasmas as a function of electron density and electron temperature is shown in Figure 1–1 [16, 21]. The electron density is related to the ionization degree, which is a ratio of the density of charged species to that of neutral gas. The plasma with the ionization degree close to unity is called completely ionized plasma, such as the Sun and nuclear fusion plasma. The plasma with the low ionization degree called weakly ionized plasma is focused on industrial application.

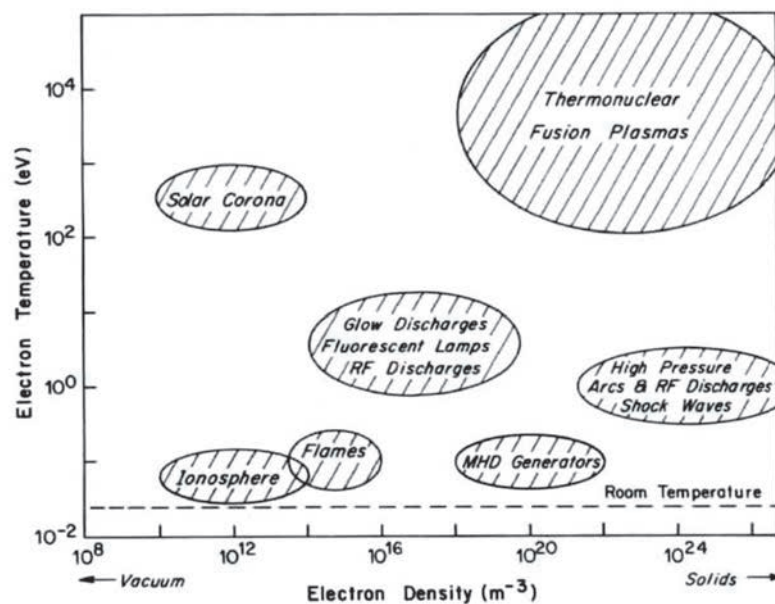


**Figure 1–1.** Classification of plasmas [16]

### 1.1.2 Generation of plasma

The artificial plasma generation method can be varied with the conditions such as plasma temperature, density, ionization, and ion type [17]. Also, depending on the dielectric material state (gas, liquid, or solid), the generation method is changing. In general, plasma is generated through a gas state, so solid metal is made into a metal vapor by heating [18]. The electrical discharge method is a widely using technic to generate plasma. When an electrical breakdown of the gas is performed, it can be primarily classified by the power supplies (DC, low–frequency, high–frequency, microwave, pulse). Figure 1–2 summarizes the plasma generation methods.

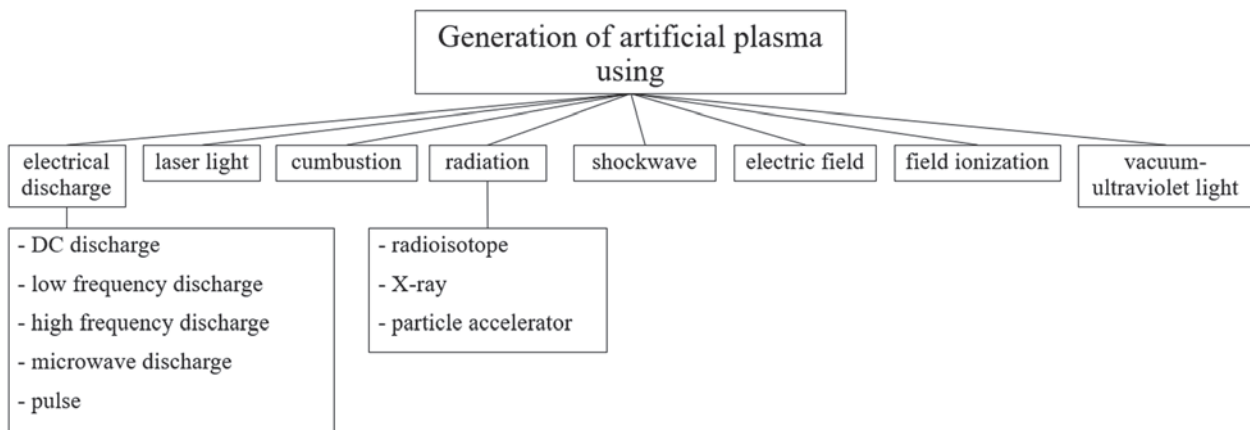


**Figure 1–2.** Generation of artificial plasma

In DC discharge, a DC voltage is applied between electrodes. Thermal electrons (thermion) or photoelectrons emitted from the cathode are accelerated in a DC electric field and ionized by colliding with neutral atoms and molecules to generate plasma.

Low–frequency discharge generates plasma by applying AC power of 50 Hz to 100 kHz between electrodes. Ionizing electrons emitted from the electrodes in an AC electric field collide with neutral atoms and molecules. The effect of low–frequency on the motion of electrons does not appear significantly. Thus, the discharge mechanism in the low–frequency range can be considered in the same way as in DC discharge [17].

In high-frequency discharge, an alternating voltage of about 10 MHz to 100 MHz is applied between the electrodes to generate plasma.

Microwave discharge generates plasma by applying a microwave in a frequency range of more than 1 GHz between electrodes or resonators.

### **1.1.3 Arc discharge plasma**

#### **1.1.3.1 Voltage–Current Characteristic of DC discharge**

Before explaining the arc, the transition step of glow discharge to arc discharge is described in Figure 1–3 [19]. In general, the cathode fall from townsend discharge to the glow discharge is quite large and has been reported to be about 200–300 V [17]. As the positive ions pass through the first cathode voltage drop region (E→F), only part of the energy is spent on secondary electron emission, while the other part serves to heat the cathode. In an abnormal glow discharge (G→H), the voltage and current increase together, causing severe cathode heating and resulting in thermal electron emission. Once the thermal electron emission begins, the current density rises rapidly, and the current also gathers and gradually raises the temperature of the local part of the cathode. As a result, the cathode is heated by the discharge current itself, causing thermal electron emission to sustain the arc discharge [17]. In the illustration, the arc region can be described in three-part. The first part is glow to arc transition (H→I), which initiates the cathode's thermion emission. Next is the non-thermal arc area (H→I→J), when the discharge has stabilized to the I point. In this part, the low-intensity arc has an approximately 1~50 A and may operate in rare cases over this range. The last part is a thermal arc area (J→K). After the point J on the figure, between 20~50 A, the non-thermal arc transit into the thermal arc [19]. Parameters of non-thermal arc and thermal arc discharge are shown in Table 1–1 [19].

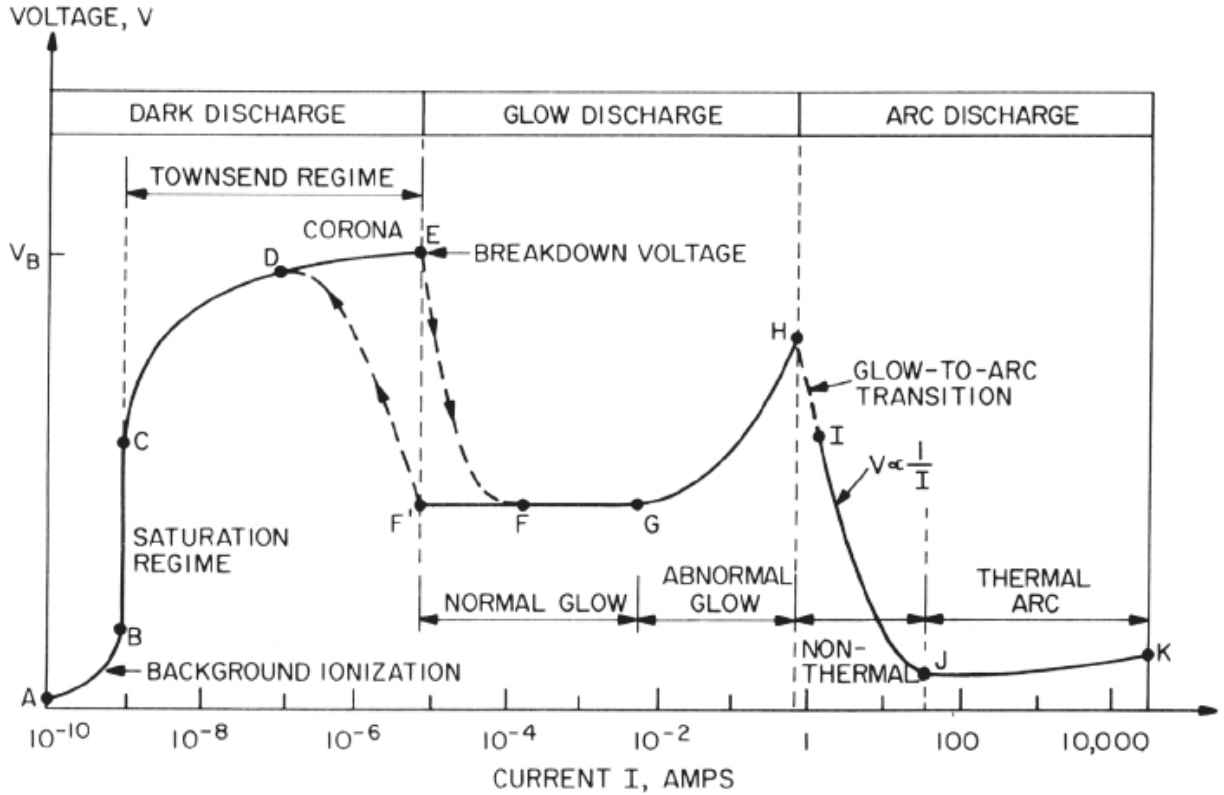


Figure 1-3. Voltage-current characteristic of the DC electrical discharge [19]

Table 1-1. Plasma parameters of non-thermal and thermal arc discharges [19]

Plasma parameter	Non-thermal arc	Thermal arc
Equilibrium state	Kinetic	LTE
Electron density, $n_e$ (electrons/m <sup>3</sup> )	$10^{20} < n_e < 10^{21}$	$10^{22} < n_e < 10^{25}$
Gas pressure, $p$ (Pa)	$0.1 < p < 10^5$	$10^4 < p < 10^7$
Electron temperature, $T'_e$ (eV)	$0.2 < T'_e < 2.0$	$1.0 < T'_e < 10$
Gas temperature, $T'_g$ (eV)	$0.025 < T'_g < 0.5$	$T'_g = T'_e$
Arc current, $I$ (A)	$1 < I < 50$	$50 < I < 10^4$
$E/p$ (V/m-Torr)	High	Low
$IE$ (kW/cm)	$IE < 1.0$	$IE > 1.0$
Typical cathode emission	Thermonic	Field
Luminous intensity	Bright	Dazzling
Transparency	Transparent	Opaque
Ionization fraction	Indeterminate	Saha equation
Radiation output	Indeterminate	LTE

### 1.1.3.2 Characteristic of arc discharge plasma

As explained above, increasing the current density at the cathode surface leads to a local area heating on the electrode surface, and metal evaporates eventually. Moreover, if the temperature rises sufficiently at the electrode, hot electrons are supplied for discharge. Even though a strong electric field is applied between the electrodes, the energy that electrons can obtain from the electric field is small because the average free path of electrons is short. Therefore, the ionization mechanism due to the collision of electrons cannot be considered, and thermal ionization is considered as the main mechanism as the temperature of gas molecules and atoms be the same as electrons [17].

When the temperature of the cathode becomes so high that the thermionic emission exceeds the discharge current, the cathode fall is almost eliminated, and arc discharge plasma, which has a lower holding voltage than the ionization voltage, can be obtained. This is called a low voltage arc discharge [17].

When the gas pressure is lowered in arc discharge, electron impact ionization becomes dominant as in glow discharge. As the pressure is lowered to a high vacuum, the evaporation material becomes ionized from the electrode to maintain the discharge. Such a plasma is often referred to as a vacuum arc plasma [17].

The arc discharge is mainly used for melting metals, welding, and arc furnace, etc., as the temperature of gas atoms and molecules, ions reaches 5,000~6,000 [K]. In addition, since the arc plasma is characterized by high luminance, it is used for photoelectric power [17].

When initialize the arc plasma following method is widely used in practical use. At first, in order to cause the local Joule heating at the electrode tip, both electrodes are placed in contact with each other without a gap. And then, arc discharge is generated by gradually increasing the distance between the two electrodes. This method is possible because the ignition voltage requires a high voltage to initiate the arc. However, a low voltage, around 10 V, is required for sustaining the discharge.

Arc discharge and glow discharge are distinguished not only according to the current magnitude but also according to the electron emission mechanisms at the cathode. Table 1–2 shows the comparison [17]. Two types of electrode emission mechanism are widely known as  $\alpha$ -process (ionizing gas molecules by a collision of an electron) and  $\gamma$ -process (emitting secondary electrons by a collision of ions).

**Table 1–2.** Comparison of glow and arc discharge [17]

	Glow discharge	Arc discharge
Cathode fall	200~300 [V]	the magnitude of the ionization voltage of the gas
V–I characteristics	slightly flat V-shaped	descent
Current density	low, $10^{-5}\sim 10^{-3}$ [A/cm <sup>3</sup> ]	high, $10^3\sim 10^7$ [A/cm <sup>3</sup> ]
Electron emission mechanism	$\gamma$ -process is main	except $\gamma$ other mechanism is dominant

### 1.1.3.3 Classification of arc plasma by pressure

Arc discharge can be divided into a low-pressure arc and a high-pressure arc by the gas pressure during discharge. In arc discharge, the boundary between low-pressure and high-pressure is not strict, but here, less than about 2 kPa is called low-pressure, and above about 2 kPa is called high-pressure. In low-pressure, arcs can be classified into hot cathode arcs, self-sustaining arcs, and cold cathode arcs caused by external overheating. The high-pressure arc is divided according to the stabilization method [17]. Among those, self-sustaining arc and cold cathode arcs are explained below.

The self-sustaining arc discharge is a discharge that occurs when a high-melting point material such as tungsten or carbon is used for the cathode. The current density of the cathode is

higher than in the case of external heating, and positive ions heat the cathode surface to generate thermionic emission, which leads to continuous arc discharge [17].

The cold cathode arc discharge is an arc discharge when a material with a low melting point or boiling point, such as mercury, zinc, or copper, is used for the cathode. An extremely high electric field (about  $10^7$  [V/cm]) is generated by the concentration and accumulation of positive ions near the surface of the cathode, and electrons are supplied by field emission to sustain the arc discharge [17].

In general, the high-pressure arc discharge plasma state is called a local thermal equilibrium plasma (LTE) and a state in which the electron temperature and the gas temperature are approximately the same. The mechanism follows thermal ionization. Since the temperature of the gas is extremely high, evaporation of the electrode material and convection of gas molecules occur violently, the arc discharge itself is unstable [17].

## 1.2 Plasma in liquid

As plasma is known for ionized gas, some people might think that plasma can be generated from the gas, not liquid and solid. However, the plasma can generate in liquid and solid [26]. Recently, there has been increasing interest in plasma under the liquid circumstance. Since around the 1980s, various studies have been conducted on in-liquid plasma, also referred to as a solution plasma. Many researchers are reported optimizing parameters such as types of liquids [27], electrode materials [28–31], types of plasmas, reactor and electrode geometries, pressure, temperature, density, composition, viscosity, and conductivity [20, 22], in plasma generation under the liquid.

Two methods are widely known for generating plasma in liquid. The key factor is a bubble, and the difference between the two methods is how to make a gas bubble near the electrode. The first one is initiated by the streamer. When it develops to corona discharge during the electrical breakdown of water, the bubbles are formed near the electrode, formed by a strong electric field or by heating from an electrode current [20, 23]. The electrical discharge under liquid occurs UV, shockwaves, localized heat, with active species such as radicals, ions, and

photons [24]. The second method is to generate bubbles by putting heating sources, by applying shock waves, or by supply gas line directly [32–33]. In both cases requires the electrical breakdown of the liquid, so a high-power supply is necessary for in-liquid plasma. In order to generate a streamer discharge underwater, it is reported that 50 to 400 kV of high voltage and a current of 100 A or more are required [20].

Generating method of in-liquid plasma can be classified into four types [20]. First is a direct discharge between two electrodes using AC power, second is a contact discharge of the electrolyte solution using DC power, third use radiofrequency or microwave irradiation, and the last one uses laser ablation. The direct discharge between two electrodes is a common method using many power sources. In the solution plasma, usually uses electrolytes for dielectric medium such as deionized water, ethanol, organic solvents, many organic metal precursors. It is essential to use a conductive medium.

In order to sustain the plasma in a liquid circumstance, many studies on the electrode using for the generation of plasma have been carried out. Tungsten, aluminum, copper, molybdenum, stainless steel, and carbon are used for the study [25]. For the continuous discharge, high melting points of the electrode, such as tungsten, withstand the longer time discharge compared to other electrodes.

Figure 1–4 shows the applications in liquid plasma. It can be broadly divided into two topics: material processing, including synthesis of nanoparticles, catalysts, and quantum dots. Next is an environmental, which is about wastewater treatment and sterilization for biomedical and agriculture purposes. In this study, material processing using plasma in liquid is related to our topic.



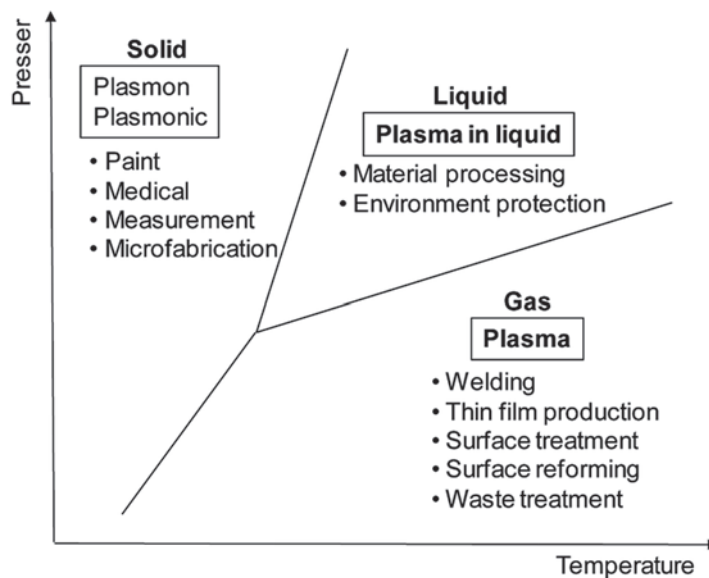


**Figure 1–4.** Applications of plasma in solid, gas, and liquid [20]

### 1.3 Particle preparation using in–liquid plasma

Nowadays, various plasma methods have been studied for the synthesis of nanoparticles. Among them, the liquid discharge has attracted a lot of attention owing to its novel properties of liquid–plasma interaction which are distinct from both gas discharge and traditional solution methods [34, 35].

Some researchers have adopted precursors which is soluble in liquid to obtain metal or metal oxide nanoparticles [36–42]. It has been reported that liquid–plasma interaction produces reducing agents, which enable faster and unique reduction of metal ions [43].

Other researchers have reported particle synthesis using electrodes as a raw material in liquid discharge [44–49]. Metal nanoparticles are obtained in solution with wire explosion method using Al, Ag, Au, Cu, Fe, Nb, Ni, , Mo, Ta, Ti, W, W–Re, Pt wire as an electrode [50–53]. The advantage of this method is a simple process. Various metal nanoparticles can be synthesized by changing electrode wire.

Especially, the application of arc discharge in which current over several amperes flows has been frequently reported in this field [54–56]. It is due to the generation of high temperature in arc discharge which can erode metal electrodes.

The existing researches have shown the synthesis of metal nanoparticles and oxide nanoparticles using in-liquid arc discharge. However, the use of electrolytes has been still required because it is difficult to generate stable arc discharge in a nonconductive liquid such as deionized water [49, 55] and liquid nitrogen [42, 43]. Although electrolyte has a significant role in determining phase composition or morphology of particles, introducing electrolyte makes the reaction complicated [54, 56–58].

In this study, liquid nitrogen was employed as a dielectric medium. In the previous researches, Fink et al. reported that the breakdown voltage of the liquid nitrogen under atmospheric pressure is about 50 kV/mm [59, 60]. It seems that a high voltage power supply is required for liquid nitrogen discharge. Toshitaka et al. investigated the effect of discharge behavior by changing the electrode material. As a product, they also obtained Al, Ti, V, Fe, Ni, Cu, Zr, Nb, Mo, Ta, and W micro-sized particles using a DC power supply [61]. Belmonte et al., reported synthesis of Cu, Ag, Pb, CoNi, ZnO, nanoparticles in liquid nitrogen medium using nano-pulse power supply [62–68]. Sano et al., presented synthesize Pt-supported carbon nanohorns for fuel cell electrode by arc plasma in liquid nitrogen [69]. Many studies have been reported synthesize carbon-based functional materials [70]. However, the particle generation mechanism in liquid arc discharge has not been completely investigated.

## 1.4 Motivation

The motivation of this study comes from the aim to further understand the arc discharge plasma in liquid nitrogen for particle preparation. We choose liquid nitrogen as a dielectric medium for two main expectations. Each of the advantages is very interesting as to conduct this scientific research.

The first reason is the temperature of the liquid nitrogen. We anticipated that the fast quenching of the particle might enable us to use it as a factor to control the particle growth in the early stage of nucleation and crystal growth. However, it is well known that the gas temperature of arc plasma is more than 5,000 K, and in some cases, the gas temperature is above 10,000 K. In this study, the vaporization temperature of liquid nitrogen used as a dielectric media as well as a coolant is 77 K (-196 °C), and the deionized water at room temperature, which is used for the purpose of comparison, is 296 K (23 °C). Considering this point, it is a slight difference compared to the gas temperature of arc plasma. However, only a few studies on using liquid nitrogen as a dielectric media it is still unknown and more studies were necessary for applied to the practical particle preparation.

The second reason is the inert characteristics of nitrogen. As in Figure 1–5, nitrogen itself has a triple bond, which means hard to break down the bond and hard to react with other materials. For this property, nitrogen is generally used as an inert and as an insulator system in industrial. In this aspect, liquid nitrogen is an attractive media for our study to investigate the particle formation mechanism and physical interaction between the arc discharge plasma without any other chemical reaction.



**Figure 1–5.** Illustration of nitrogen triple bond

## 1.5 Objectives and research approach

The purpose of this study is to investigate the specific features of the particles prepared by an electrical discharge under liquid nitrogen and to understand particle formation phenomena in liquid nitrogen discharge.

A synergy of rapid quenching of liquid nitrogen and plasma, which enables the fast synthesis of particles, was expected to improve the production of fine particles.

In this study, the dielectric media, power supply, and metal electrode were investigated to develop the particle preparation system in liquid nitrogen discharge. Also, we considered the effect of process parameters such as applied current and applied voltage related on the electrical discharge behaviors and particle formation. For comparison with the liquid nitrogen, submerged discharge in deionized water was conducted. In the liquid nitrogen discharge, AC, DC, and pulsed power supply were applied to optimize the preparation of the particle. Four kinds of metal electrodes, including aluminum (Al), copper (Cu), titanium (Ti), and zinc (Zn), were chosen as raw materials in this process.

We focus on the interaction between the synthesized particles and the plasma under liquid and discuss the particle formation phenomena based on the experimental results.

## 1.6 Structure of this thesis

In this study, we aim to investigate particle preparation using an electrical discharge in liquid nitrogen. According to the objectives, the thesis consists of six chapters as follows.

**Chapter 1 Introduction** explains the background of this study, plasma technology, previous research about solution plasma for particle preparation, motivation, objectives, and structure of the study. This chapter describes the basic concept of plasma and plasma under the liquid. Based on this background, the aim of this study is clarified.

**Chapter 2 An experimental study on submerged electrical discharge in deionized water** reports an experimental procedure of submerged electrical discharge in deionized water (DI water) for particle preparation. The DI water was selected as a dielectric media for preliminary study towards in-liquid plasma as well as a comparison with liquid nitrogen media. A bipolar pulse power supply was introduced in this chapter. The collected copper oxide particles were characterized with the scanning electron microscope (SEM), X-ray diffractometer (XRD), transmission electron microscope (TEM), and X-ray photoelectron spectroscopy (XPS) in order to investigate the surface morphologies and crystalline structure. The particle formation mechanism was suggested based on experimental results.

**Chapter 3 Effect of power supplies on Cu particle preparation using liquid nitrogen discharge** describes experimental setup using AC, DC, and bipolar pulsed power supplies. The particle production rate of copper and the particle size distribution depends on operating conditions are investigated with changing applied voltage and applied current. Effects of power characteristics and behavior on yield are discussed based on characterization results.

**Chapter 4 Variation in metal electrodes for particle preparation using liquid nitrogen discharge** studies the feasibility of this particle preparation process with different types of metal electrodes. An aluminum (Al), titanium (Ti), and zinc (Zn) electrode was used. In this

chapter, a DC power supply was applied for the experiment. The characteristics of prepared particles are investigated by changing applied current as a variable parameter. The effect of metal electrode configuration was discussed based on the experimental results and electrical discharge behavior.

**Chapter 5 Mechanism of Particle formation** deals with the synthesis of nitride fine particles. The interaction between metal electrodes and the behavior of arc plasma is discussed with the point of material physical properties and the stability of continuous discharge. The illustration of particle formation phenomena in liquid nitrogen discharge was proposed.

**Chapter 6 Conclusion** summarizes the results obtained from this study.

A schematic diagram in Figure 1–6. shows the structure of this thesis.

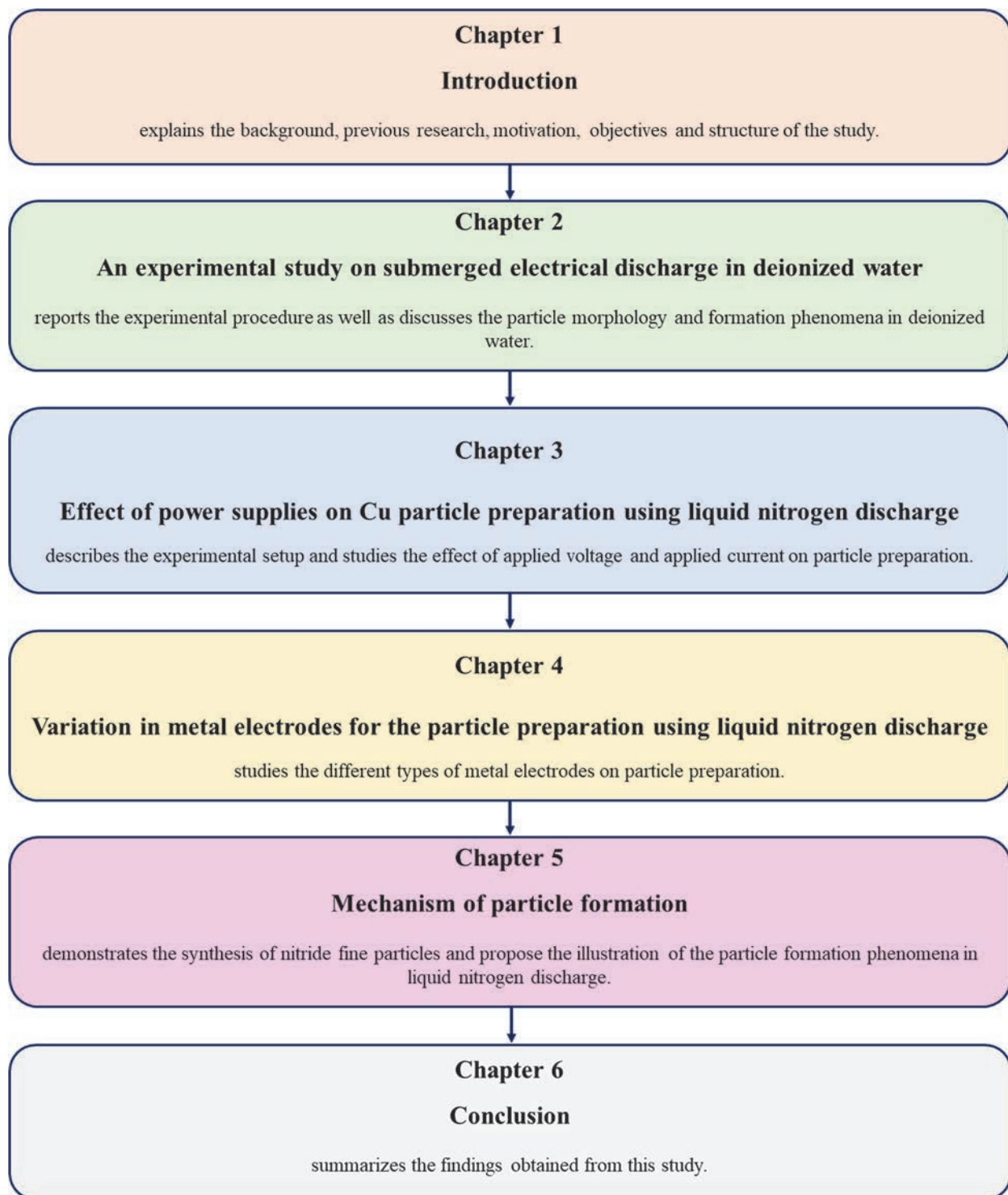


**Figure 1–6.** Schematic of the structure of thesis

# **CHAPTER 2**

## **An Experimental study on submerged electrical discharge in deionized water**



## 2.1 Introduction

In this chapter, particle preparation in deionized water (DI water) was conducted for a preliminary study concerning in-liquid plasma and a comparison study with liquid nitrogen. The copper electrode was chosen as the raw material. The particles were prepared by a submerged electrical discharge under DI water without any electrolyte. The electrochemical reaction could be simplified due to the absence of an electrolyte. Also, the particle formation mechanism in DI water will be discussed.

## 2.2 Experimental

### 2.2.1 Particle preparation using submerged discharge in deionized water

The experimental setup is shown in Figure 2–1 and Figure 2–2. The Electrical discharge was generated between copper rods (Nilaco Co., Japan) with a diameter of 3 mm, immersed in deionized water. The gap between the electrodes could be controlled using a micrometer and was maintained as 300  $\mu\text{m}$  for all experimental conditions. A Dewar-like flask was used for the container to minimize the heat transfer to the surroundings. A high voltage bipolar pulse power supply (Genius2, EN Technologies, Korea) was applied to generate electrical discharge in water. Two types of operating conditions were conducted called low- and high-power modes, respectively. The low-power mode was operated with a frequency of 20 kHz and applied voltage of 4 kV, and the high-power mode was operated with a frequency of 60 kHz and applied voltage of 9 kV. It is worth mentioning that the low-power mode and the high-power mode provided respectively the minimum and maximum operating power. Other operating parameters such as pulse on-time were maintained as same. The detailed operating conditions are summarized in Table 2–1, and the specification and physical properties of the copper electrode material are summarized in Table 2–2.

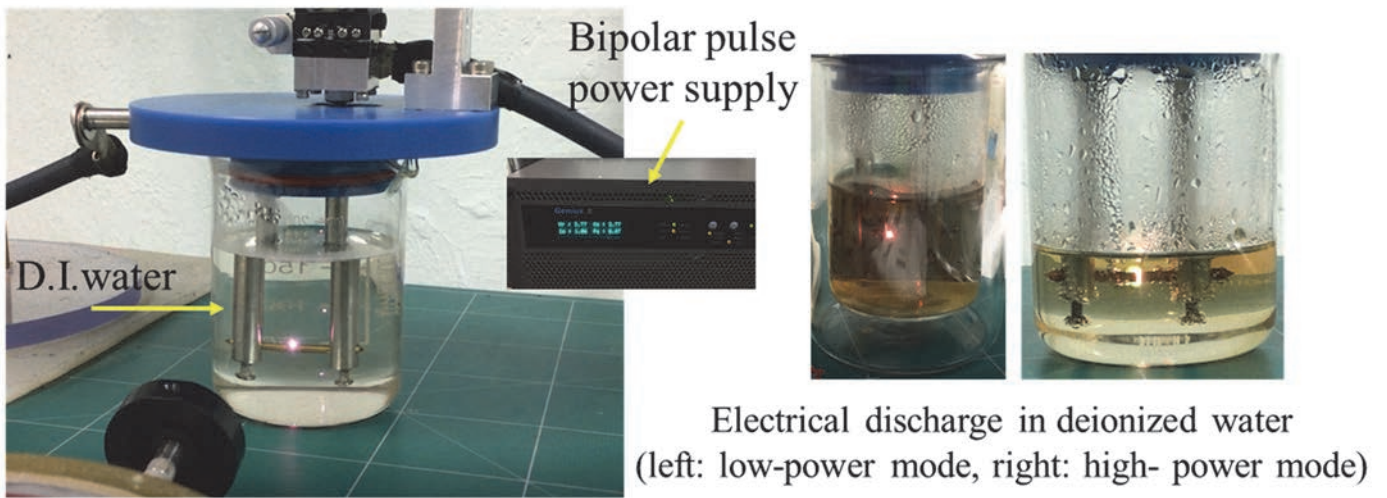
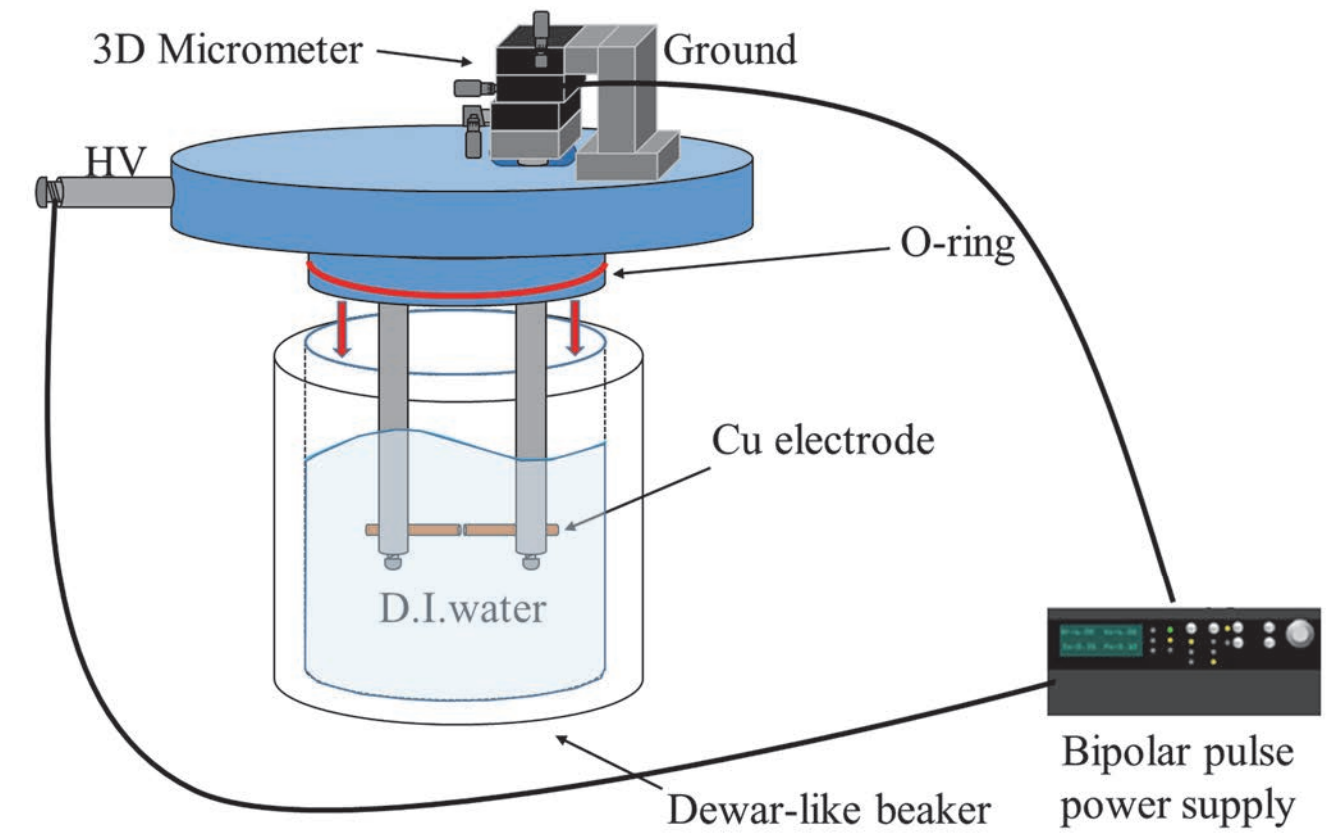


**Figure 2–1.** Schematic diagram of the reactor using a bipolar pulse power supply (upper) and actual picture of the experimental setup (bottom)

**Table 2–1.** Detailed operating conditions for preparation of Cu particles

Power supply	Bipolar pulse	
Dielectric medium	Deionized water	
Electrode material	Cu rod (>99.99, 3 $\phi$ )	
Applied voltage	4 kV	9 kV
Applied current	n/a	n/a
Frequency	20 kHz	60 kHz
Pulse on time	2.5 $\mu$ s	
Gap distance	300 $\mu$ m	
Gas flow rate	n/a	
Power Specification	$V_{\max}=10$ kV, $V_{PP}=20$ kV	
	Power up to 2 kW 20~60 kHz	

**Table 2–2.** Specification and physical properties of copper

Material	Cu
Rod diameter [mm]	3
Purity [%]	99.99
Crystal structure	fcc (Face-centered cubic)
Melting point [K]	1,357.77
Boiling point [K]	2,835
Heat of fusion [kJ/mol]	13.26
Heat of vaporization [kJ/mol]	300.4
Molar heat capacity [J/(mol·K)]	24.44
1 <sup>st</sup> Ionization energy [kJ/mol]	745.5
Thermal expansion [ $\mu$ m/(m·K)]	16.5
Thermal conductivity [W/(m·K)]	401

### 2.2.2 Characterization

During the discharge, the solution gradually started to have a brown color, as shown in Figure 2–1, which suggested nanoparticle formation. Thus, we used this solution for preparing the analysis sample.

The surface of the obtained particles and electrodes were observed with a field emission scanning electron microscope (FE–SEM, S–4300, Hitachi, Japan) for high magnification.

The morphologies of the synthesized particles were analyzed by a field emission transmission electron microscope (FE–TEM, JEM–2100F, Jeol Co.) operating with a voltage of 200 kV. The particles were dispersed in ethanol by ultrasound and then sampled on the copper grid for FE–TEM. The ethanol was completely removed by drying the grid for some days.

SAED (Selected area electron diffraction) was used to obtain information on the crystal structure of the prepared particles.

Eq (2–1) is called Bragg's equation where  $n$  is an integer determined by the order given,  $\lambda$  is the wavelength of the X–ray (for Cu  $K\alpha$ , 1.540598Å),  $d$  is a lattice spacing, and  $\theta$  is the angle between the incident ray and the scattering planes.

$$n\lambda = 2d \sin \theta \quad (2-1)$$

From Eq (2–2) and the data of the diameter of the diffraction ring of the sample, lattice distance “ $d$ ” could be obtained where  $L$  is a camera length,  $\lambda$  is a wavelength of the electrons,  $R$  is a radius of the diffraction ring, in this analysis,  $L\lambda$  is a camera constant (9.285nm<sup>2</sup>).

$$L\lambda = Rd \quad (2-2)$$

Using Eq (2–1) and the information of the  $d$ –value on the product material,  $2\theta$  could be calculated.

The chemical bonding state was investigated via an X-ray photoelectron spectroscopy (XPS, K-alpha, Thermo Scientific Co.). The X-ray of monochromatic Al-K $\alpha$  was employed for the measurement. The ranges of the measurement were from 927.5 to 960 eV for the Cu2p<sub>3/2</sub> peak and Cu2p<sub>1/2</sub> peak.

## 2.3 Results and discussion

### 2.3.1 Morphology of the prepared particles in deionized water discharge

The particles were synthesized in deionized water discharge under the low-power mode and the high-power mode named PLP and PHP. Figure 2-2 shows SEM images of PLP and PHP, respectively. The difference between PLP and PHP is observed from their morphologies. PLP (Figure 2-2, (a)) has needle-like morphologies while PHP (Figure 2-2, (b)) has a linked structure.

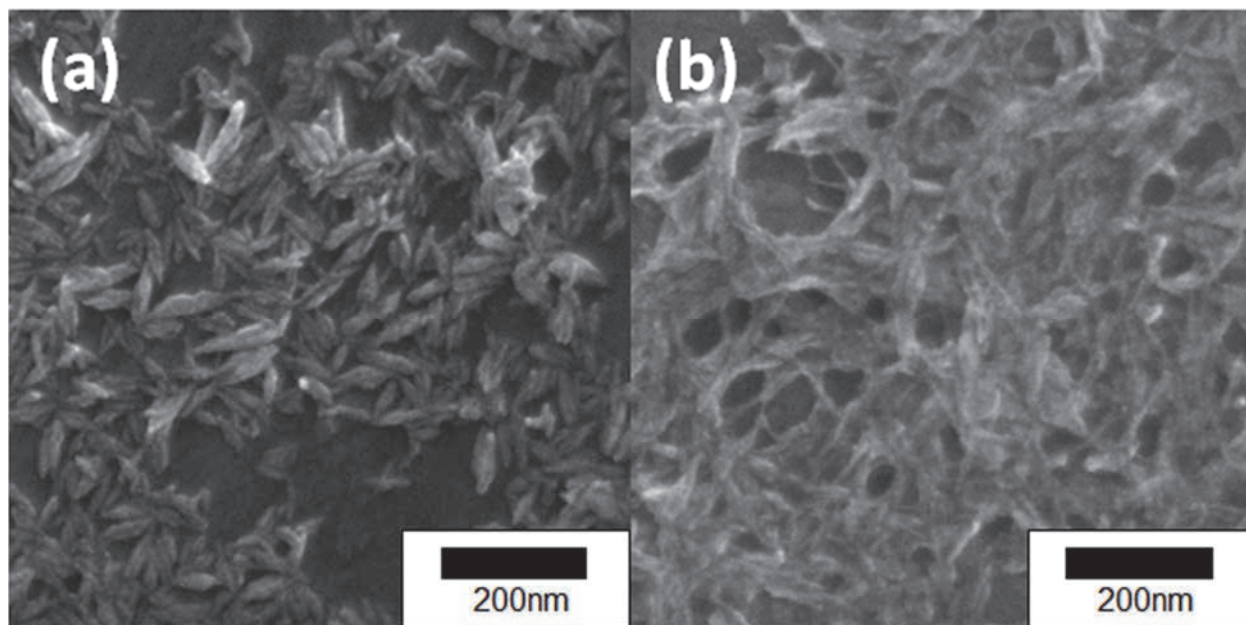


Figure 2-2. FE-SEM images of (a) PLP and (b) PHP

The morphologies of individual particles could also be observed from TEM images shown in Figure 2–3. Figure 2–3 (a) shows that the morphologies of PLP are almost the same as those observed from the SEM images. Meanwhile, the PHP in Figure 2–3 (b) shows distinctive morphologies compared to Figure 2–2 (b). It shows that the individual PHP has clipped nail–like morphologies. It seems that the aggregation of the individual clipped nail–like particles led to the formation of a linked structure.

The needle–shaped PLP particles are having straight body, and both ends are sharply pointed. On the other hand, the clipped nail–shaped PHP particles are slightly bend compared to the needle–shaped particles. Also, the center body part is thicker, and the thickness tends to get thinner towards both ends. The tip shape is not clearly sharp compared to needle–shaped particles.



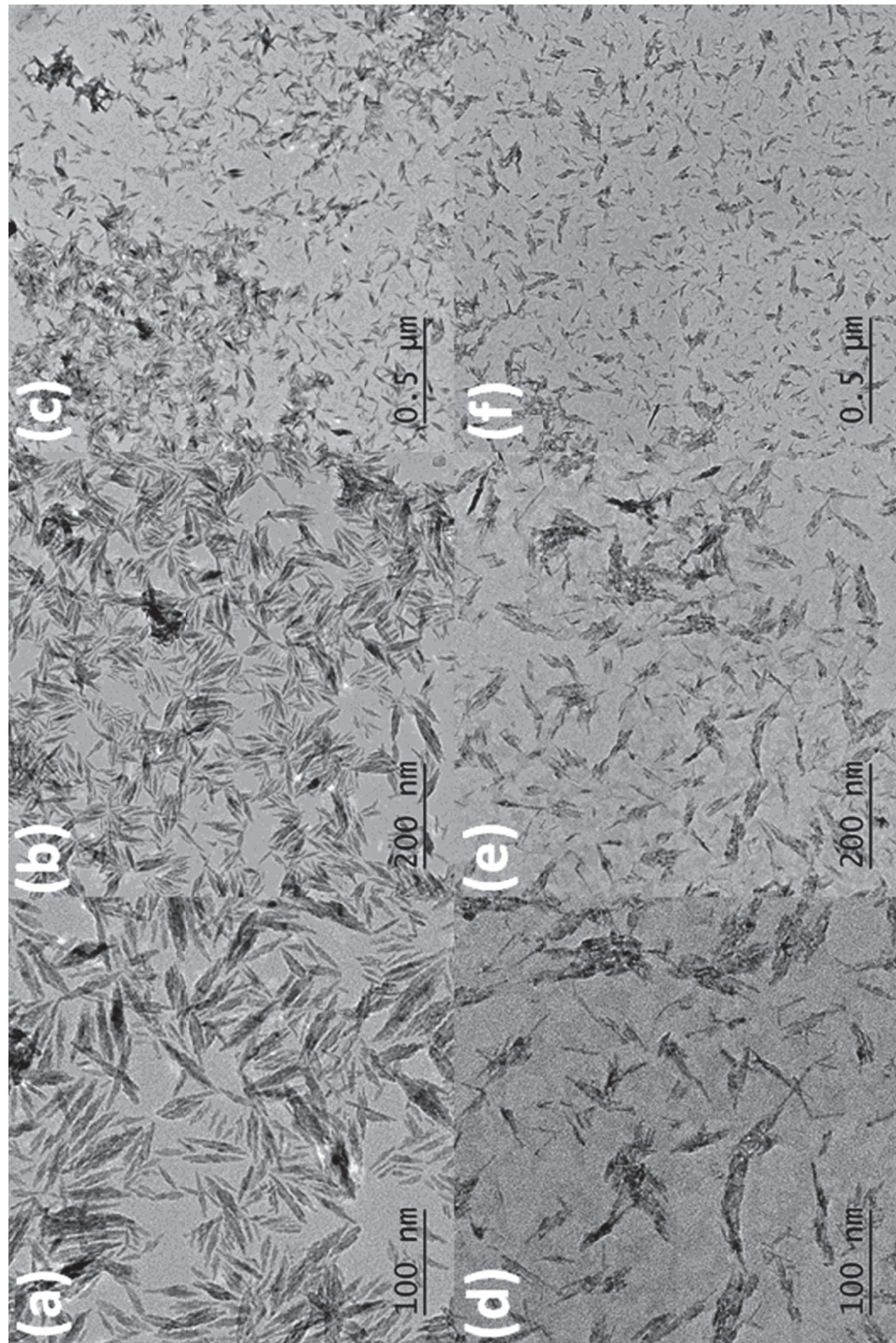


Figure 2-3. TEM images of (a, b, c) PLP and (d, e, f) PHP

## **Chapter 2. An Experimental study on submerged electrical discharge in deionized water**

The difference in particle size distribution is also observed between PLP and PHP. The particle size distribution of PLP and PHP measured from a hundred particles that were randomly chosen are shown in Figure 2–4 (a) and (b). The distance between tip–to–tip of the particle was measured in pixels using a photoshop program and recalculated based on the scale in the image. According to the Figure 2–4, the particle size distribution of PLP is more uniform than that of PHP.



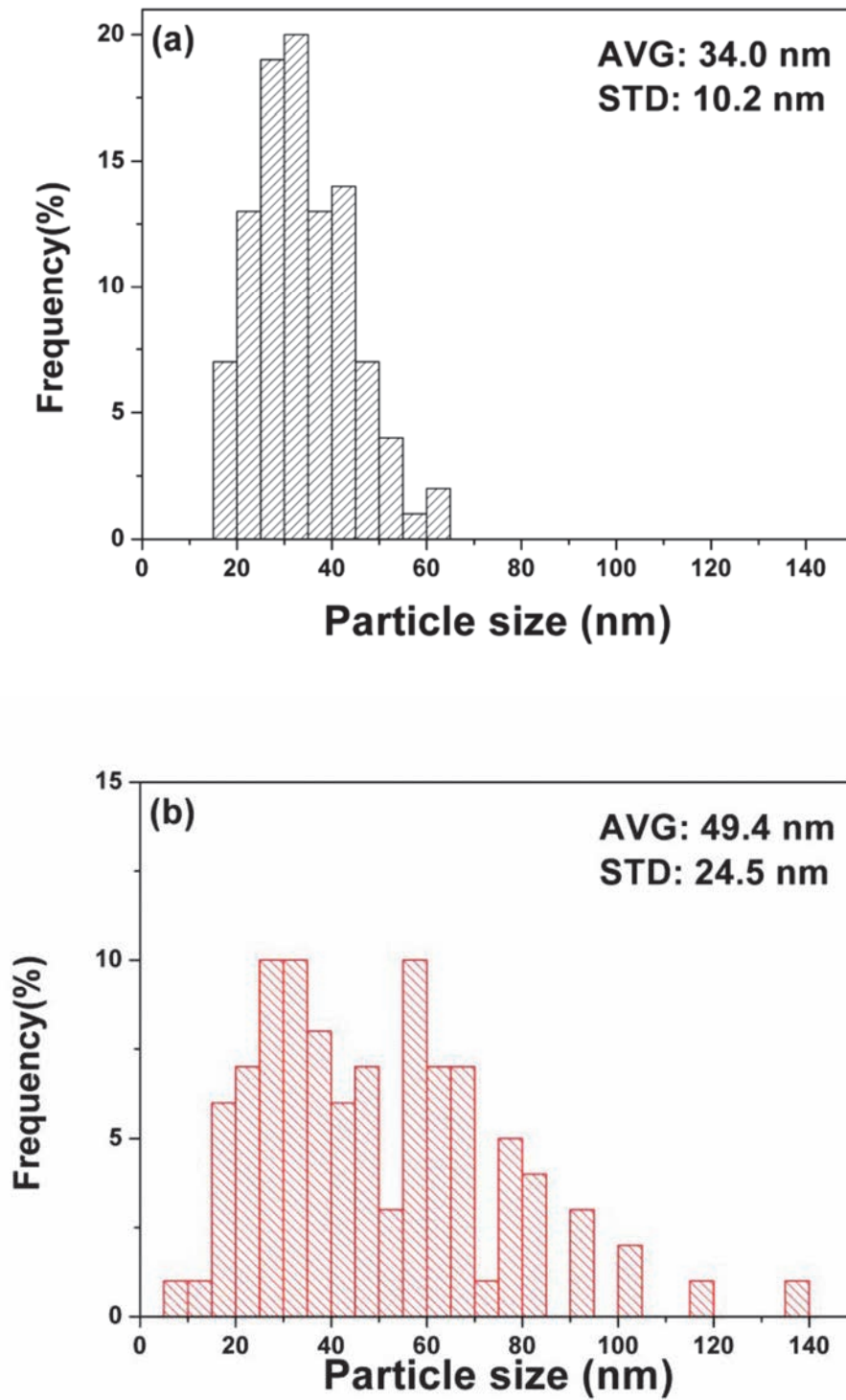


Figure 2-4. Particle size distribution obtained from TEM images; (a) PLP, (b) PHP

## 2.3.2 Chemical composition of a prepared particle in deionized water

### discharge

#### 2.3.2.1 SAED pattern

The phase composition of each product was identified by diffraction patterns obtained from TEM, as shown in Figure 2–5. It is seen that cupric oxide (CuO) was the main component in both PLP and PHP.

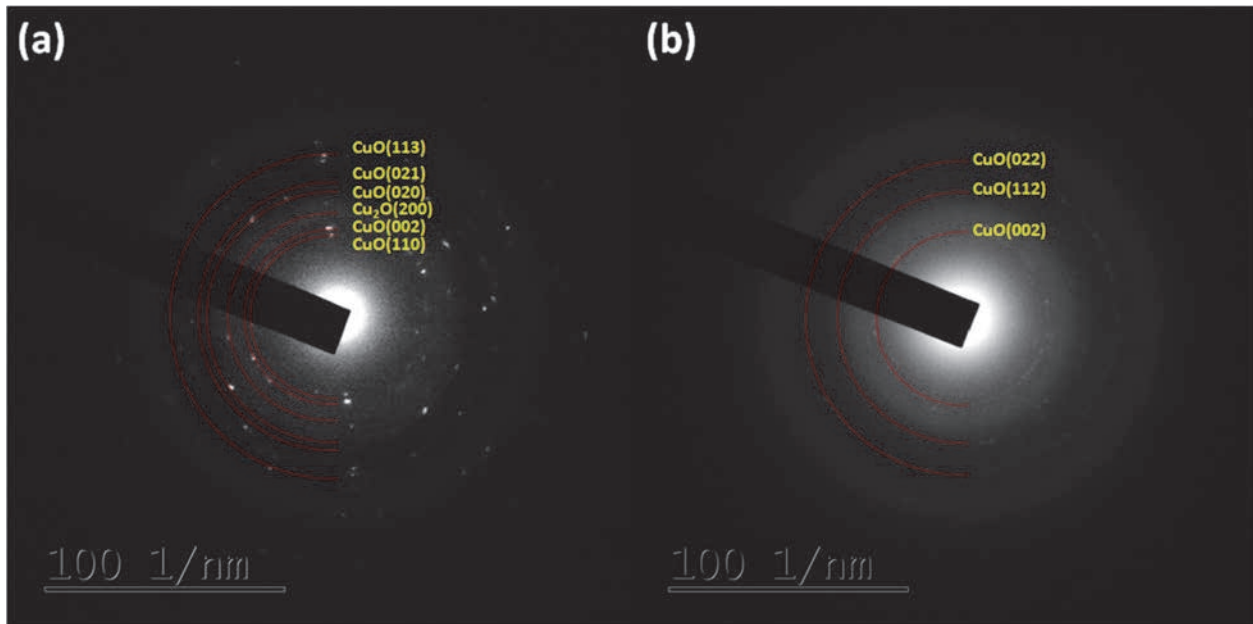


**Figure 2–5.** Diffraction patterns of (a) PLP and (b) PHP both corresponding to copper oxide

### 2.3.2.2 XPS analysis

The difference in the chemical bonding state of the electrodes was analyzed by XPS. Figure 2–6 shows Cu2p spectra and the fitted curves of the electrode after the discharge at the low–power mode (Figure 2–6 (a)) and at the high–power mode (Figure 2–6 (b)). Figure 2–20 (a) shows the three curves in Cu2p<sub>3/2</sub> corresponding to metallic Cu at 932.4 eV, CuO at 933.8 eV, and Cu<sup>2+</sup> satellite at 942.6 eV, while Figure 2–6 (b) shows those curves corresponding to metallic Cu at 932.7 eV, Cu(OH)<sub>2</sub> at 934.7 eV, and Cu<sup>2+</sup> satellite at 942.9 eV. Both electrodes seemed to have the three fitted curves; metallic Cu curves and Cu<sup>2+</sup> satellite in common and CuO at the low–power mode, and Cu(OH)<sub>2</sub> at the high–power mode. When compared to the phase composition of the products shown in Figure 2–5, it could be seen that PLP after discharging at the low power mode have the CuO crystalline structure in common as they have similar morphologies as mentioned in the previous discussion. This result of XPS analysis also provides reasonable evidence that PLP was directly derived from the detachment of the nanostructure on the electrode.

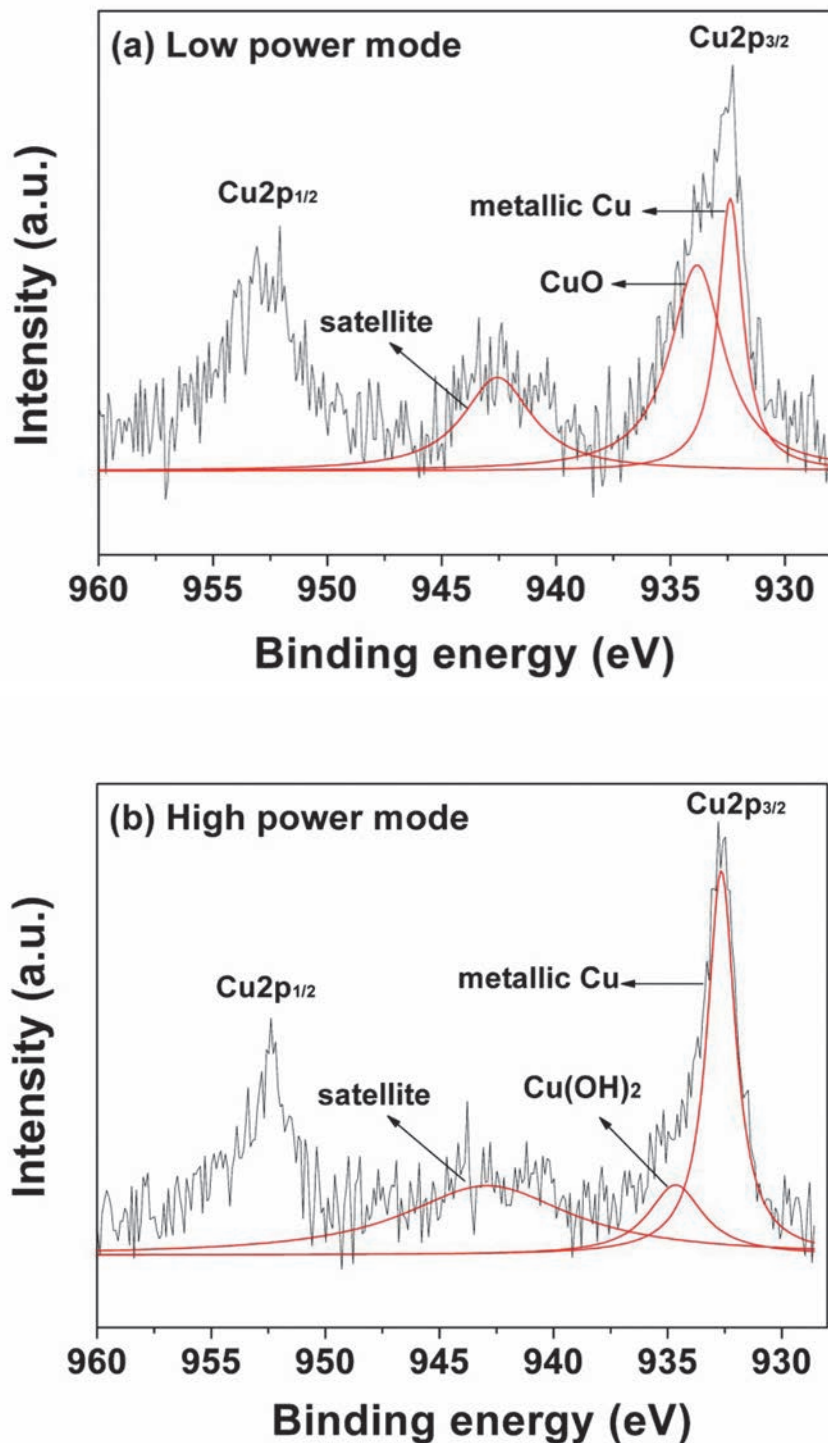
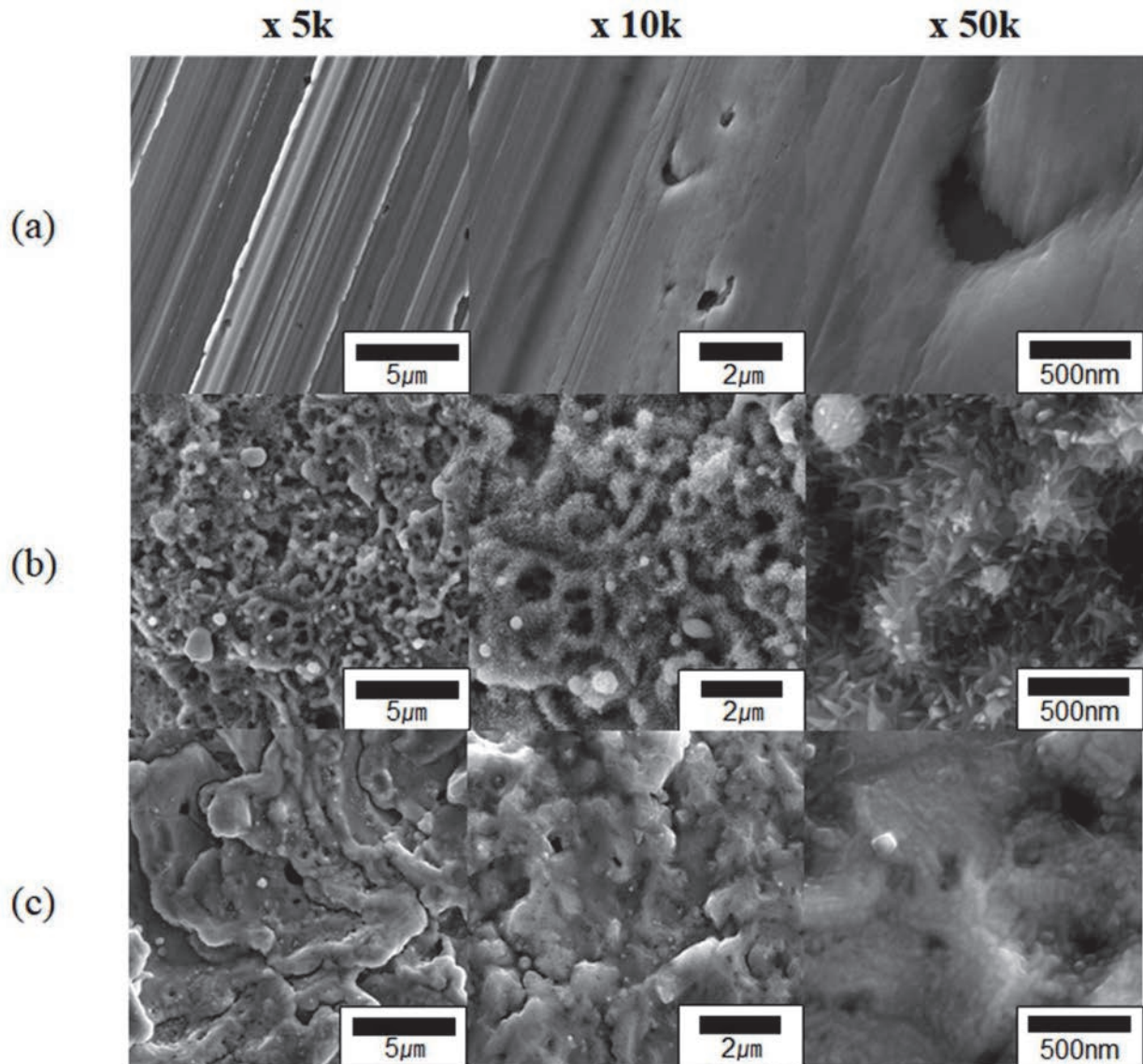


Figure 2–6. Cu<sub>2</sub>p spectra of the electrode after discharging at (a) the low power mode and (b) the high power mode analyzed by XPS

### 2.3.3 Formation mechanism of CuO nanoparticles in deionized water discharge

The surface morphologies of copper electrodes in deionized water discharge were also observed, as shown in Figure 2–7. The pristine electrode has a smooth surface, although some scratches are observed from the low magnification image because of polishing as a pre–treatment for removing the contaminant. After discharging at the low–power mode (Figure 2–7 (b)) and at the high–power mode (Figure 2–7 (c)), the surface morphologies are clearly different. In the low magnification image of Figure 2–7 (b), the electrode after the discharge at the low–power mode seems to have a porous structure. While in the high magnification image of Figure 2–7 (b), the formation of a needle–like structure is confirmed. It is interesting because this structure seems to correspond to the morphologies of PLP. Thus, it is reasonable that PLP was directly derived from the detachment of those needles on the electrode during discharge. On the other hand, the surface morphologies of the electrode after discharging at the high–power mode in Figure 2–7 (c) shows only traces of the molten electrode, indicating that it does not correspond to the morphologies of PHP.



**Figure 2–7.** Surface morphologies of the electrode (a) before discharging and after discharging at (b) the low–power mode and (c) the high–power mode

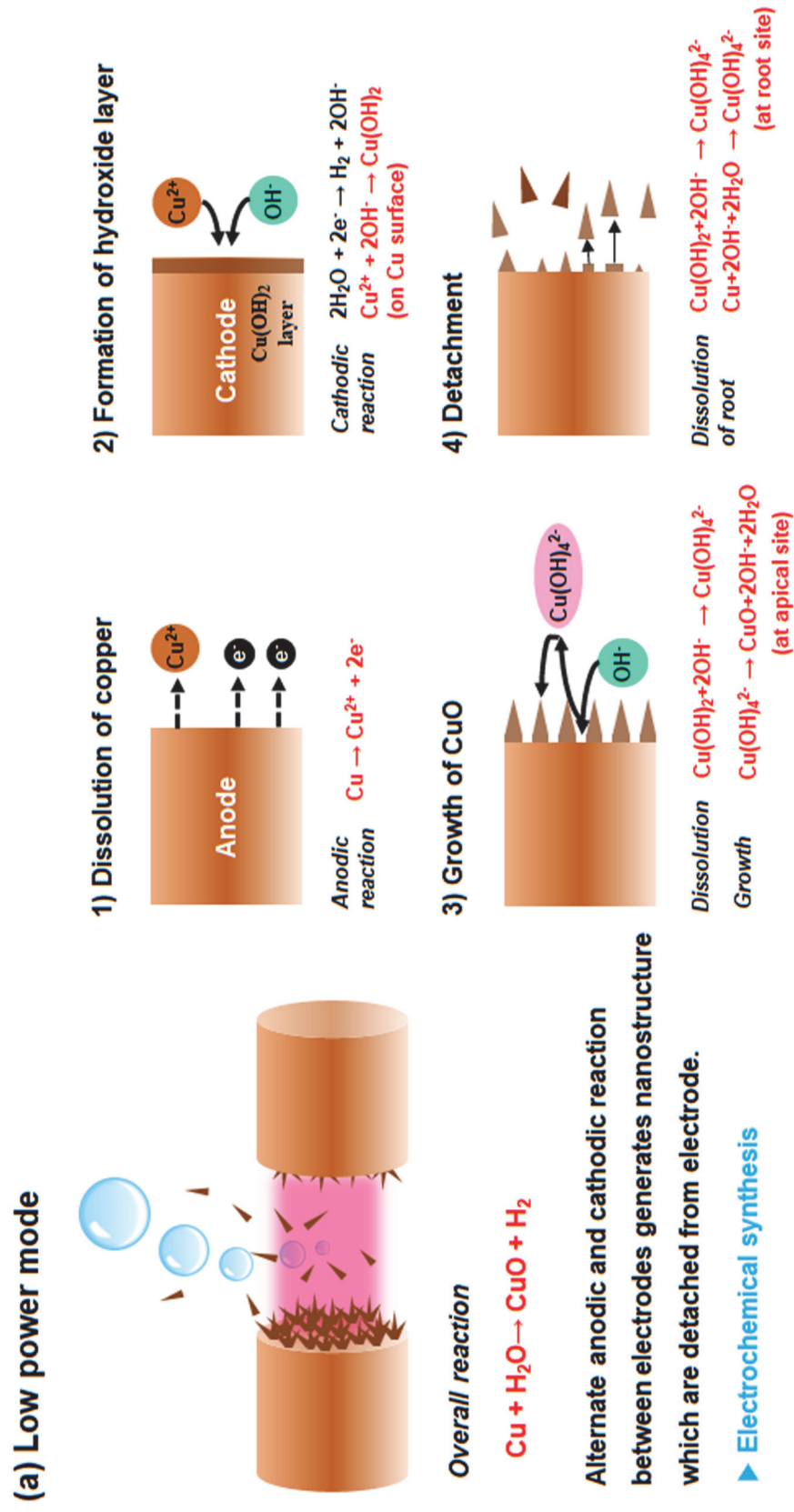
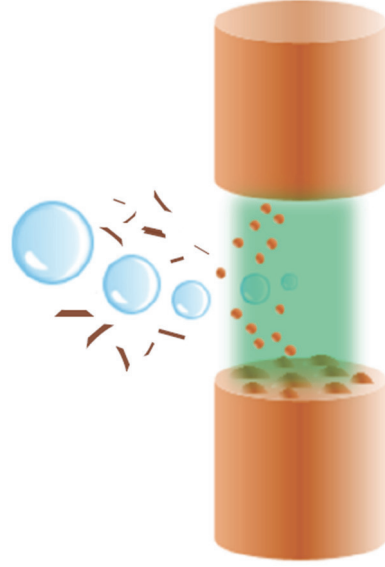


Figure 2–8. The supposed mechanism for the generation of CuO nanoparticles at (a) the low–power mode



**(b) High power mode**



**Overall reaction**



Copper nanoclusters generated from partial heating of the electrodes grow to CuO rod.

- ▶ Combination of physical (nanocluster generation) and chemical (crystal growth) process

**1) Heating of electrode**



**Partial Melting**  
 $\text{Cu (s)} \rightarrow \text{Cu (l)}$

**2) Generation of Cu nanoclusters**



**Vaporization**  
 $\text{Cu(l)} \rightarrow \text{Cu(g)}$   
**Nucleation**  
 $\text{Cu(g)} \rightarrow \text{Cu cluster}$

**3) Oxidation of nanoclusters**



**Dissolution of oxygen**  
 $\text{O}_2(\text{g}) \rightarrow \text{O}_2(\text{aq})$   
**Growth**  
 $\text{Cu cluster} + \text{O}_2(\text{aq}) \rightarrow \text{CuO cluster}$

**4) Crystal growth**



**Ostwald ripening**  
 $\text{CuO cluster} \rightarrow \text{CuO (cr)}$

Figure 2–9. The supposed mechanism for the generation of CuO nanoparticles at (b) the high–power mode



In this study, we suppose the formation mechanism of CuO nanoparticles is based on the above observation. Here, we focused on two points to investigate the particle formation mechanism; (i) alternate cathodic and anodic reaction and (ii) electrochemistry between water and copper electrode.

At first, the power variation of arc discharge was considered to affect particle formation. Figure 2–8 (a) illustrates the supposed electrochemical mechanism for the generation of needle–like CuO nanoparticles. When the low power mode was applied, the arc plasma was not hot enough to melt the copper electrode. However, the arc plasma could induce an electrochemical reaction by dissociating water to produce reactive species such as hydroxyl radical. One feature of this reaction was that the electrochemistry was dominated by bipolar pulse power, which generated alternate anodic and cathodic reactions between the electrodes. At the initial stage of discharge, the copper electrode emits copper ions and electrons when it works as an anode. When the polarity of pulse changes, the same electrode undergoes a cathodic reaction in which reduction of water ( $2\text{H}_2\text{O} + 2\text{e}^- \rightarrow \text{H}_2 + 2\text{OH}^-$ ) occurs. Here the generated hydroxide ions ( $\text{OH}^-$ ) react with the emitted copper ions around the surface of the electrode so that the copper hydroxide layer is formed. It should be noted here that  $\text{OH}^-$  is continuously provided when the electrode works as a cathode. The excess  $\text{OH}^-$  dissolves  $\text{Cu}(\text{OH})_2$  from the electrode to form complex anion  $\text{Cu}(\text{OH})_4^{2-}$ . It has been reported that  $\text{Cu}(\text{OH})_4^{2-}$  is considered as a precursor for CuO [71–73]. Transformation of  $\text{Cu}(\text{OH})_4^{2-}$  to CuO is performed with a loss of two  $\text{OH}^-$  and one water molecule ( $\text{Cu}(\text{OH})_4^{2-} \rightarrow \text{CuO} + 2\text{OH}^- + \text{H}_2\text{O}$ ).  $\text{Cu}(\text{OH})_4^{2-}$  condenses at the apical site to form needle–like CuO crystal. Finally, these needle–like CuO grown on the electrode surface are detached because of both dissolution of Cu and CuO at their root site.

On the other hand, particle generation is considered to be dominated by vapor phase synthesis at the high–power mode. Figure 2–9 (b) illustrates the supposed mechanism for the generation of clipped nail–like CuO nanoparticles at the high–power mode. In this mode, the temperature of arc plasma is considered high enough to melt and evaporate the arc spot at the electrode. Once the vapor of copper is generated, it is rapidly condensed by surrounding water to form copper nanoclusters. The generated nanoclusters are easily oxidized due to the dissolved oxygen in the water. The generated CuO nanoclusters grow in a monoclinic crystal, which is a

natural structure property of CuO. Although the electrochemistry which dominated the reaction also occurs and partially generates the copper hydroxide layer, the thermal effect such as melting will hinder the electrochemistry on the electrode. In other researches, similar CuO nanoneedles are produced by chemical etching and anodization method on the copper foils [74–77]. Wenwen et al. reported that when the etching time increases, the morphology changed from sharp needles to dense sharp needles, and then sharp needles loss their sharpness and transformed into a stamen-like structure, finally forms into a curved flower-like cluster [74]. In our study, high power conditions may promote the chemical reaction and transform the sharp needle into a thick and bend as clipped nail-like structure. Furthermore, the generated monoclinic structure of CuO and clipped-nail-like particles are aggregated by colliding with each other. However, the irregular collision between the clusters leads to the broadness of particle size distribution, as shown in the experimental results.

### 2.4 Summary

The electrical discharge was successfully maintained under deionized water using the bipolar pulse power supply. Nano-size of copper oxide particles were synthesized using a copper electrode as a raw material without any electrolyte by submerged electrical discharge process. In a deionized water discharge experiment using bipolar pulse power, the particles were synthesized at two operating conditions called as low-power mode (4kV, 20kHz) and high-power mode (9kV, 60kHz). The brownish aqueous solutions, including CuO nanoparticles, were obtained after discharge. However, the morphologies were different according to the operating condition. When the low-power mode was applied, the needle-like CuO with narrow size distribution was observed, while the clipped nail-like CuO with broad size distribution was observed with a high-power mode. The analysis of the electrode implied that the characteristics of the obtained particles corresponded to the nanostructure generated on the surface of the electrode after discharge at the low-power mode but not at the high-power mode. Finally, the particle generation mechanism was proposed based on the experimental results. When the low-power mode was applied, the

electrochemical reaction between water and copper surface dominated the particle generation. The needle-like CuO nanostructure grew up on the surface of the electrode during discharge, and then the detachment of these structures generated the CuO nanoparticles. Meanwhile, the particle generation at the high-power mode was dominated by the local melting and evaporation of the copper electrode. The CuO nanocluster was generated from the copper electrode and then formed the CuO nanoparticle in the solution.

# **CHAPTER 3**

## **Effect of power supplies on particle preparation using liquid nitrogen discharge**

## 3.1 Introduction

In the previous chapter, particle preparation in DI water discharge was investigated for comparison with the liquid nitrogen discharge. In the DI water as a medium, the unique features of copper oxide fine particles are produced accompanied with reaction with the DI water. Based on the experience on the DI water discharge, we investigated the process using liquid nitrogen. The following two major things are modified in this chapter.

First, liquid nitrogen was employed as a dielectric medium in order to prevent side reactions. To better understand particle preparation phenomena in liquid discharge, liquid nitrogen was chosen because it is widely used as a chemical fields' inert source. The plasma effect on particle preparation without reaction was investigated in liquid nitrogen.

The second, high voltage alternating current (AC), bipolar pulse, direct current (DC) power sources are applied to generate electrical discharge in liquid nitrogen. Liquid nitrogen, which has a triple bond and inert characteristic, requires high breakdown voltage than DI water. For this reason, a high voltage power supply is necessary.

In this chapter, three kinds of power sources are applied to generate electrical discharge in liquid nitrogen, and their effect on the particle production process was investigated. As a raw material, the copper electrode was used similarly to in the previous chapter.

## 3.2 Experimental

### 3.2.1 Preparation of Cu particles using AC transformer in liquid nitrogen discharge

A schematic diagram of the experimental apparatus is illustrated in Figure 3–1. In this experiment, the Cu electrode material, electrode holder, and the dewar-like flask are the same as in the previous chapter. Only the power supply and connection line were changed. A high voltage

**Chapter 3. Effect of power supplies on particle preparation using liquid nitrogen discharge**

AC neon transformer (LECIP, Japan) was applied to generate electrical discharge in the liquid nitrogen. A maximum voltage of 19.5 kV was applied for the experiment. The detailed operating conditions are summarized in Table 3–1.

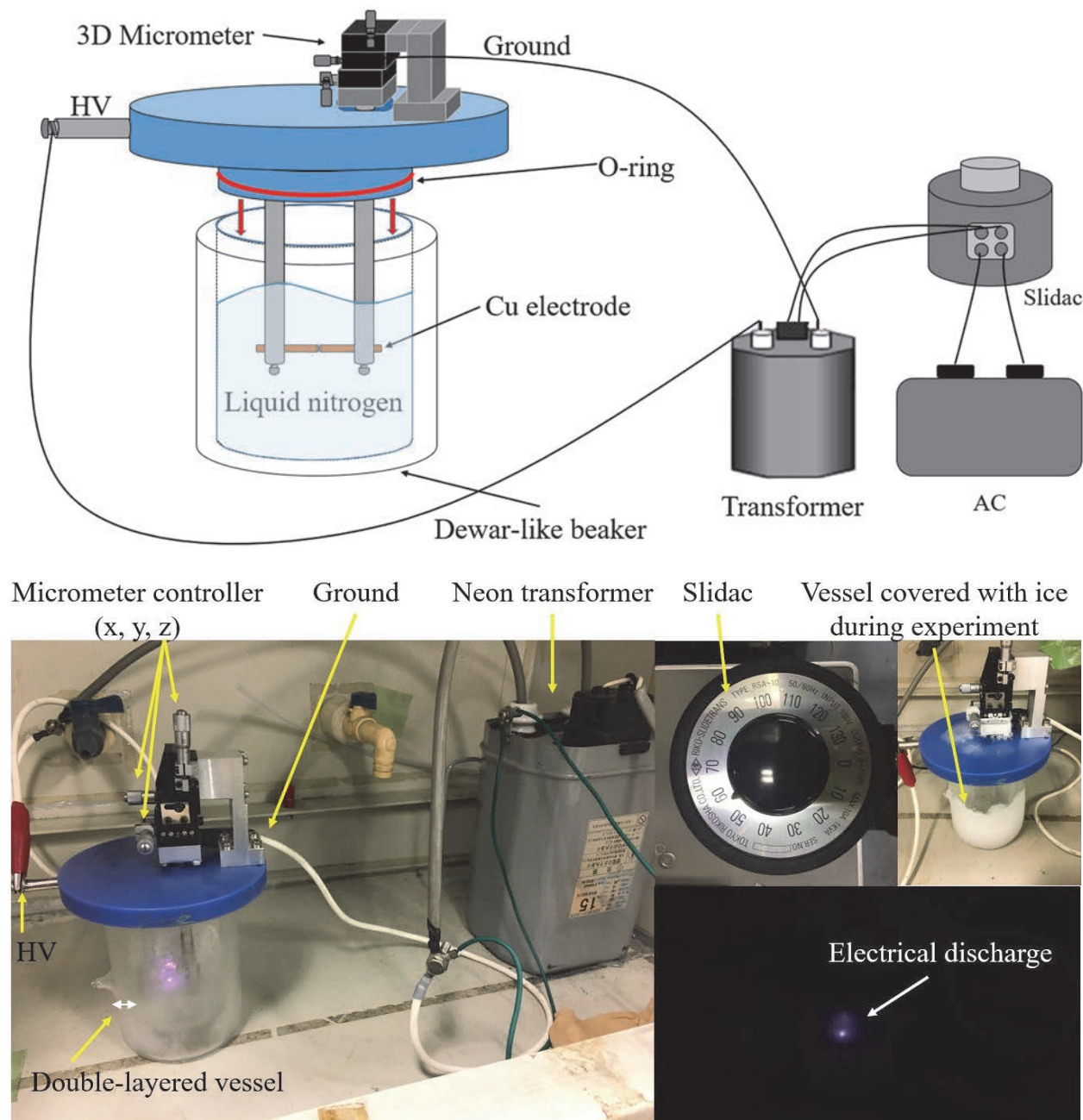


**Figure 3–1.** Schematic diagram of the experimental using an AC step-up transform (upper) and actual picture of the apparatus (bottom)

### **3.2.2 Preparation of Cu particles using bipolar pulse power supply in liquid nitrogen discharge**

Figure 3–2 displays a schematic of the experimental setup and a picture for Cu particle preparation in liquid nitrogen discharge. The same equipment was used in the previous chapter except for dielectric media (DI water replace with liquid nitrogen). A bipolar pulse power supply (Genius2, EN Technologies, Korea) was applied to generate electrical discharge in liquid nitrogen.

For the liquid nitrogen experimental conditions, more than 9 kV was applied for maintaining the discharge for the bipolar pulse power supply. Due to the high breakdown voltage of the liquid nitrogen, the discharge generates from the 9 kV. In order to sustain the electrical discharge, the gap distance and applied voltage were fixed as 300  $\mu\text{m}$  and 9 kV, respectively. The variation of frequency was tested at 20, 40, and 60 kHz. Another operating parameter, such as pulse on–time, was maintained at 2.5  $\mu\text{s}$  as the same in the previous chapter.

The detailed operating conditions are summarized in Table 3–1. Figure 3–3 shows changes in current and voltage recorded with current and voltage recorded with an oscilloscope (AC 50 Hz, TBS 1072B, Tektronix, USA) and an oscilloscope (bipolar pulse power at 20 kHz, 3000X, Agilent Technologies, USA).

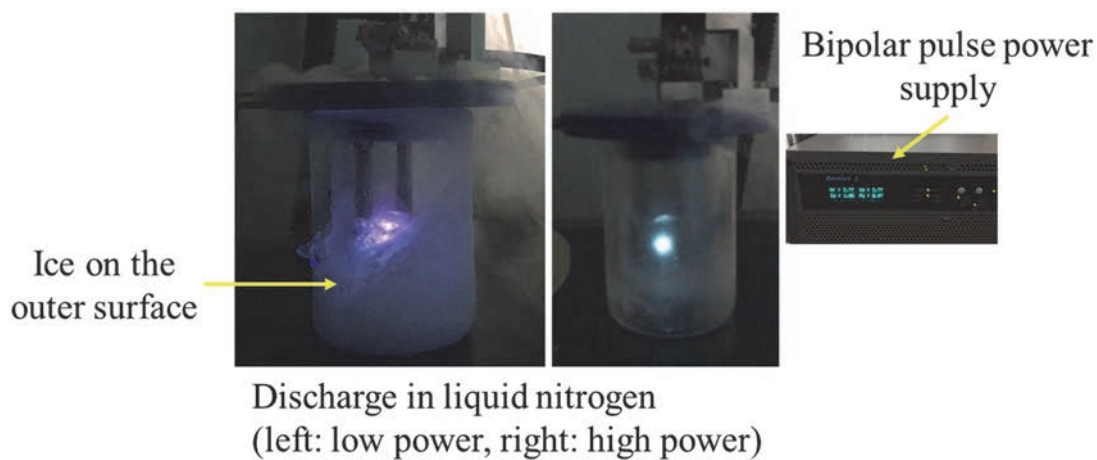
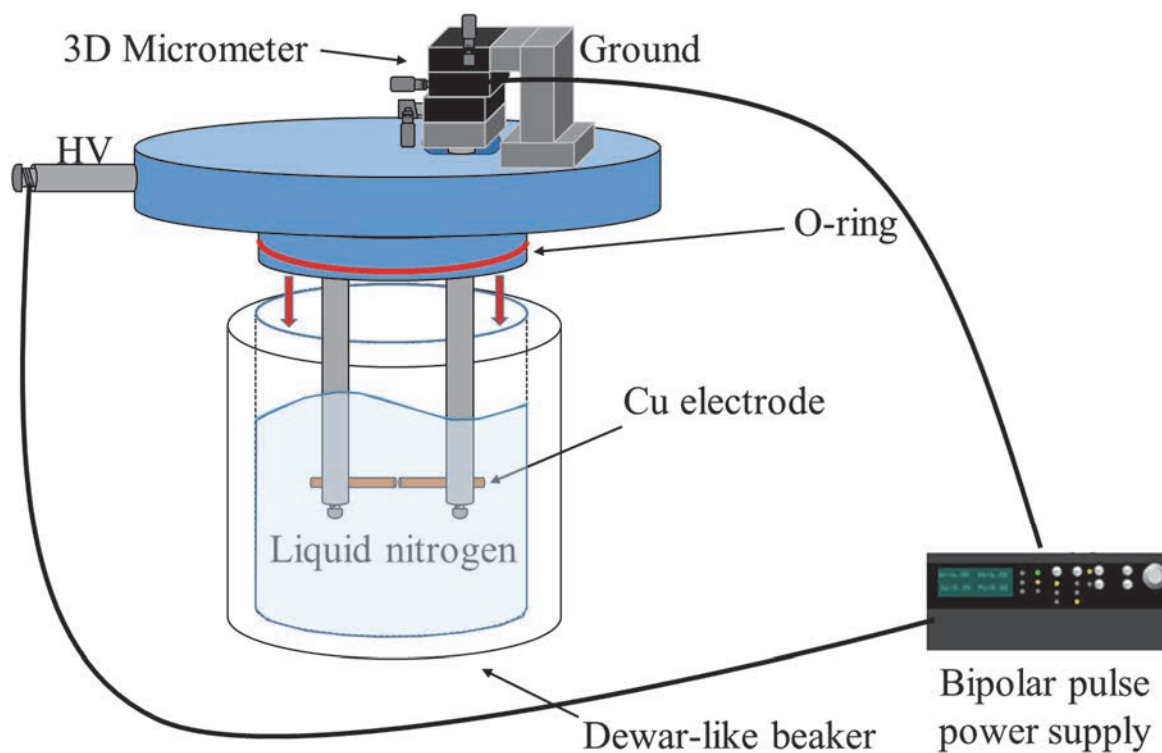


**Figure 3–2.** Schematic diagram of the reactor using a bipolar pulse power supply (upper) and actual picture of the experimental setup (bottom)



**Table 3–1.** Detailed operating conditions for preparation of Cu particles

Power supply	AC		Bipolar pulse			DC	
Dielectric medium	Liquid nitrogen						
Electrode material	Cu rod (>99.99, 3 $\phi$ ) M.P: 1085, B.P: 2562						
Applied voltage	19.5 kV (step-up using slidac 130%)		9 kV			n/a	n/a
Applied current	n/a		n/a			5A	30A
Frequency	50 Hz	20 kHz	40 kHz	60 kHz	n/a	n/a	
Pulse on time	n/a		2.5 $\mu$ s			n/a	n/a
Gap distance	300 $\mu$ m		300 $\mu$ m			Attached (initial) ↔ detached (maintain)	
Gas flow rate	n/a		n/a			N <sub>2</sub> 500 ml/min	
Power Specification	V <sub>max</sub> 15 kV		V <sub>max</sub> =10 kV, V <sub>PP</sub> =20 kV Power up to 2 kW 20~60 kHz			Enable up to 150 A	

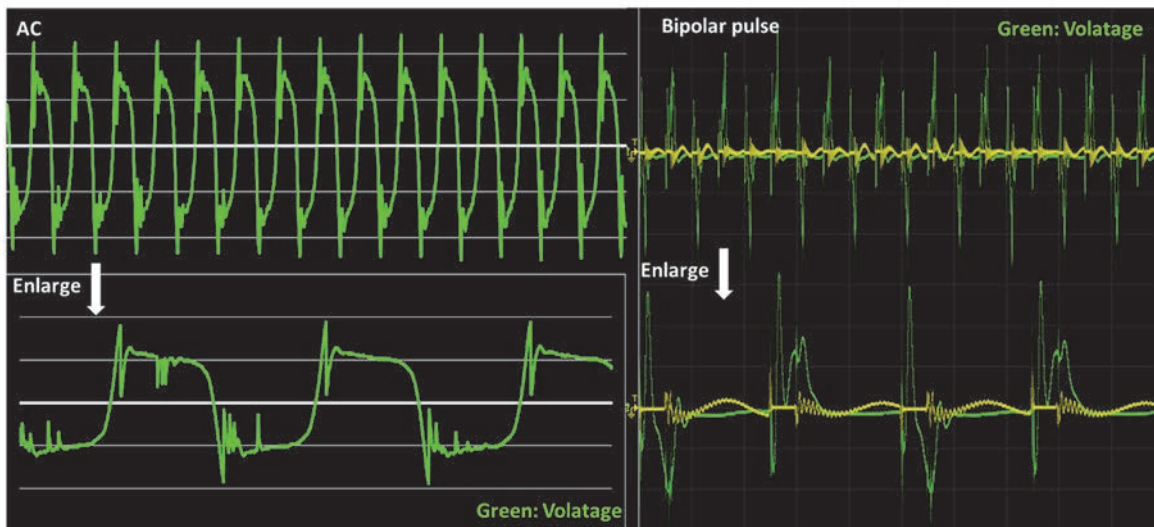


**Figure 3–3.** Voltage and current waveform of plasma generated by AC 50 Hz (left) and bipolar pulse with 20 kHz (right)

### 3.2.3 Preparation of Cu particles using DC power supply in liquid nitrogen discharge

A schematic diagram of the DC arc discharge system is indicated in Figure 3–4. Some pictures of the experimental setup are shown in Figure 3–5. In this study, DC power supply (YE–200BL3, Panasonic, Japan), electrode holder cell, frame, and all the connection parts were newly prepared as compared to the experimental setups for the AC and bipolar power supplies. Electrodes were arranged vertically in order to render them more feasible during the reaction. The arc discharge was generated between copper rods (Nilaco Co., Japan) with a diameter of 3 mm submerged in liquid nitrogen. The specification and physical properties of the copper electrode material are summarized in the previous chapter Table 2–2. As to the DC power setup, in order to provide constant current, the values of initializing current and working current were set identical from a minimum operating current of 5 A to a maximum of 30 A. When the current condition exceeded 30 A, the electrode was difficult to maintain the discharge for a long time because the electrode melted down too quickly. During the experiment, the electrode gap distance was controlled using a millimeter controller manually. At first, the electrodes were placed together with no gap in the DC arc discharge system. Then current was applied with detaching motion simultaneously. The initial breakdown discharge was generated when the electrodes were in detaching motion. The arc was stopped by the electrode melting. Procedures of attaching and detaching the electrodes were repeated to regenerate the discharge. Before the experiment, nitrogen gas at a 500 ml/min flow rate was supplied using a Teflon tube connected to the electrode holder cell to purge inside the vessel and create a nitrogen atmosphere. A continuous supply of nitrogen gas was kept inside the cell during the reaction. The detailed operating conditions are also summarized in Table 3–1.

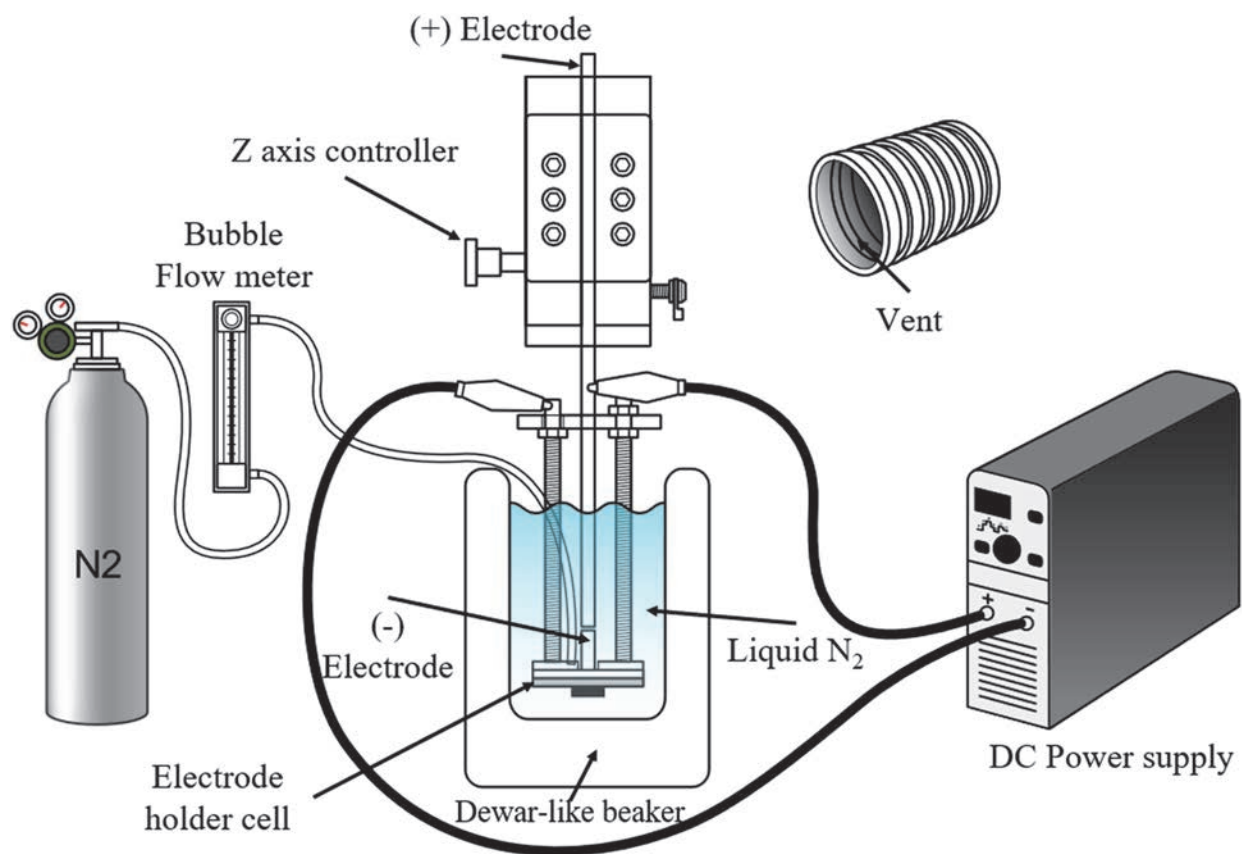


Figure 3-4. Illustration of in-liquid arc plasma reactor using DC power supply

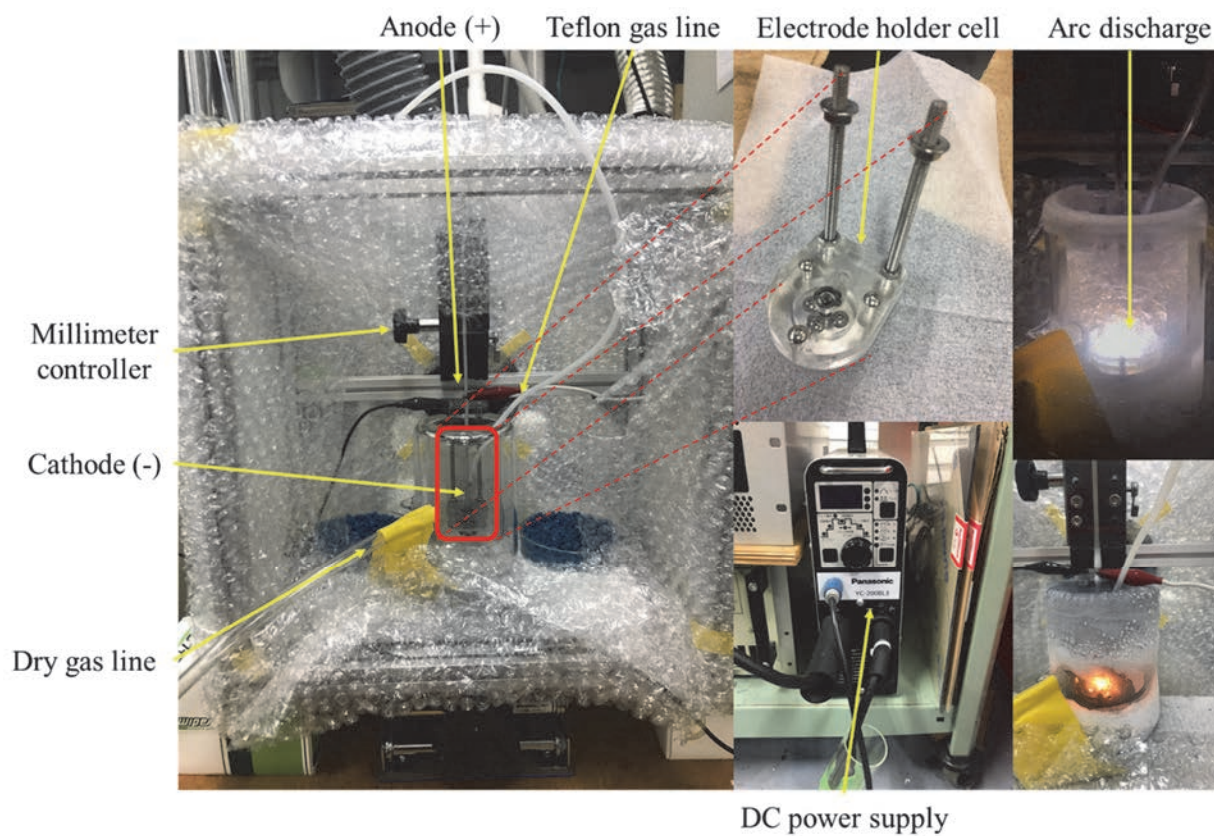


Figure 3–5. A picture of the experimental setup for particle preparation using DC in liquid nitrogen

### 3.2.4 Experiment procedure in liquid nitrogen discharge

Each of the electrodes was cut by a diamond blade cutter in order to minimize impurities. After cutting electrodes, the surface of the electrode was ground by sandpaper, followed by ethanol washing and air blow drying. Electrodes were set on the electrode holder, and gap distance was closely manipulated. Liquid nitrogen was kept supplied to maintain a liquid nitrogen atmosphere. During the liquid nitrogen discharge experiments, in order to secure a clear vision inside the vessel, dry nitrogen gas was supplied to prevent ice formation on the vessels' outer surface. Electrode status and liquid nitrogen amount were frequently confirmed during the experiment. After the experiment, whole parts were dried using an oven to let liquid nitrogen vaporize.

In the case of liquid nitrogen discharge samples using AC and bipolar pulse power, fine sediment particles from the bottom of the vessel were swept directly using carbon tape in order to observe particle morphology by the FE-SEM. There were no visible particles on naked eye examination. Hence, we directly sampled particles from the vessel bottom.

Lastly, in a liquid nitrogen discharge experiment using the DC power, samples were classified into three types, namely electrode debris, coarse particles, and fine particles. Electrode debris and coarse particles were collected from the reactor wall and bottom using a micro-spatula. Fine particles were collected from the vessel and cell part using ethanol 99.5% (Kanto Chemical Co., Inc., Japan) as a dispersion agent. The ethanol solution was treated with a sonification of about 30 mins. The characterization sampling was proceeded with this ethanol solution and produced particles.

### 3.2.5 Characterization

The crystalline phases of the coarse particle samples were investigated by X-ray diffraction (XRD, Rigaku Mini Flex 600), which was operated with a Cu K $\alpha$  source at 40 kV and 15 mA. Prepared coarse particle samples were measured in the scanned range of 2 theta from 10° to 80°

degrees with a step size of  $0.02^\circ$ . The measurement scan rate was  $5^\circ/\text{min}$ . All samples were measured more than twice to check for any aging effects after exposure to air for several weeks. The obtained XRD peaks were assigned based on the database of the PDXL software.

The surface of the obtained particles and electrodes were observed with a scanning electron microscope (SEM, VE-9800, Keyence, Japan) for low magnification and two kinds of field emission scanning electron microscope (1.FE-SEM, SU9000, Hitachi, Japan, 2.FE-SEM, JSM-7500F, Jeol, Japan) for high magnification.

The morphologies of the synthesized particles were analyzed by a field emission transmission electron microscope (FE-TEM, JEM-2100F, Jeol, Japan) operating with a voltage of 200 kV. The particles were dispersed in ethanol by ultrasound and then sampled on the copper grid for FE-TEM. The ethanol was completely removed by drying the grid for some days.

SAED (Selected area electron diffraction) was used to obtain information on the crystal structure of the prepared particles. From using Bragg's equation, the  $2\theta$  was calculated. The detail is explained in the previous chapter.

## **3.3 Results and discussion**

### **3.3.1 Morphologies of the prepared particles in liquid nitrogen discharge**

Prepared Cu particles were observed by FE-SEM. After the liquid nitrogen discharge using AC and bipolar pulse power, particles were directly collected from the bottom part of the container. In the case of DC power samples, produced fine particles were dispersed in ethanol and then spread on the support (7500F: carbon tape, SU9000: nickel grid) using a pipette for FE-SEM characterization. The drying and spreading process was repeated three times to mount the sample enough. Figure 3-6 is an image of copper particles produced by AC power applied voltage of 19.5 kV. Figure 3-7 shows the copper particles prepared by DC power supply applied with currents of 5 A and 30 A. Low magnification photos were obtained from 7500F (a, b, c, d) and high magnification (e, f, g, h) photos from SU9000. Through the high magnification images, the

spherical copper particles and nano-sized grain-shaped particles were confirmed on the spherical copper particle surface. Figure 3–8 shows the copper particles obtained by liquid nitrogen discharge using a bipolar pulse power source applying 20 and 60 kHz frequencies. According to the FE–SEM images, there was no significant difference between the produced particle shapes using different power sources. In all the conditions, spherical copper particles were observed. These spherical particles were ranged in size from nanometer to micrometer.

In the bipolar power supply, we could not observe sufficient samples to compare the particle size directly. However, we measured the diameter of each random 100 particles from each of the AC and DC, FE–SEM images, respectively. The particle size distribution is indicated in Figure 3–9, and Table 3–2 shows the average particle size and standard deviation of the particles produced under AC and DC conditions. The size distributions of Cu particles were arranged from 15 nm to 15  $\mu$ m. From the data based on Table 3–2, the average size of the particle was increased around 200 %, and the standard deviation value was increased above 300% (from 0.78 to more than 2.48) when the DC power was employed. AC power provided smaller particles with good uniformity in the size distribution compared to the DC power supply in this experiment. However, the high–power DC produced more particles in the same discharge time. DC provided low uniformity on the size distribution as compared to AC.

The reason for the above result is related to the power characteristics of AC. The applied power is weaker than DC, and the input energy is dispersed into both electrodes. We can assume that the temperature of the AC electrode surface is relatively lower than the DC when discharge occurs. Since the temperature of the electrode surface is low, the local hot spot hills will be small. When the hill is small, it is reasonable to infer that relatively small particles will come out. For the same reason, the size distribution of AC is more uniform.

In the case of DC, the energy applied in 5 A is small than 30 A. However, the average particle size of the particles is slightly larger. The reason is that among the produced copper particles, the micro–size of the particles are seemed to be generated by the melting process, and the nano–size particles are determined to be generated by the vaporization process. In 5 A, the melting mechanism is dominant, so most of them are micro–sized particles. On the other hand, in the case of 30 A, even the melting mechanism is still the dominant process. However, vaporization

### **Chapter 3. Effect of power supplies on particle preparation using liquid nitrogen discharge**

occurs in this condition, and some nano-sized particles are generated. In Figure 3-9 (b) 5 A, there are no particles less than 500 nm, whereas in (c) 30 A, particles less than 500 nm a little exists. Since these nanoparticles are considered in the measurement of average size calculation, it was lesser than 5 A in the average calculation.



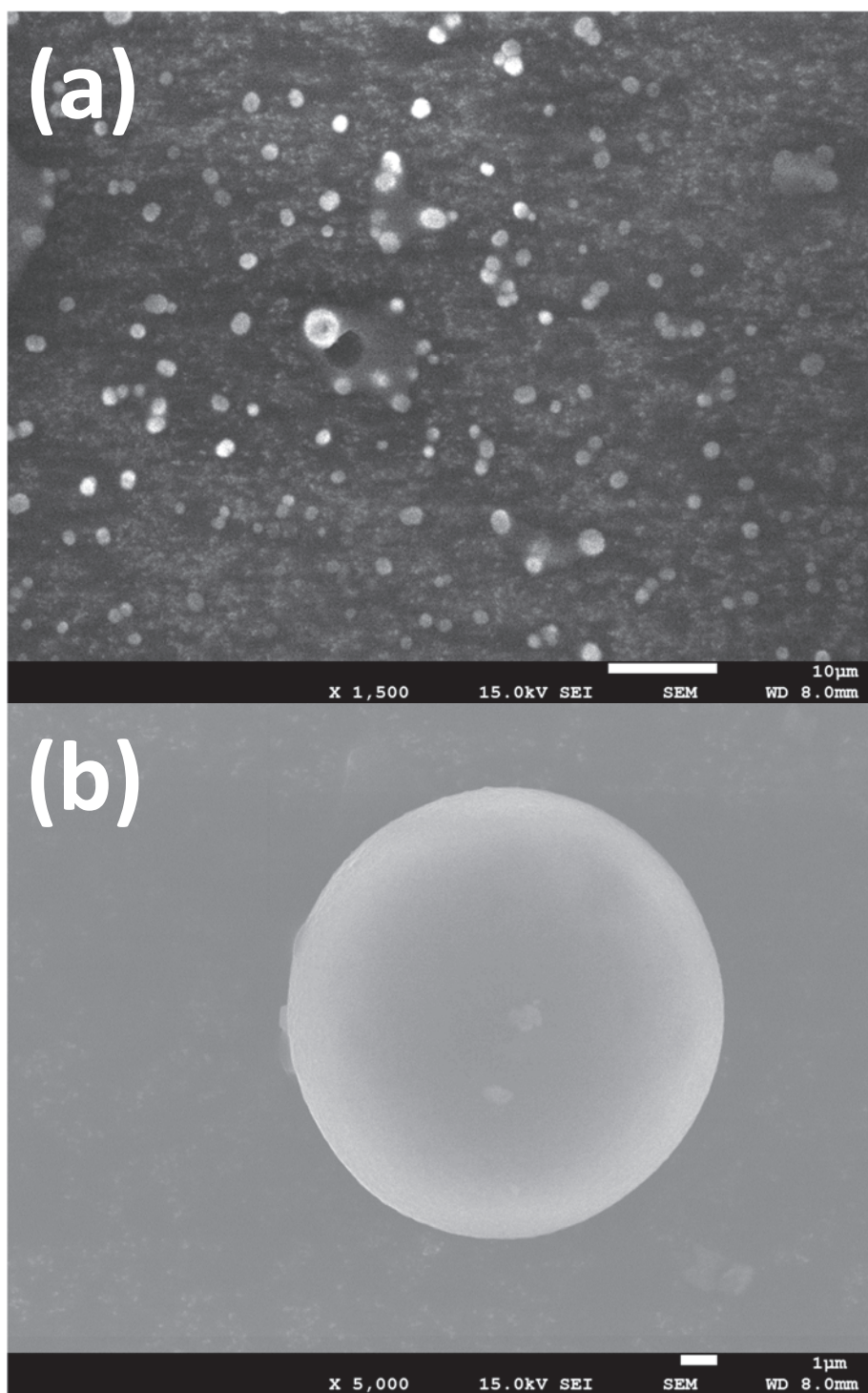


**Figure 3–6.** FE–SEM images of the particles prepared by AC power. SU4300:  
(a) x1,500; (b) x5,000

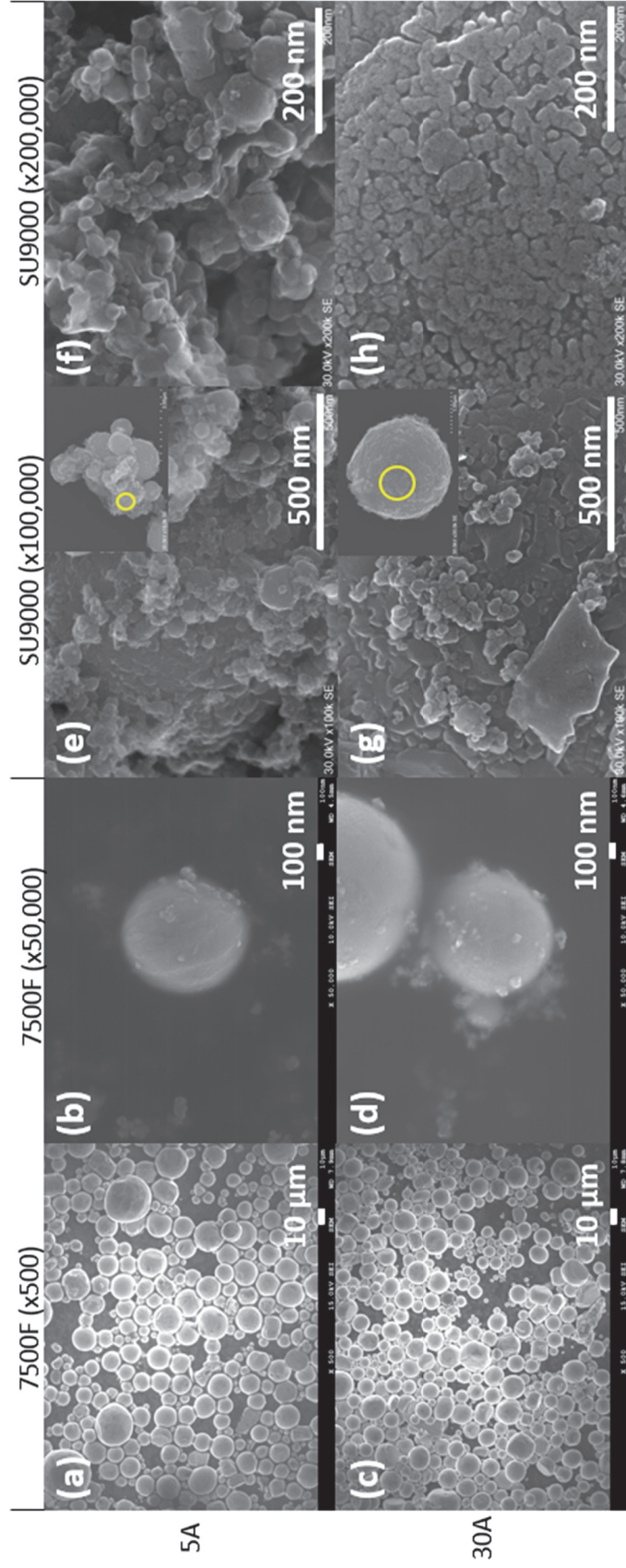


**Figure 3–7.** FE–SEM images of the particles prepared by DC power. 7500F: (a, b) DC 5 A, (c, d) DC 30 A, SU9000: (e, f) DC 5 A, (g, h) DC 30 A. The inserted figure in the yellow circle part is the low magnification image of the (e) and (g), respectively.

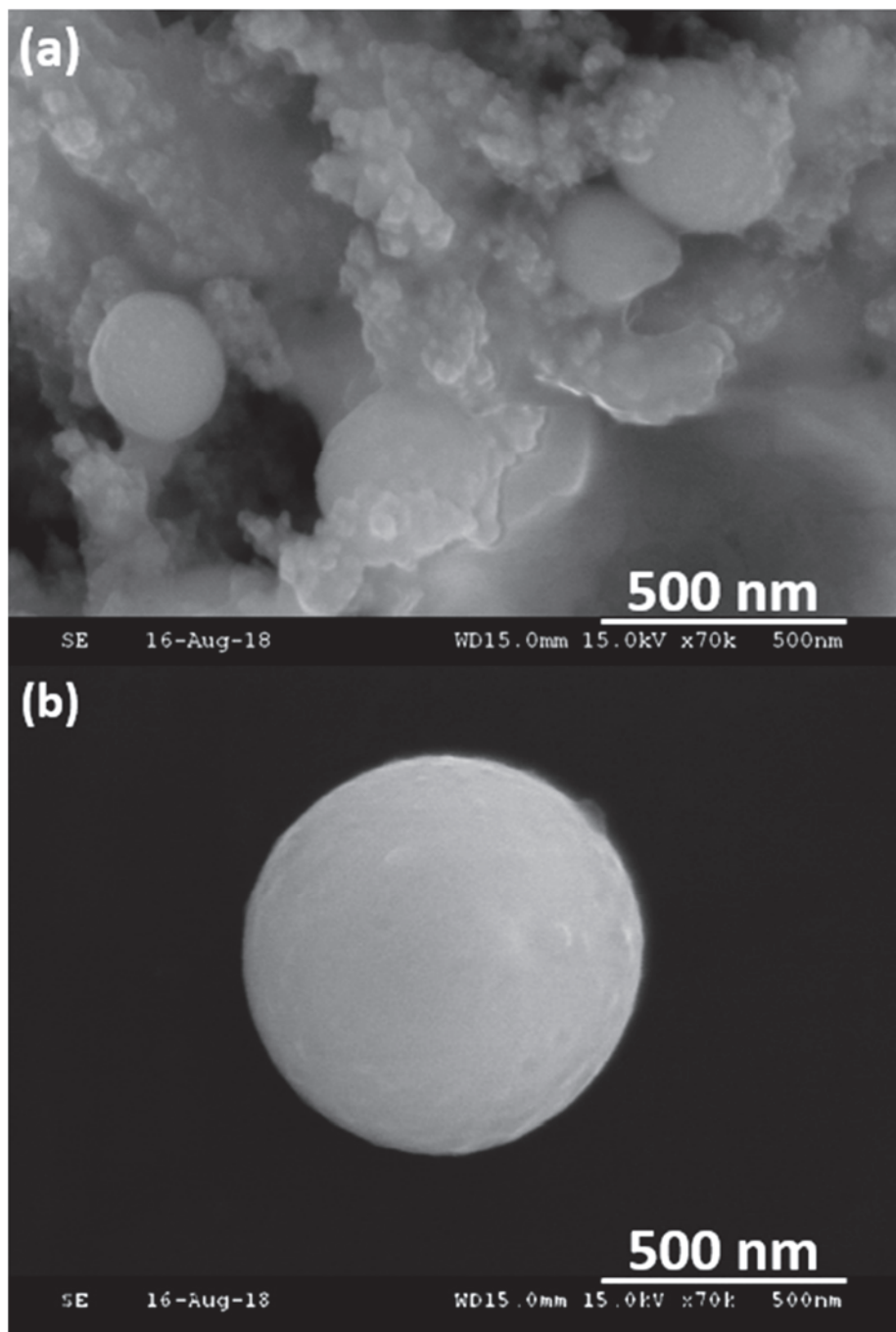


**Figure 3–8.** FE–SEM images of the particles prepared by bipolar pulse power. SU4300: (a) 9 kV, 20 kHz, (b) 9 kV, 60 kHz

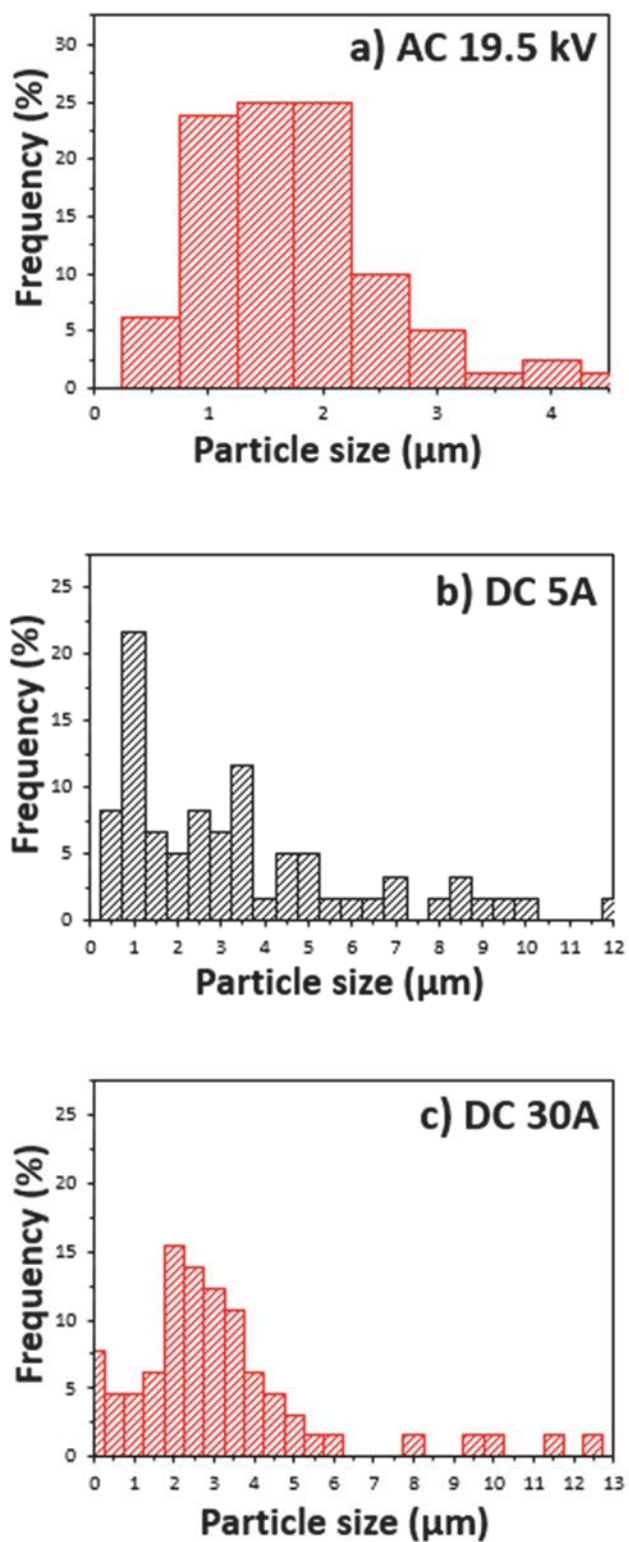


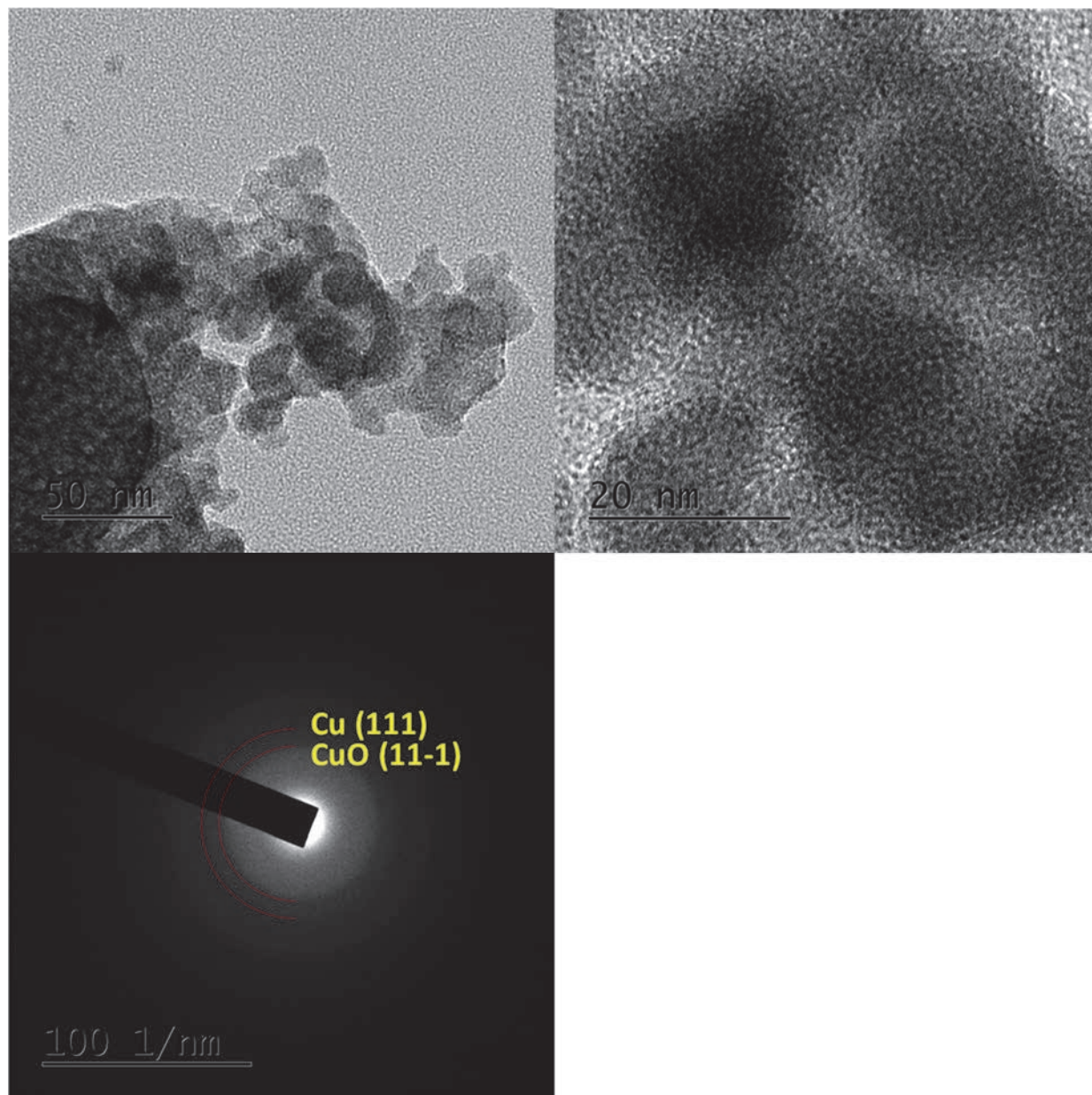
Figure 3–9. Particle size distribution of prepared Cu particle in liquid nitrogen discharge by a) AC, b) DC 5 A and c) DC 30 A.

**Table 3–2.** Average particle size and standard deviation of prepared Cu particles depending on the AC and DC power supply

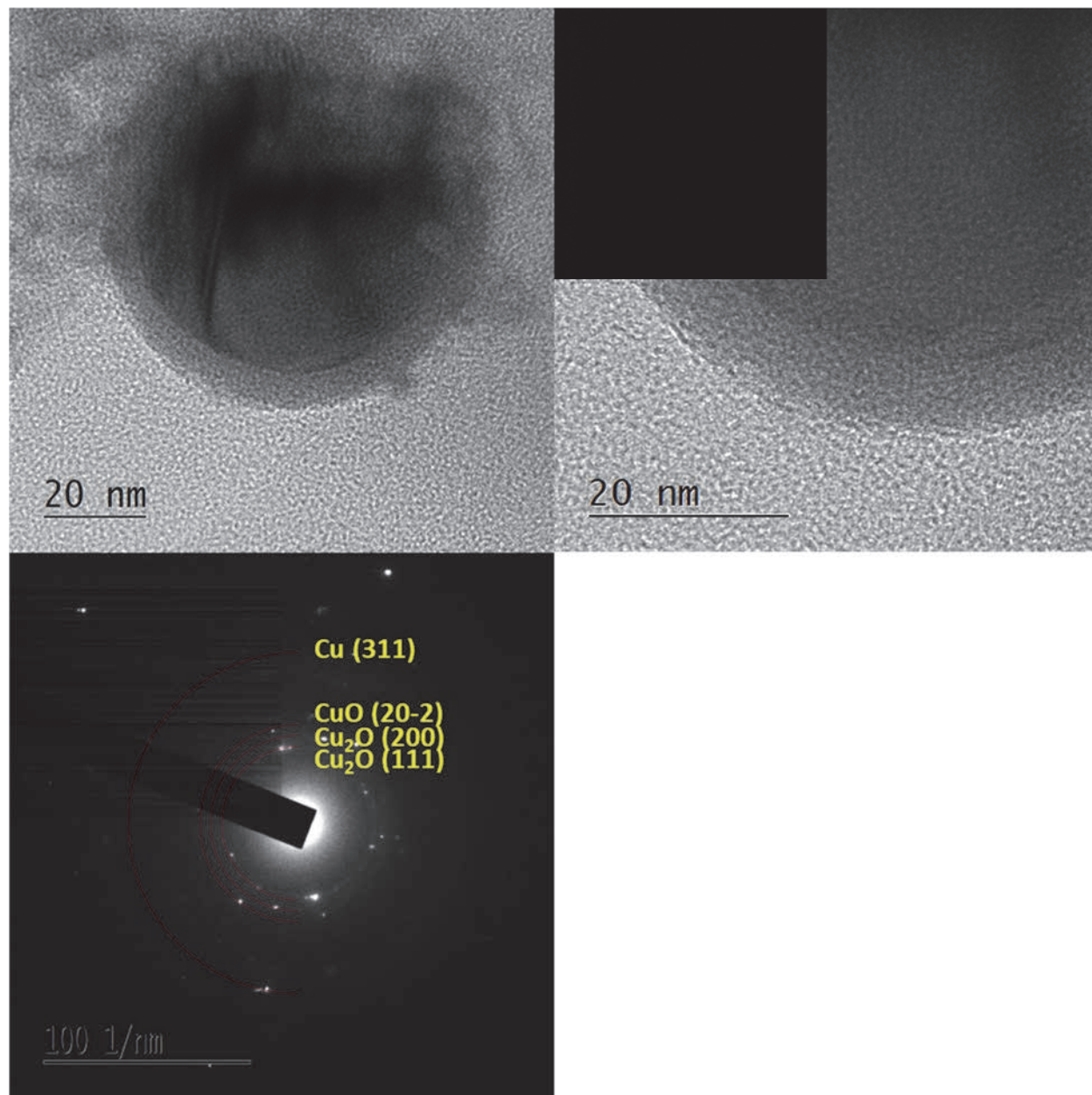
	AC 19.5 kV	DC 5 A	DC 30 A
Average particle size	1.75 $\mu\text{m}$	3.92 $\mu\text{m}$	3.38 $\mu\text{m}$
Standard deviation	0.78 $\mu\text{m}$	2.80 $\mu\text{m}$	2.48 $\mu\text{m}$

Figure 3–10, 3–11, and 3–12 are TEM images and SAED patterns of nano-sized particles produced by the bipolar power source in the variation of frequency of 20, 40, and 60 kHz. The image of the particle shown in Figure 3–10 (a) looks similar to a grain-shaped nano-sized particle on the sphere particle surface, which corresponds to the FE–SEM images in Figure 3–7 and 3–8. The lattice structure has not been clearly seen in the high-resolution TEM observation. From the SAED pattern, the characterization results show a thick cloud, which means the sample is to be an amorphous structure. Figure 3–11 shows a spherical nanoparticle with a similar shape corresponding to the FE–SEM analysis. High-resolution TEM images clearly show a layer has covered up the spherical nanoparticle surface. The diffraction pattern shows that the sample has a lattice structure. The calculated lattice distance from the scattering lights indicated the presence of metallic Cu and Cu oxides, including CuO and Cu<sub>2</sub>O. It is supposed that the surface of the metallic copper was oxidized, and the surroundings formed the oxidation film. In Figure 3–12, the spherical particle size range of 4~5 nm was observed. High-resolution TEM observations demonstrate a lattice structure inside the sphere particle. The SAED pattern shows similar trends to the 40 kHz case in which Cu, Cu<sub>2</sub>O and CuO were detected. In the liquid nitrogen discharge experiments, most of the nano-sized particles are supposed to have the oxide state forms caused by exposure to air.





**Figure 3–10.** TEM images (a, b) and SAED patterns (c) of liquid nitrogen discharge sample in the operating condition of 9 kV, 20 kHz.



**Figure 3–11.** TEM images (a, b) and SAED patterns (c) of liquid nitrogen discharge sample in the operating condition of 9 kV, 40 kHz.



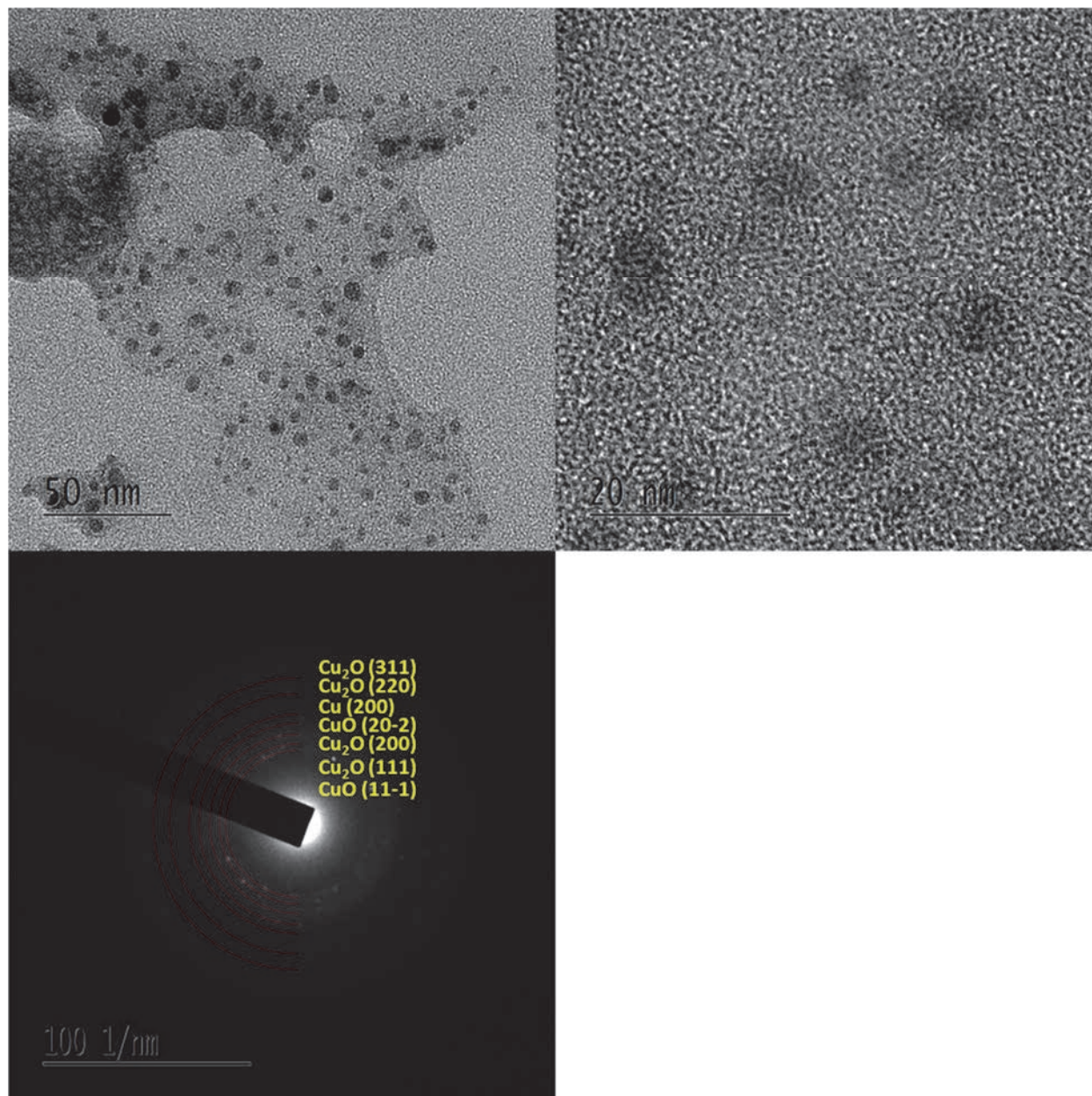


**Figure 3–12.** TEM images (a, b) and SAED patterns (c) of liquid nitrogen discharge sample in the operating condition of 9 kV, 60 kHz.



### 3.3.2 Crystallite phase of the synthesized particles

The coarse particle sample prepared by the DC power supply was characterized by XRD. The crystalline phases of the raw material (electrode surface) and the product components were identified based on the database of the PDXL software. Figure 3–13 indicates the XRD patterns of the prepared copper particles. According to the diffraction patterns shown in Figure 3–13, the samples treated by DC 5 A contained the crystallite phases of Cu (copper, PDF #00–004–0836,  $2\theta=43.3^\circ$ ,  $50.4^\circ$ ,  $74.1^\circ$ ), Cu<sub>2</sub>O (cuprous oxide, PDF #01–078–2076,  $2\theta=36.4^\circ$ ,  $42.3^\circ$ ,  $61.4^\circ$ ) and CuO (cupric oxide, PDF #00–048–1548,  $2\theta=38.7^\circ$ ). On the other hand, those treated by 30 A had metallic Cu peaks. From the XRD spectra, the Cu<sub>2</sub>O peak had a more clear intensity than the CuO peak, which meant that the particles were partially oxidized.

There might be two reasons for this. One was that oxides were produced by the oxidation of nano-sized particle, which was very sensitive to be oxidized, after the vaporization of liquid nitrogen in the room temperature. Another reason was thought to be due to the sampling procedure in the current process. During the experiments, liquid nitrogen strongly moved up and down with boiling, which made the black fumes vaporize. Some of the contents from the fume, which was thought to be fine particles, were mostly stacked uppermost around the vessel boundary, as shown in Figure 3–5.

At the end of the experiments, most of the residual particles were attached in 3 positions, the vessel bottom part, the vessel wall part below the liquid nitrogen surface, and the top edge boundary of the vessel. In the case of the 5 A current experiment, the production rate of the particle was not enough. Thus, it was hard to obtain particles. In order to make more samples, we collected the particles at the top boundary of the vessel. However, compared to the other two positions, the circumstance seemed different. The boundary part might be easier to contact with the moisture and the air. In the case of the 30, An experiment, the product amount of the sample was more than 5 A. Thus, the ratio of the Cu<sub>2</sub>O peak ( $2\theta=36.4^\circ$ ) was relatively lower, almost unnoticeable, compared to the Cu<sub>2</sub>O peak for 5 A sample.

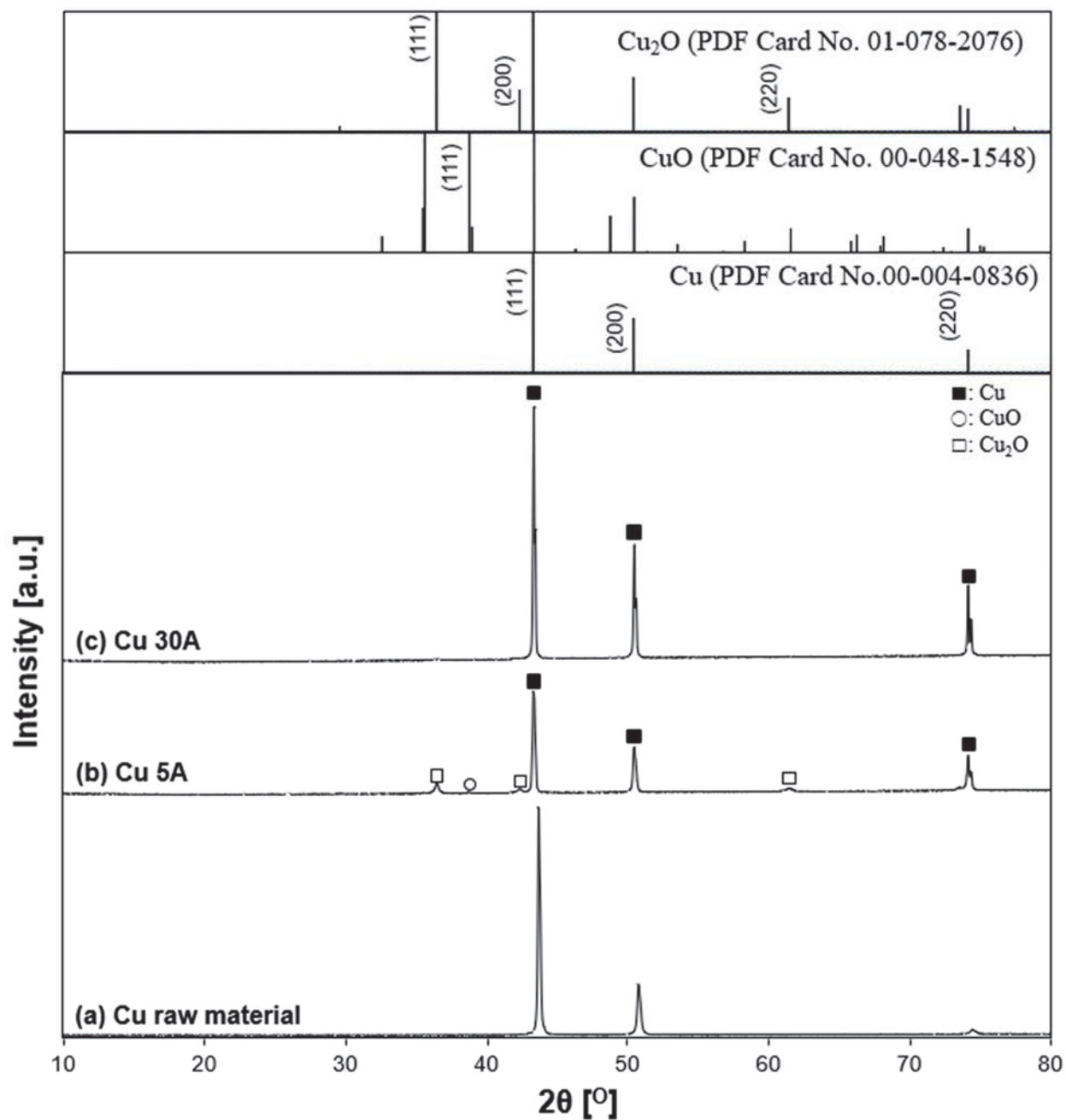


Figure 3–13. XRD patterns of samples treated by DC power.

(a) Cu raw material (electrode surface), (b) Cu treated by DC 5 A, (c) Cu treated by DC 30 A samples. The inserted figure is the PDF card of the Cu XRD patterns in the range of  $2\theta = 10^\circ \sim 80^\circ$ . Individual crystalline phases are represented by the following characteristic peaks.

( $\blacksquare$ : Cu,  $\circ$ : CuO,  $\square$ : Cu<sub>2</sub>O)

### 3.3.3 Formation phenomena of Cu/CuO/Cu<sub>2</sub>O composite in liquid nitrogen discharge

The surface structure of copper electrodes was analyzed as the product particles were considered to be derived from the electrode. Figure 3–14 and 3–15 shows the surface structure of the electrode before and after the discharges by the AC, bipolar pulse and DC power. The initial condition of the electrode has a smooth surface, although some scratches are observed from the low magnification image because of polishing as a pre-treatment to make the surface flat to adjust electrodes surface parallel.

The surface morphology trends are quite similar. However, the discharge power seems to cause a different effect on the electrodes. According to the low magnification of the SEM images, hills-like structures are observed. It is considered that the electrode was gradually heated up by the repeating partial discharges on the electrode surface. When it comes to be heated enough, and the surface becomes locally melted, it can probably form the hills. Many hills were observed in the bipolar pulse power compared to the AC power was applied to the electrode (Figure 3–14, (d, g, j)). It means that the melting part at bipolar pulse is much more significant than AC. Figure 3–15 shows the electrode surface using DC power at 30 A condition. It has much bigger hills and pore structures. High energy was concentrated in the order of DC > bipolar pulse > AC.

According to the high magnification images, the electrode surface was changed from a flat plane to hills and a sponge-like pore structure after the discharging (Figure 3–14, (f, i, l)). The created pore size shows nearly the same size as the produced spherical particle size. It seems plausible that the local molten part developed hills on the heated electrode surface, and then the discharge was concentrated on the coarse hills, which are relatively melted states. When the discharge hits the melted region, the pore structure is generated, which means partial evaporation occurred. It can be considered that the electrode surface is heated enough to partially vaporized. Furthermore, most of the hill position shows pore structure with having a molten surface.

It can also explain the mechanism of spherical particle formation in this process. Kittaka et al. [78] proposed the formation of fine spheres depends on crystal structures. The metal oxides which easily form spheres have an amorphous or polymorphous structure. In contrast, the metal oxides, which have a low tendency to form a sphere, are crystallized monomorphic. Moreover, the molten particles, which are polymorphous, will have a diverse crystal structure. In contrast, monomorphic molten particles, which should have an isotropic property, form spherical particles due to the surface tension. They also discussed other research of fine spheres obtained by the plasma torch method, for their comparison results. They discussed the report of Barry et. al. [79]. In the report, they used plasma torch, which was the temperature reach to 5,000 K. Due to the fast quenching rate, Kittaka et al. suggested that the formation of sphere liquid droplets would be quenched as particles with the anticipation of lost ordered structure.

In our research, the micro-size Cu molten droplet and vaporized nano-size Cu metal clusters were concentrated to form a sphere shape to reduce the surface tension. Based on the SAED pattern results in Figure 3-10, some of the nano Cu particles seem to have an amorphous structure due to the fast quenching.

The average particle size data revealed that the particle from the DC power source, which had more energy concentrated on the electrode surface, brought a larger size of the particles than those formed by AC power sources. Saito et al. explained the formation mechanism for the melting in full plasma, melting in partial plasma, and vaporizing in partial plasma with relation to the particle size [80]. It is plausible to follow that the intensive energy of the DC power on the electrode surface produces bigger particles than the AC and the bipolar pulse power.

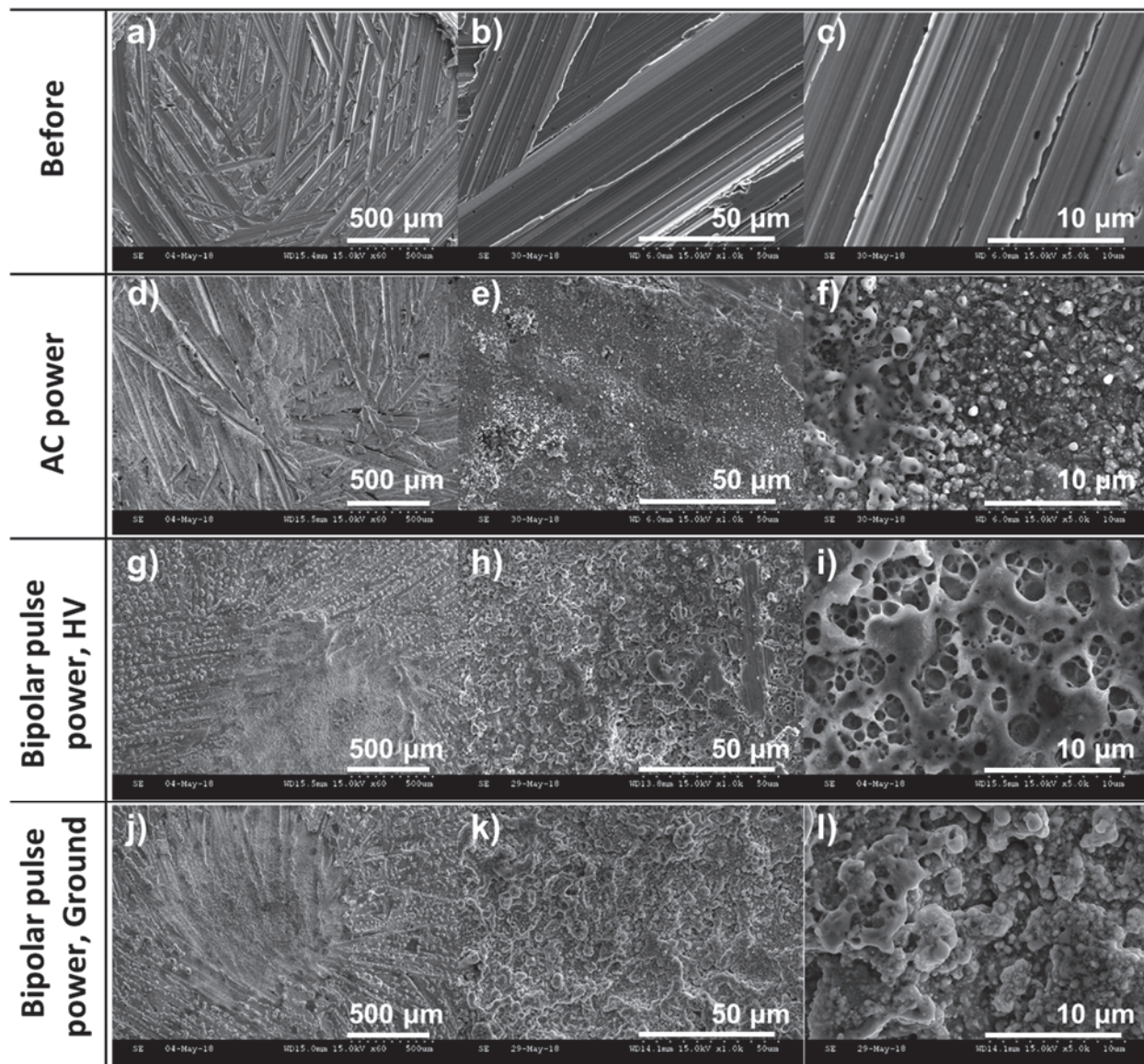


Figure 3–14. Surface structure change of Cu electrodes after discharge by AC and bipolar pulse power



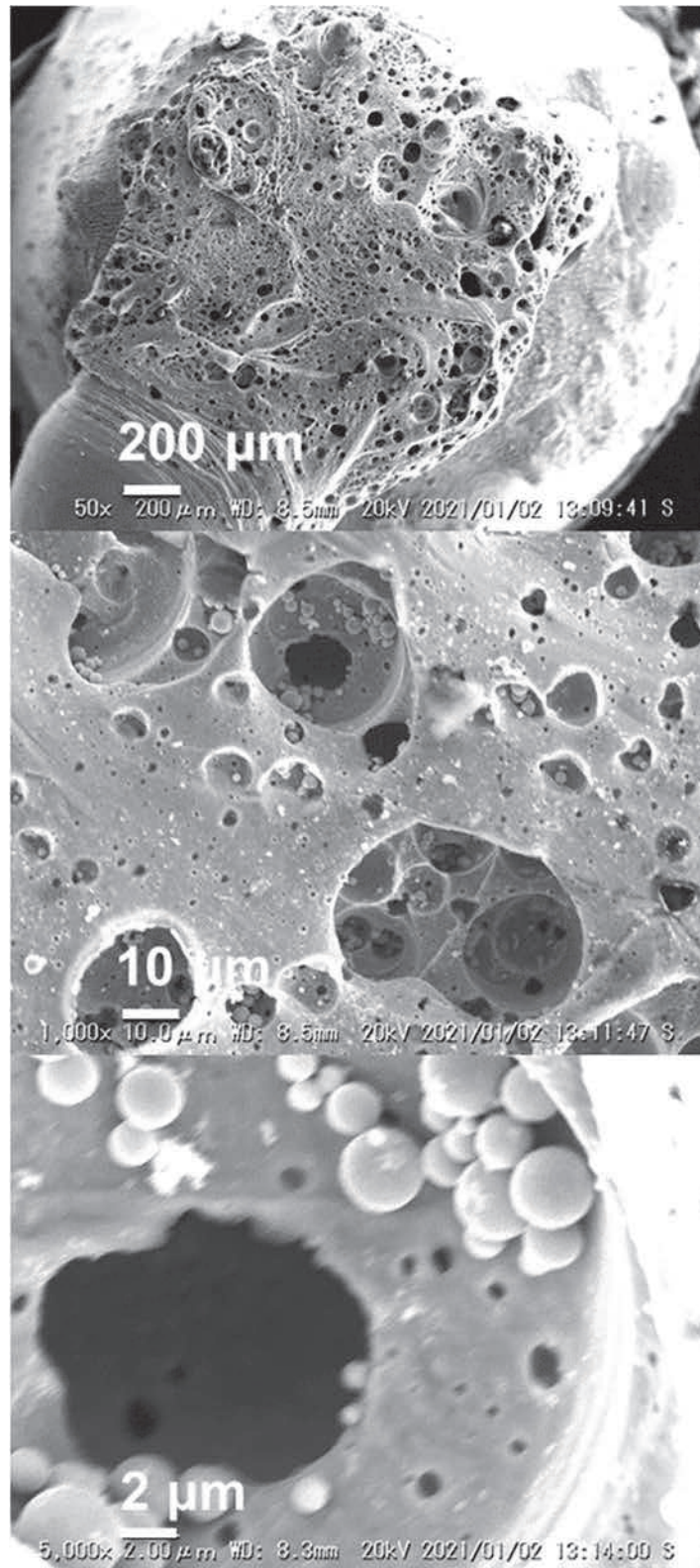


Figure 3–15. Surface structure change of Cu electrodes after discharge by DC 30 A

### 3.4 Summary

The electrical discharge was successfully maintained under liquid nitrogen using AC, bipolar pulse, and DC power supply. Micro- to nanometer size of the metallic copper (Cu) and copper oxides (CuO, Cu<sub>2</sub>O) particles were synthesized from the erosion of copper electrodes, and their morphologies differed independence on the dielectric media. Regardless of the variation of the power supplies, the produced particles have a spherical shape in common when discharge in liquid nitrogen. The spherical is a common shape in particle generation since the particle itself tries to minimize the surface tension of the particle.

According to the XRD analysis, copper particles are in a metallic copper state. However, in the nano-sized case, SAED patterns showed that the particle seems to be easily oxidized to form CuO and Cu<sub>2</sub>O when exposed to air.

The particle formation mechanism is considered to proceed by local melting and partial vaporization. The micro-size spherical coarse particles may directly be detached from the molten surface of the electrode. Moreover, the nano-size spherical fine particles may be generated by partial vaporization from the electrode. The DC power supply shows the best particle production ability as compared with AC and bipolar pulse power supplies.

# **CHAPTER 4**

## **Variation in metal electrodes for the particle preparation using liquid nitrogen discharge**



## 4.1 Introduction

The liquid nitrogen discharge with Cu electrodes was investigated in the previous chapter using different power supplies (AC, bipolar pulse, and DC). For comparison, DI water discharge was also examined for copper particle preparation. It seems that hydroxyl ions participated in the electrochemical reaction with copper in Chapter 2. However, Cu did not participate in any chemical reaction in a liquid nitrogen medium, in Chapter 3.

In Chapter 4, three kinds of metal electrodes, including titanium (Ti), aluminum (Al), and zinc (Zn), were chosen as expected to react with liquid nitrogen and synthesize nitride particles. Three electrodes were performed as a raw material for particle preparation in liquid nitrogen discharge. The experiment using different metal configurations of anode and cathode was also conducted to better understanding particle formation characteristics. Based on the experimental results, the reaction between liquid nitrogen and metal electrodes (Al, Ti, and Zn) was discussed. The reaction between dielectric media (liquid nitrogen and DI water) and the metal electrodes (Al, Cu, Ti, and Zn) can be discussed at the end of this chapter. Since the AC and bipolar pulse power produced very scarce particles, which eventually led to difficulties characterizing the particles. In this aspect, the DC power supply was employed for particle preparation in liquid nitrogen.

## 4.2 Experimental

### 4.2.1 Experimental setup

The experimental setup is the same as in Chapter 3.2.3. A schematic diagram of the DC arc discharge system is depicted in Figure 3-4. The pictures of the experimental apparatus consisted of a DC power supply (YE-200BL3, Panasonic, Japan) are shown in Figure 3-5. DC power supply was employed to generate arc discharge in liquid nitrogen. The electrical discharge was generated using Al, Ti, Zn rods (Nilaco Co., Japan) with a diameter of 3 mm, immersed in

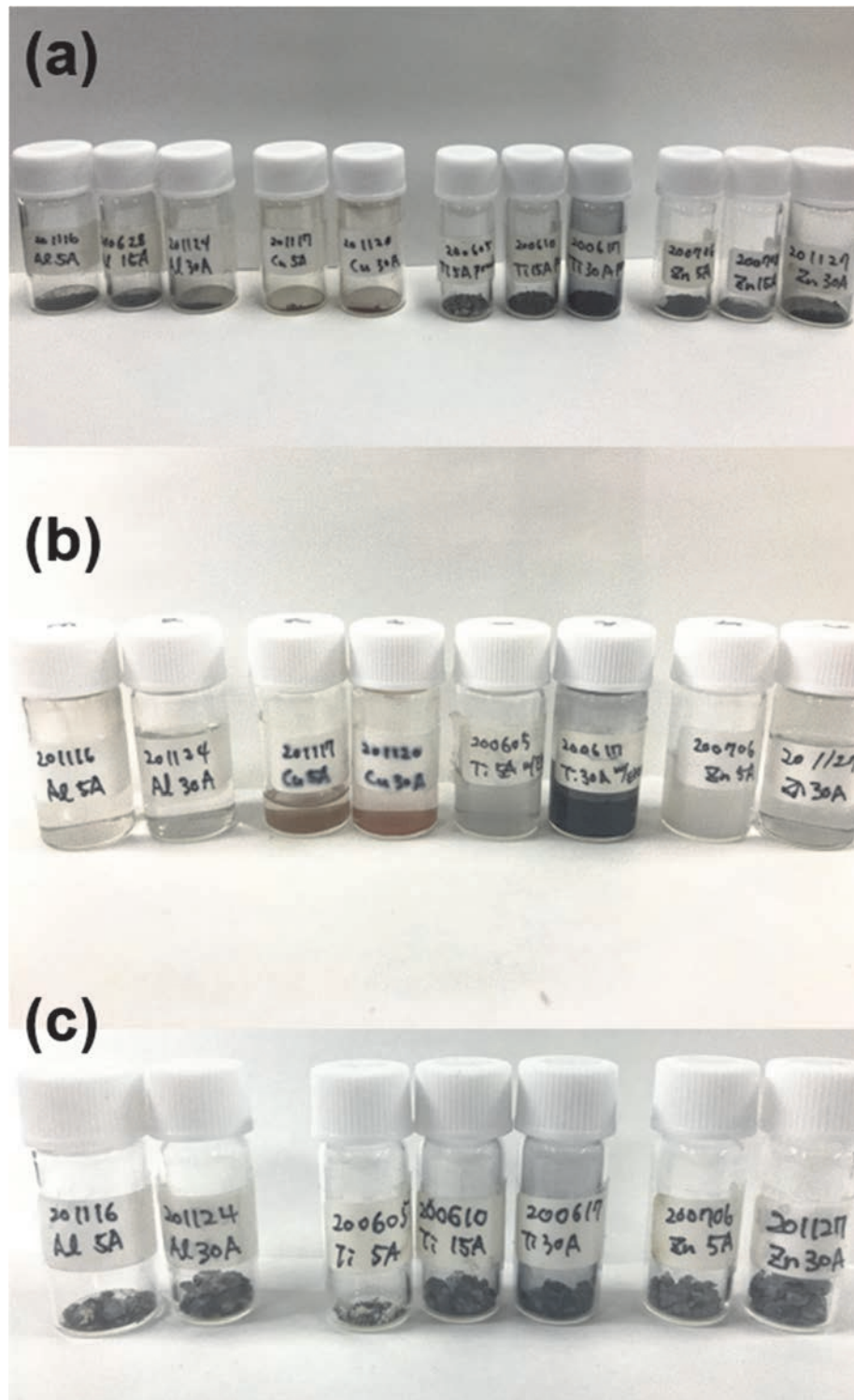
liquid nitrogen as a dielectric medium. The discharge was generated between two electrodes in a vertical arrangement. The upper electrode was the anode (+) and situated on the holder connected with the millimeter controller to set the vertical position of the anode. The bottom positioned electrode was the cathode (-) and held by an electrode holder cell. Applied current was the main process parameter using the DC power supply. The operating condition of current varying from 5 A to 30 A was applied to the electrodes. The details are shown in Table 4-1.

**Table 4-1.** Experimental conditions

<b>Content</b>	<b>Conditions</b>	
Dielectric medium	Liquid nitrogen	
Electrode material	Titanium rod, aluminum rod, and zinc rod	
Power supply	DC	
Power mode	Low-Power mode	High-Power mode
Applied current [A]	5	30
Material – Material	Ti–Ti	Ti–Ti
(+) anode – (-) cathode	Al–Al	Al–Al
	Zn–Zn	Zn–Zn
		Ti–Cu
		Cu–Ti

#### **4.2.2. Materials and method**

The experimental procedure for the synthesis of the particle is the same as in Chapter 3.2.4. The three types of samples were collected similarly described in Chapter 3.2.3. For the characterization of the prepared samples, coarse particles were characterized with XRD, while fine particles were observed with FE-SEM. Pictures of the samples is shown in Figure 4-1. A specification and physical properties of the Ti, Al, Zn electrodes were indicated in Table 4-2. The physical properties of nitrides materials and their applications are also described in Table 4-3.



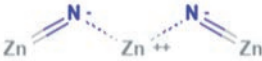


**Figure 4-1.** Pictures of the prepared samples. (a) Coarse particles from liquid nitrogen discharge using DC power, (b) Some samples of fine particles dispersed and collected by ethanol, (c) debris

**Table 4-2.** Specification and physical properties of the electrode materials

	Al	Ti	Zn
Rod diameter [mm]	3	3	3
Purity [%]	99.99	99.5	99.99
Crystal structure	fcc (Face-centered cubic)	hcp (Hexagonal close-packed)	hcp (Hexagonal close-packed)
Melting point [K]	933.45	1,940	693
Boiling point [K]	2,793	3,634	1,180
Heat of fusion [kJ/mol]	10.71	14.15	7.32
Heat of vaporization [kJ/mol]	284	425	115
Molar heat capacity [J/(mol·K)]	24.2	25.06	25.47
1 <sup>st</sup> Ionization energy [kJ/mol]	577.5	658.8	906.4
Thermal expansion [ $\mu\text{m}/(\text{m}\cdot\text{K})$ ]	23.1	8.6	30.2
Thermal conductivity [W/(m·K)]	237	21.9	116

**Table 4-3.** Physical properties of the nitride materials and their applications [81–90]

	AlN	TiN	Zn <sub>3</sub> N <sub>2</sub>
Chemical Structure			
Crystal structure	Wurtzite	Cubic	Cubic
Appearance	White to pale-yellow	Golden color	Blue-gray cubic
Melting point	Dissociates 2,773 K	3,220 K	Decomposes 973.15 K
Applications	Dielectric layers in optical storage media Military aeronautics Heat exchange system Optoelectronics Electronic substrates Steel and semiconductor manufacturing	Machine tooling Aerospace and military application Diffusion barrier Medical implants BioMEMS	Thin film transistor Sensors for humidity indicator

### 4.2.3 Characterization

The crystalline phases of the coarse particle samples and electrodes were investigated by X-ray diffraction (XRD, Mini Flex 600, Rigaku, Japan), which was operated with a Cu K $\alpha$  source at 40 kV and 15 mA. In analyzing the surface properties of the electrodes, a special sample holder was used to fixing the position. The samples were measured in the scanned range of  $2\theta$  from  $10^\circ$  to  $80^\circ$  degrees with a step size of  $0.02^\circ$ . The measurement scan rate was  $5^\circ/\text{min}$ . All samples were measured more than twice to confirm for any aging effects after exposure to air for several weeks. The obtained XRD peaks were assigned based on the database of PDXL software (Rigaku, Japan).

The crystallite size was calculated from the measurement data using the Scherrer equation as follows:

$$D = \frac{K\lambda}{\beta \cos\theta} \quad (4-1)$$

where  $D$  is crystallite size,  $K$  is a shape factor that varies with the actual crystalline shape determined as 0.9 here (0.94 for the cubic),  $\lambda$  is X-ray wavelength (for Cu K $\alpha$ ,  $1.540598\text{\AA}$ ),  $\beta$  is full width at half maximum (FWHM) of a peak and  $\theta$  is half of  $2\theta$  at the peak.

Eq (4-2) is used to calculate a lattice parameter  $a$  of a cubic unit cell where  $d$  is a lattice spacing calculated as in Bragg's law Eq (2-1), and  $h$ ,  $k$ , and  $l$  are Miller indices of a corresponding plane.

$$d_{hkl} = \frac{a}{\sqrt{h^2+k^2+l^2}} \quad (4-2)$$

The surface morphologies of the obtained particles and electrodes were observed with a scanning electron microscope (SEM, VE-9800, Keyence, Japan) to study the effects of electrical discharge on electrodes. The images were collected at 20 kV conditions. Two kinds of field emission scanning electron microscope (1. FE-SEM, SU9000, Hitachi, Japan, 2. FE-SEM, JSM-7500F, Jeol, Japan) were also used for high magnification observation. In operation with SU9000, Al samples were coated with osmium (Os) with around 5 nm thick using Os plasma coating (Neoc-pro) prior to observing the samples. In the case of Ti samples, the existence of the nitrogen species was examined using energy-dispersive spectroscopy (EDS, Ametech, Genesis-APEX) operated at 30 kV.

### 4.3 Results and discussion

#### 4.3.1 Synthesis of Al/AlN particles

##### 4.3.1.1 Morphologies of prepared Al-based nanoparticles

Morphologies of the synthesized nanoparticles were investigated using two kinds of FE-SEM (SU9000 and 7500F). Figure 4-2 shows FE-SEM images of prepared Al-based nanoparticles at different current modes with x50,000 and x100,000 magnification views. The majority of the particles were formed in a spherical shape in the observation. The particles in this figure were not pre-coated with conductive materials. Thus, the boundary of the particle seems sharp and clear even though the image has a low resolution compared to the osmium-coated particles in Figure 4-3. The average diameter of the spherical particle was measured using obtained images from FE-SEM. A hundred of the spherical particles were selected randomly, and the diameter was measured. The size distribution of the prepared Al-based nanoparticles is shown in Figure 4-4, and the measured average particle size was listed in Table 4-4. The prepared Al-based nanoparticles by low current mode showed an average size particle around 25.77 nm, while the high current mode sample was measured around 46.31 nm. The Al-based nanoparticles with relatively uniform size were prepared in the low current mode. The calculation results show that the high current mode using DC seems to affect the heating of the

**Chapter 4. Variation in metal electrodes for the particle preparation using liquid nitrogen discharge**

electrode surface. This leads to forming a relatively larger particle size in the particle growth step and the broad size distribution of the synthesized particles.

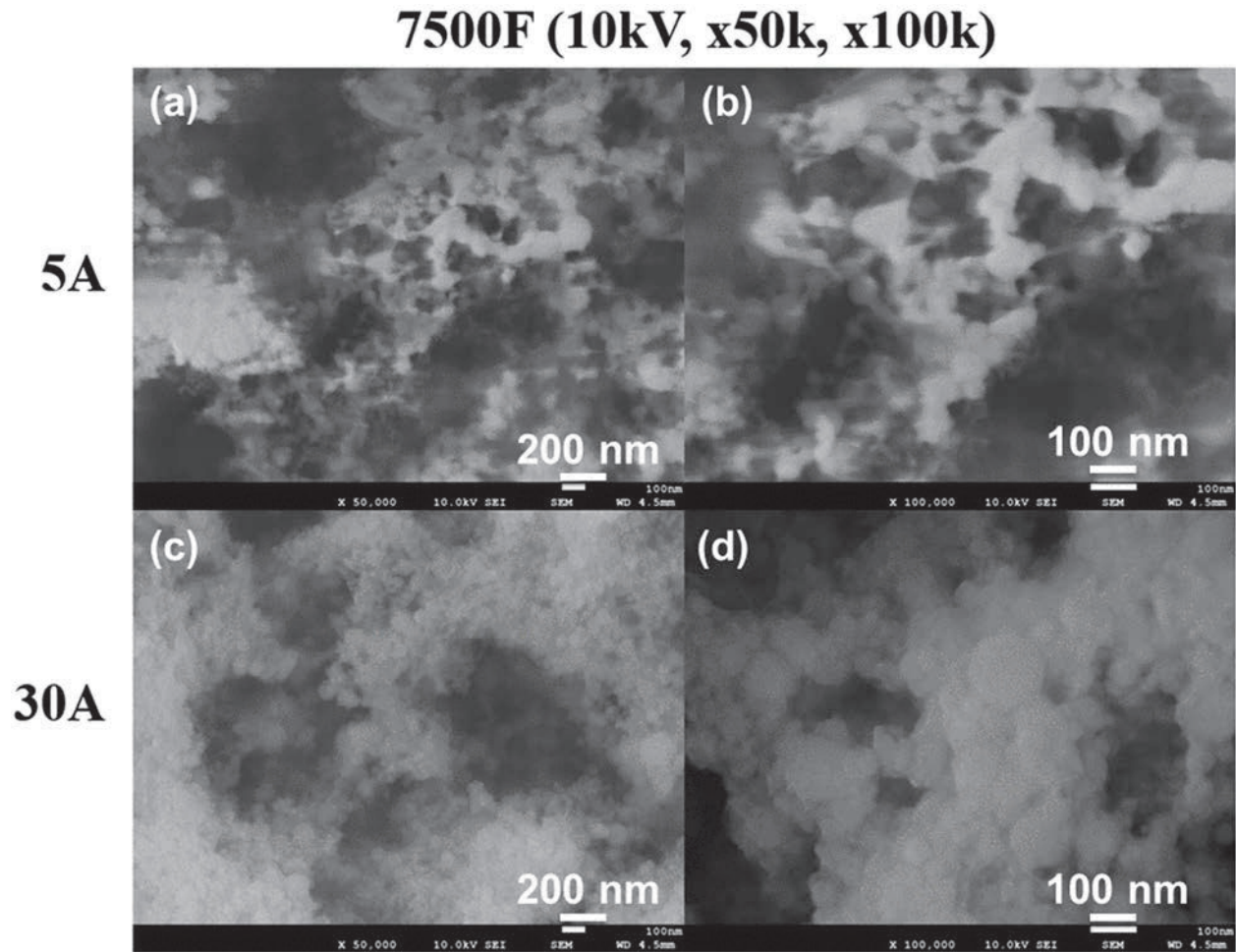


**Figure 4-2.** FE-SEM images of Al-based nanoparticles without osmium coating (a, b) low current mode, Al 5 A, and (c, d) high current mode, Al 30 A



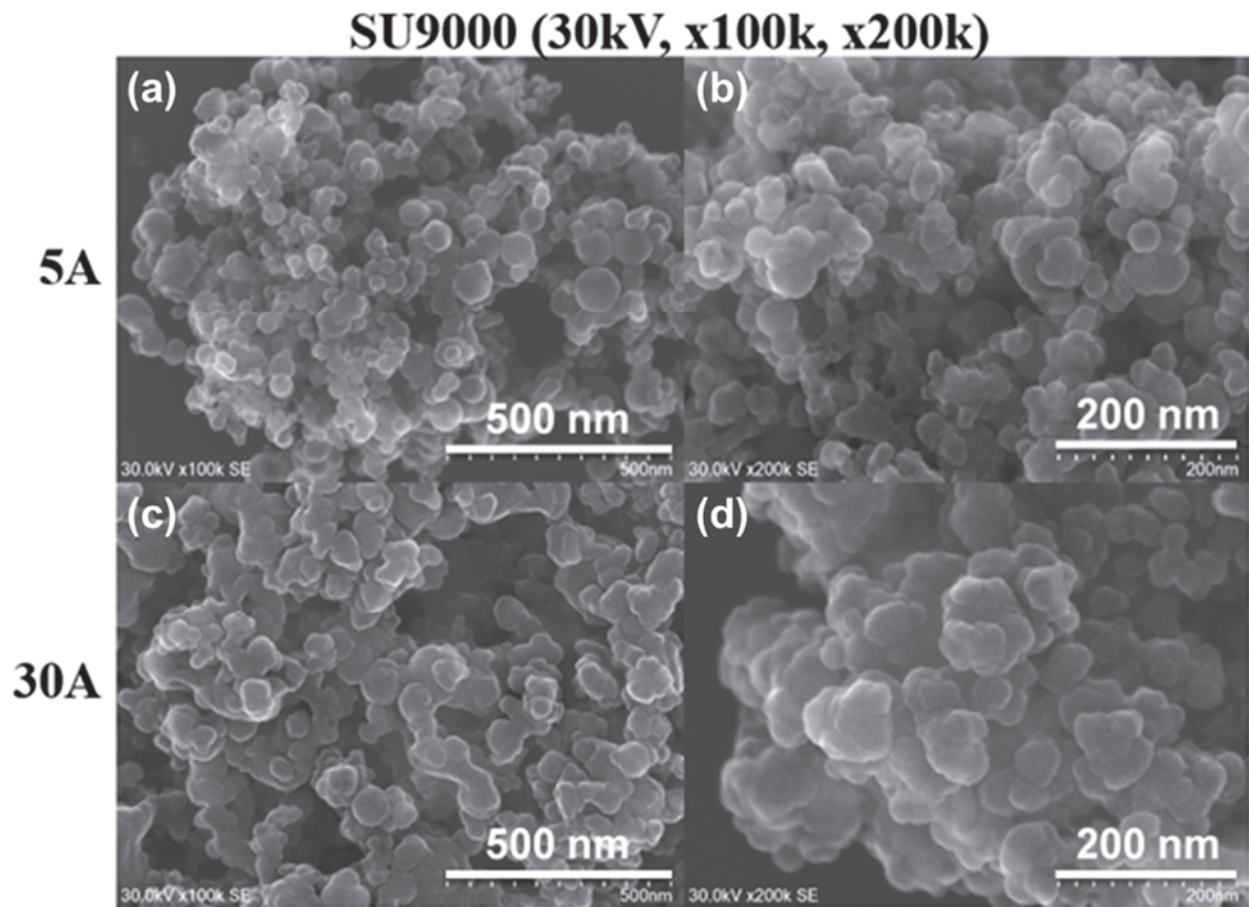


**Figure 4-3.** FE-SEM images of Al-based nanoparticles with osmium-coated sample. (a, b) the low current mode, Al 5 A, and (c, d) high current mode, Al 30 A



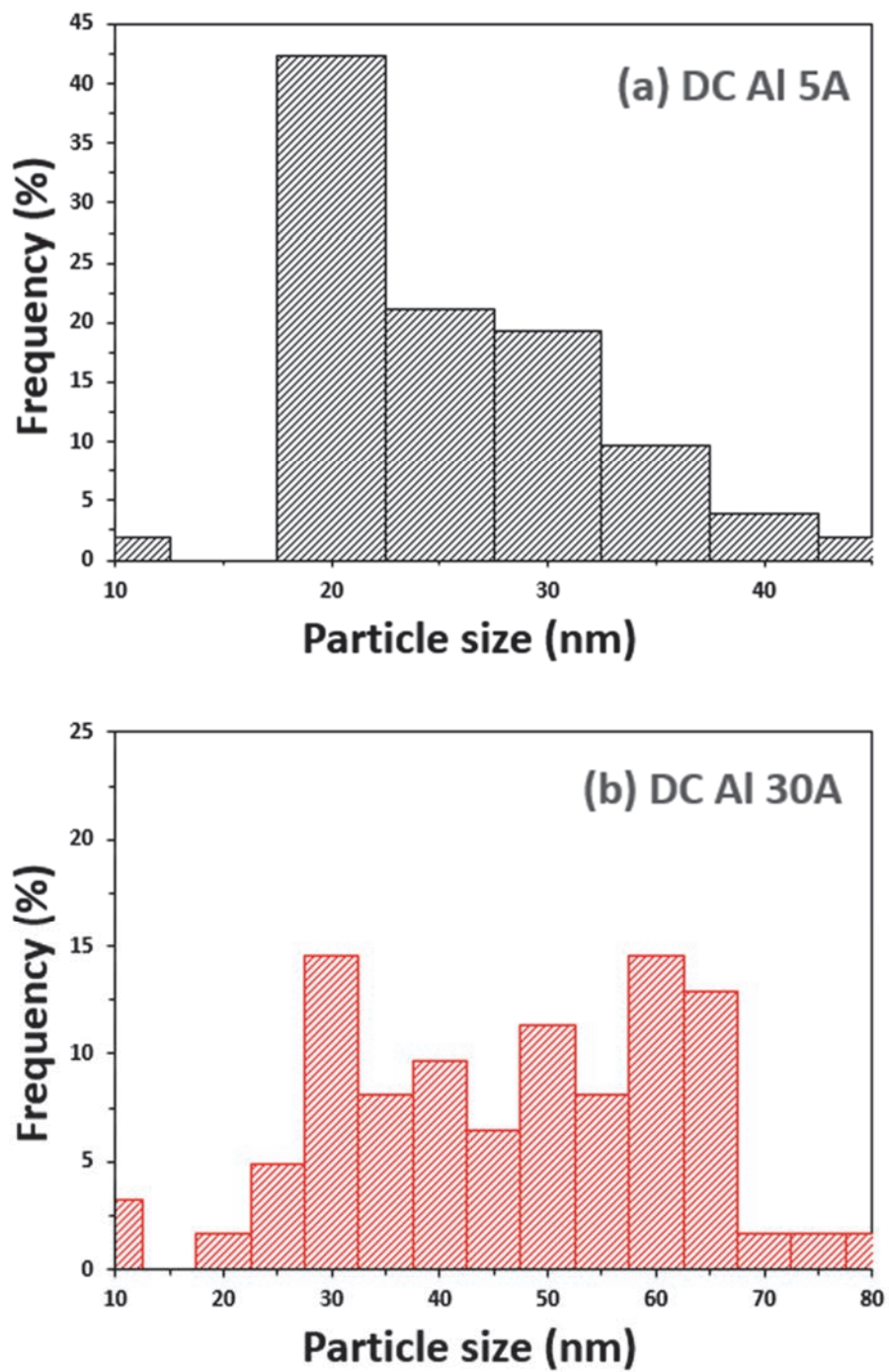


Figure 4-4. Particle size distribution of prepared Al-based nanoparticles, (a) low current mode, Al 5 A, and (b) high current mode, Al 30 A

**Table 4-4.** Average particle size and standard deviation of prepared Al-based particles depending on the current mode

	Low current mode (5 A)	High current mode (30 A)
Average particle size [nm]	25.77	46.31
Standard deviation [nm]	6.67	15.61

#### 4.3.1.2 Crystallite phase of the synthesized Al/AlN particles

Figure 4-5 shows the XRD patterns of the prepared Al-based particles with variable currents of 5 A, 15 A, and 30 A. According to the characterization results, Al and AlN were the main components in both low- and high-current modes. The XRD pattern (a) indicates the peaks of the initial state of the Al electrode surface, which was used as a raw material in this experiment. The peaks of the AlN (Aluminum nitride, PDF #00-066-0534,  $2\theta=33.22^\circ$ ,  $36.05^\circ$ ,  $37.94^\circ$ ,  $49.83^\circ$ ,  $59.36^\circ$ ,  $66.07^\circ$ ,  $69.75^\circ$ ,  $71.45^\circ$ ,  $72.64^\circ$ ,  $76.48^\circ$ ) appeared in every experimental condition. The XRD patterns showing a trend that when it goes to the high current condition, the intensities of AlN peaks are increased while those of Al peaks decreased. However, in Al 30 A sample, unreacted Al still remains. The results indicate that the crystallinity of synthesized AlN was enhanced with increasing the high current up to 30 A conditions. This explains that the current as a variable has an influence on the crystallinity of the synthesized AlN as well as the productivity of the AlN particles.

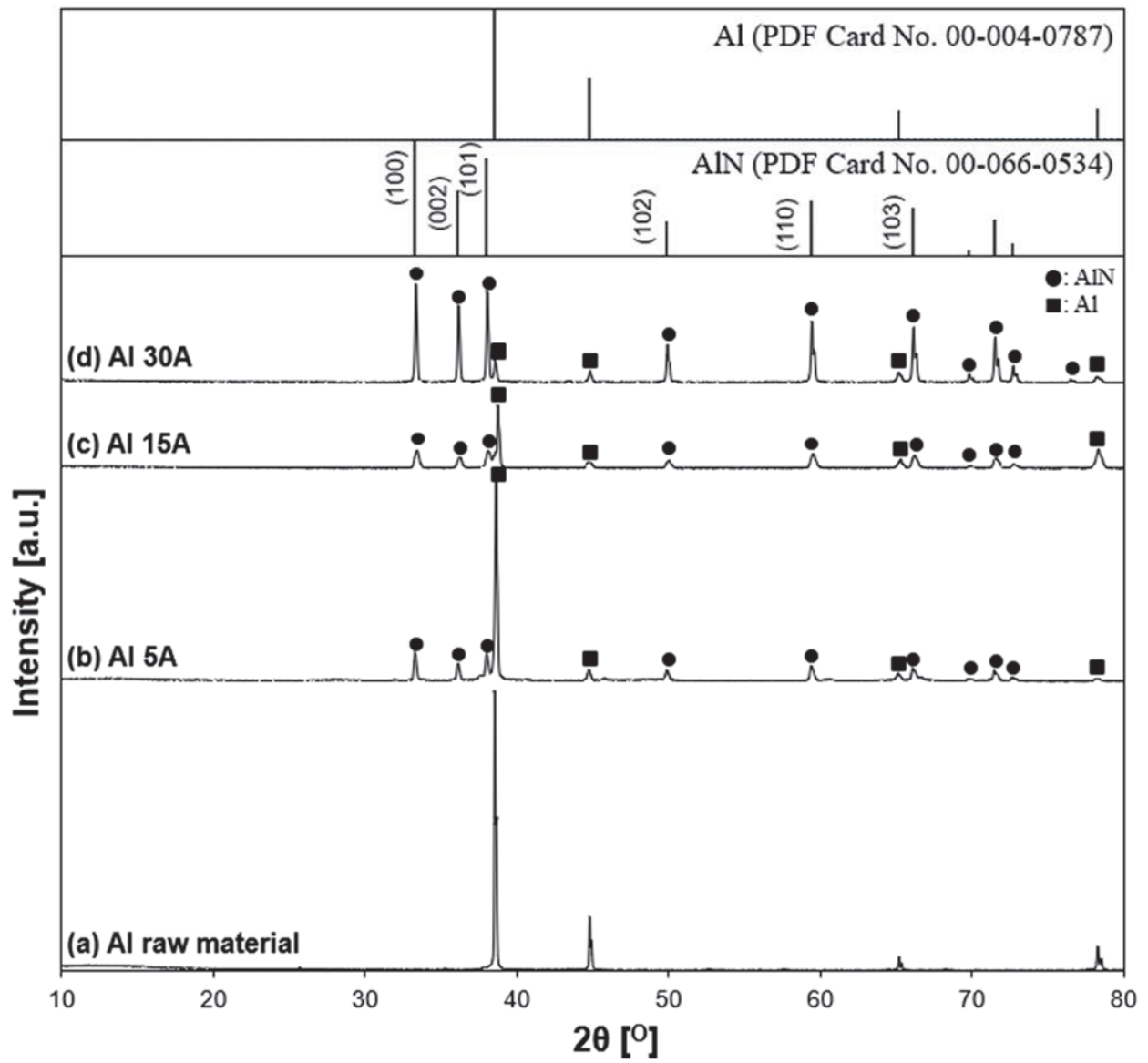


Figure 4-5. X-ray diffraction patterns of synthesized samples. (a) Al raw material (b) Al 5 A, (c) Al 15 A, (d) Al 30 A, (●) AlN, (■) Al

### 4.3.2 Synthesis of TiN particles

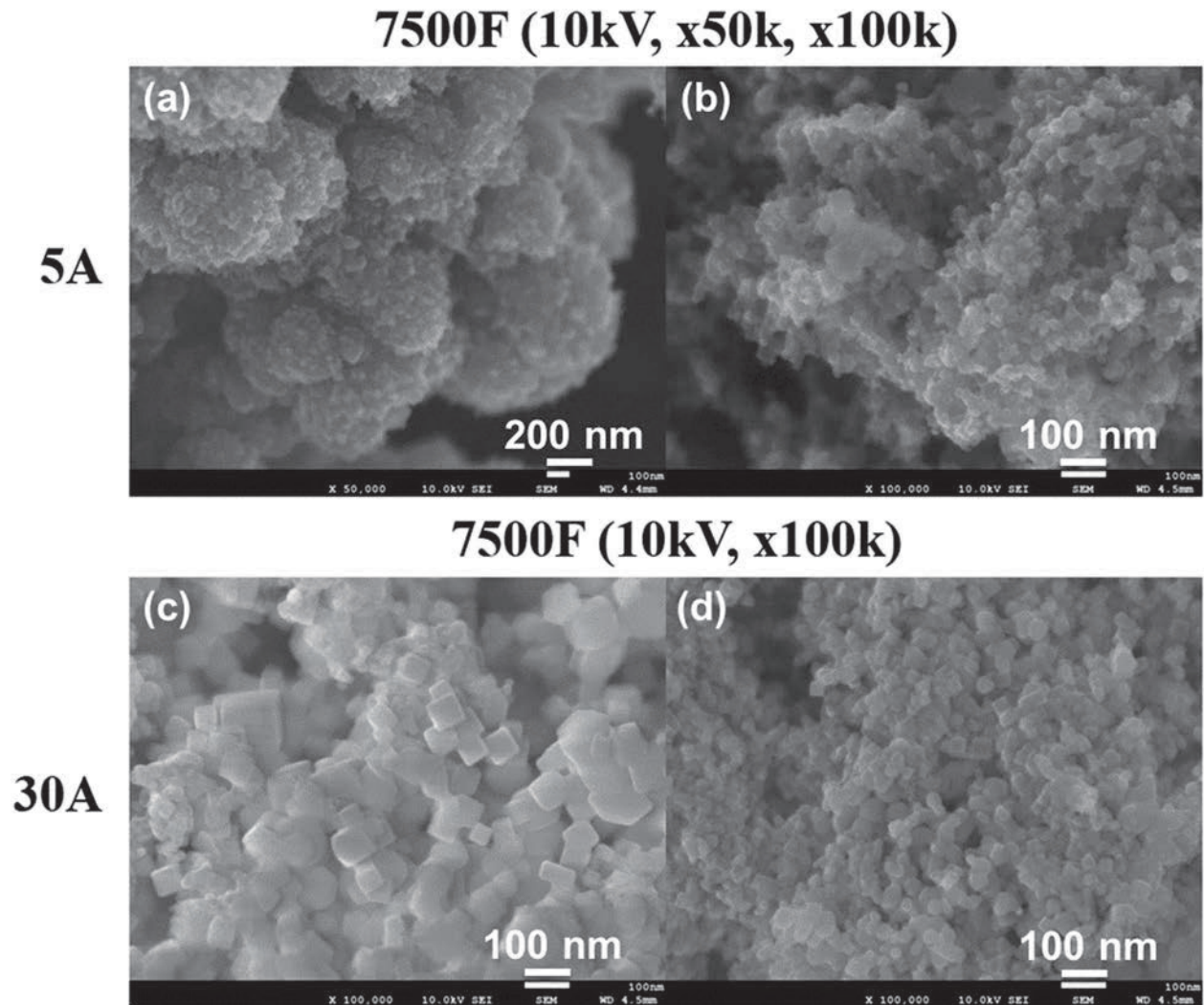
#### 4.3.2.1 Morphologies of the prepared Ti-based nanoparticles

Figure 4-6 and 4-7 shows the morphology of the prepared Ti-based nanoparticles in liquid nitrogen discharge. From the images, two types of morphologies are observed, cubic and spherical particles. The morphologies are not clearly divided by the current conditions. However, the cubic particles were mainly synthesized in the 30 A condition, while the spherical particle is mainly synthesized in 5 A.

In order to confirm the component of cubic particles, EDS elemental mapping was conducted during the FE-SEM observation. In Figure 4-8, the presence of nitrogen elements on the surfaces of Ti 5 A and Ti 30 A was confirmed. Comparing with the 5 A and 30 A samples, the nitrogen element represented by red dots were finely dispersed in the 30 A condition, while a relatively very weak nitrogen signal was shown in the 5 A sample.

The average size particle was measured in the same procedure as in Al samples. The size of the cubic particle was calculated based on the length of the longest diagonal. A diagonal length of the cube was calculated as  $a\sqrt{3}$ , when 'a' is the length of the sides in the cubic. Figure 4-9 and Table 4-5 show the size distribution of the nanoparticles and their average size. The measured cubic particles seem to have an average size of 43.16 nm with a standard deviation value of 22.50 nm.

From the other studies, they mentioned that the cubic nanoparticles were identified to titanium nitride (TiN) as they were synthesized by wire explosion and other plasma methods [91-93] using nitrogen gas as a dielectric. The rapid synthesis method may be one of the key factors related to form the cubic TiN particles. To identify the component of the prepared samples, XRD analysis was performed.



**Figure 4-6.** FE-SEM images of prepared Ti-based nanoparticles. (a, b) the low current mode, Ti 5 A, and (c, d) high current mode, Ti 30 A

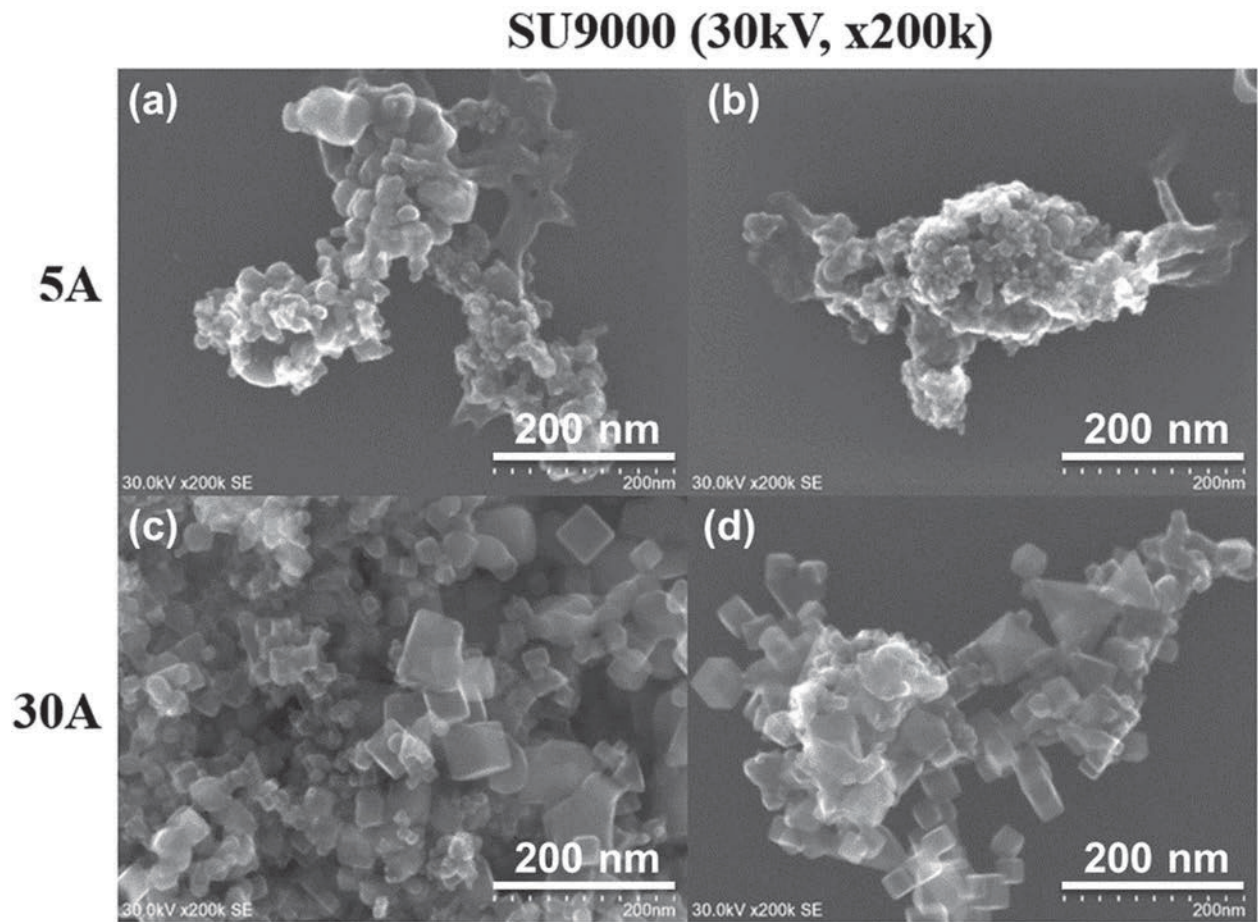


**Figure 4-7.** FE-SEM images of prepared Ti-based nanoparticles. (a, b) the low current mode, Ti 5 A, and (c, d) high current mode, Ti 30 A



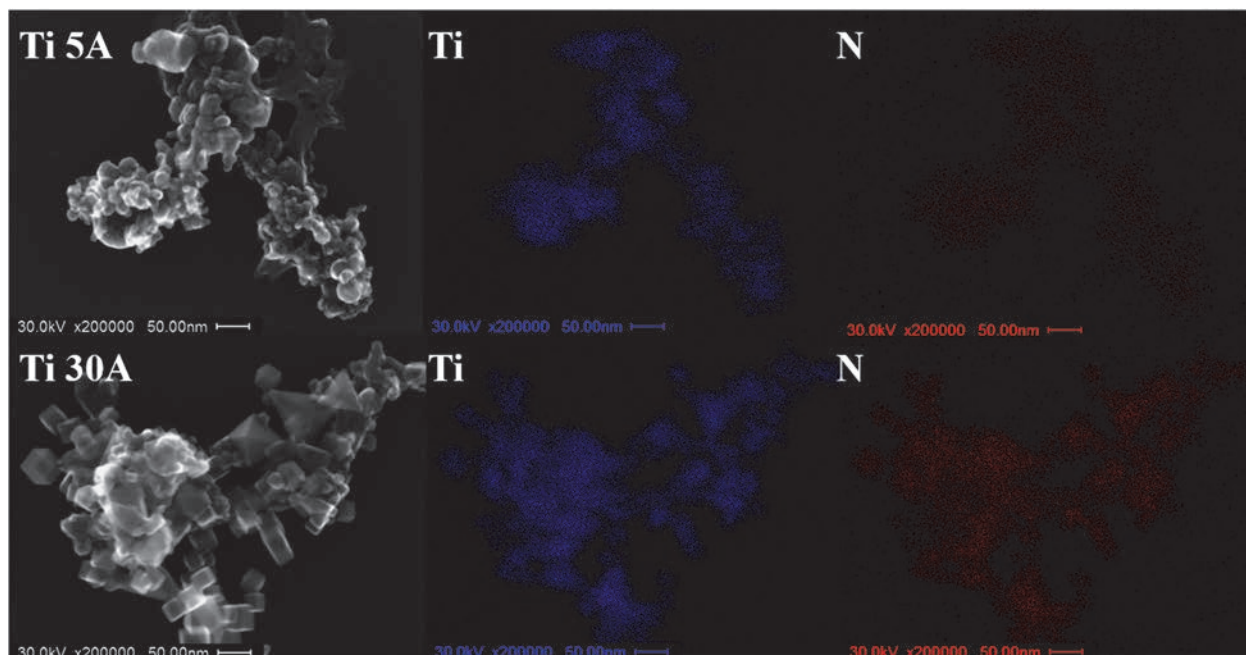


**Figure 4-8.** FE-SEM images (left) and EDS mapping images of the prepared samples. Low current mode, Ti 5 A (upper) and high current mode, Ti 30 A (bottom)

**Table 4-5.** Average particle size and standard deviation of prepared Ti-based particles depending on the current mode

	Low current mode (5 A)	High current mode (30 A)
Average particle size [nm]	30.04	43.16
Standard deviation [nm]	22.44	22.50

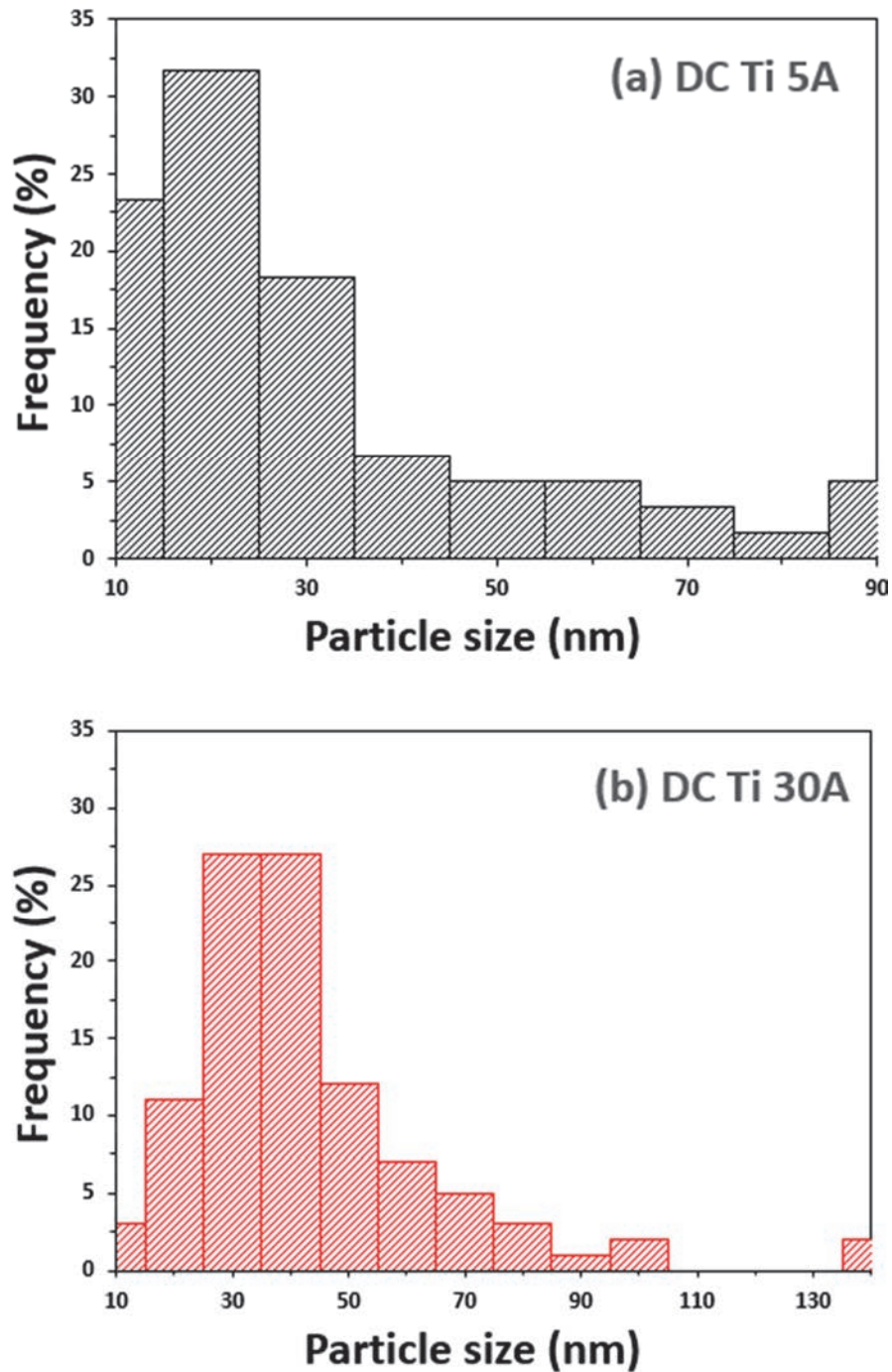


Figure 4-9. Particle size distribution of Ti-based nanoparticles, (a) low current mode, Ti 5 A, and (b) high current mode, Ti 30 A



### 4.3.2.2 Crystallite phase of the synthesized TiN particles

The XRD patterns of the synthesized TiN particles at currents of 5 A, 15 A, and 30 A are indicated in Figure 4–10. The initial Ti electrode surface of the XRD peak is confirmed as a reference. The presence of TiN (Osbornite, syn, PDF #00–038–1420,  $2\theta=36.66^\circ, 42.60^\circ, 61.81^\circ, 74.07^\circ, 77.96^\circ$ ), which is known as osbornite, the natural structure of titanium nitride found in meteorites [91], is confirmed in every experimental condition in the ranges of 10 to 80,  $2\theta$  degree. According to the XRD patterns, Ti pure metal peaks do not appear after the discharge, which means that Ti seems to react with nitrogen and produce TiN. The crystalline phase of  $\alpha$ -TiN<sub>0.3</sub> was identified in the 5 A and 15 A conditions. It seems that a large amount of nitrogen was dissolved into the melting titanium during discharge. This can be attributed to the low nitridation of Ti as an intermediate for the TiN nitridation process. Moreover, some of Ti were exposed to air and formed TiO<sub>2</sub>, which was a side reaction after the experiment. As a higher current of 30 A was applied to the electrode, the oxide peak intensity was decreased while the nitride peak intensity increased. The results also indicate that the crystallinity of synthesized TiN was enhanced with increasing the current up to 30 A, high current mode. In the high current mode, all the peaks were turned into TiN peaks. The crystallite TiN was produced in the high current modes compared to the low current modes of 5A and 15A. The XRD patterns are in good agreement with the FE-SEM images in Figure 4–6 to 4–7, which shows a proportional increase in the number of cubic particles when the current conditions increase 5 A to 30 A.

Wriedt et al. introduce the following equation Eq (4-3) to calculate the nitrogen content of TiN on its lattice parameter [94].  $a$  is the lattice parameter and  $x$  is the atomic percent of nitrogen. The lattice parameter can be calculated using Eq (2-2) and Eq (4-2).

$$a = 0.4159 + 0.000164x \quad (4-3)$$

#### Chapter 4. Variation in metal electrodes for the particle preparation using liquid nitrogen discharge

In order to calculate the lattice parameter of the synthesized TiN, the miller indices of the TiN peaks were indexed from the JCPDS pdf card references. The PDF card number is put on the upper side of the XRD figure.

TiN has a cubic crystal structure in the form of NaCl, and based on this cubic structure, the surface energy of each plane was calculated and reported by Oh et al. who suggested (200) planes have the lowest surface energy compared to (111) planes in the TiN thin film growth [95]. A similar study was made independently by Zhao et al. [96]. At the initial step of TiN film growth, the (200) orientation is preferred, and surface energy was a dominant factor. When the film grows to a certain level, strain energy becomes the dominant factor, and the preferential facet is changed to (111) instead of (200).

Based on the XRD patterns of Ti-Ti samples in Figure 4-10, the miller index information provides that when increasing current from 5 A to 30 A, the intensity of TiN (200) peak increases, which indicates that crystal growth proceeded preferentially on to the orientation of (200) in TiN particle formation in this step. According to Oh and Zhao's previous study, this result infers that TiN particles synthesized by liquid nitrogen discharge would be at the initial stage of particle growth. Also, it might be considered that the rapid cooling of surrounding liquid nitrogen has an effect on controlling the particle size.

The calculated nitrogen content was summarized in Table 4-6. In the determination of the lattice constant, the single-crystal phase of the osbornite in the range of  $2\theta = 10^\circ$  to  $120^\circ$ , (111), (200), (220), (311), (222), (400), (331), (420) were represented. The lattice constant was measured and calculated by averaging all values from each diffraction peak of the plane. The lattice constant calculated at the 30 A condition was 4.2334 Å in this experiment. This value is around 45 atomic percent, which is in good agreement with the standard reference value, 4.2417 Å (JCPDS PDF card #00-038-1420). According to the calculated data from Table 4-6. The calculated value provides that a higher current condition, 30 A, shows higher nitrogen contents, which corresponds to the TiN crystallinity of the XRD patterns. The nitrogen content could be increased with the increasing current condition of more than 30 A. W. Kim et al., mentioned that in the fine particle, lattice parameter was affected sensitively by the other impurities such as oxygen. This was hard to manage [91].

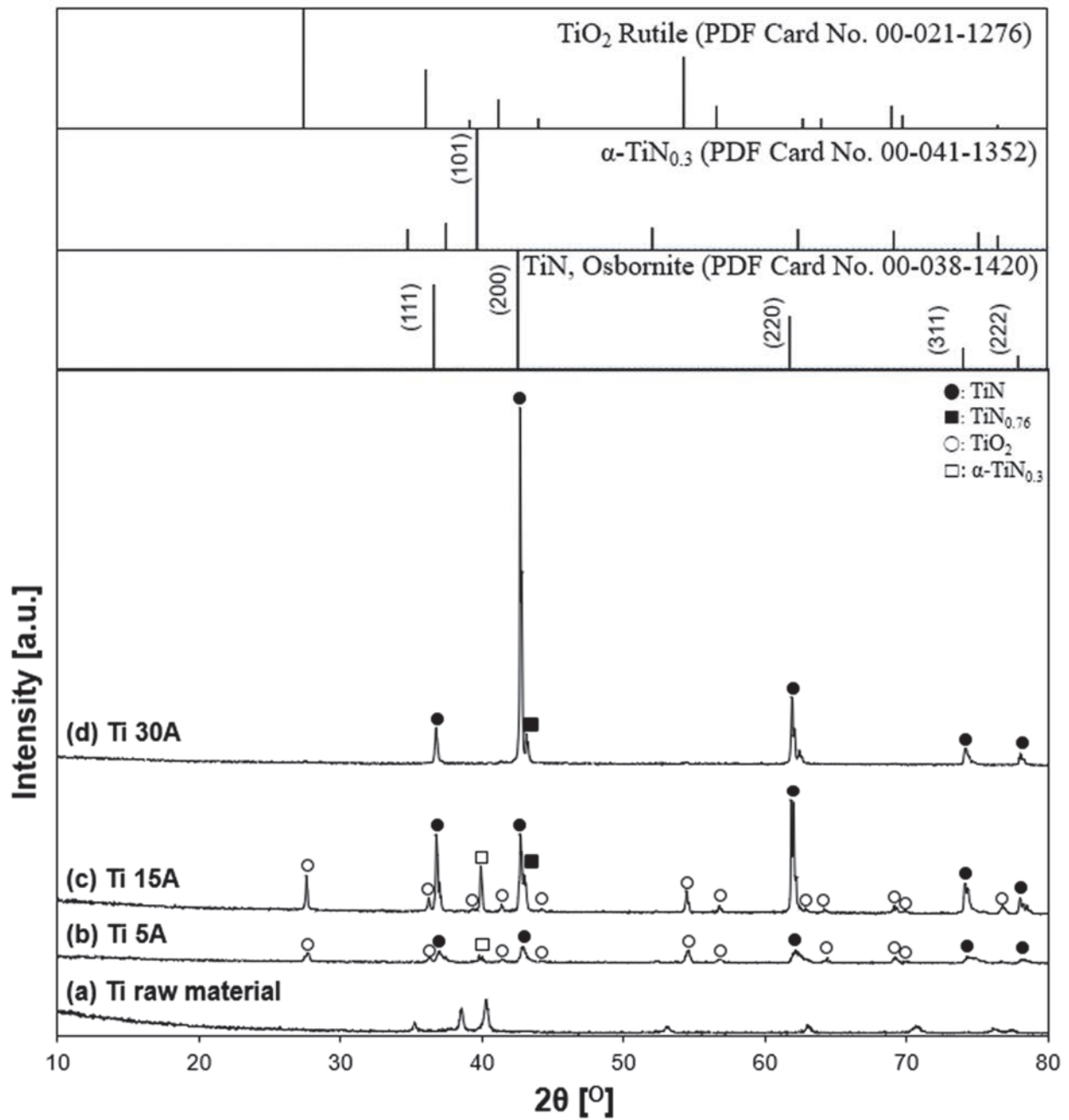


Figure 4-10. X-ray diffraction patterns of prepared samples. (a) Ti raw material, (b) Ti 5A, (c) Ti 15A, (d) Ti 30A, (●) TiN, (■)  $\text{TiN}_{0.76}$ , (○)  $\text{TiO}_2$ , (□)  $\alpha\text{-TiN}_{0.3}$

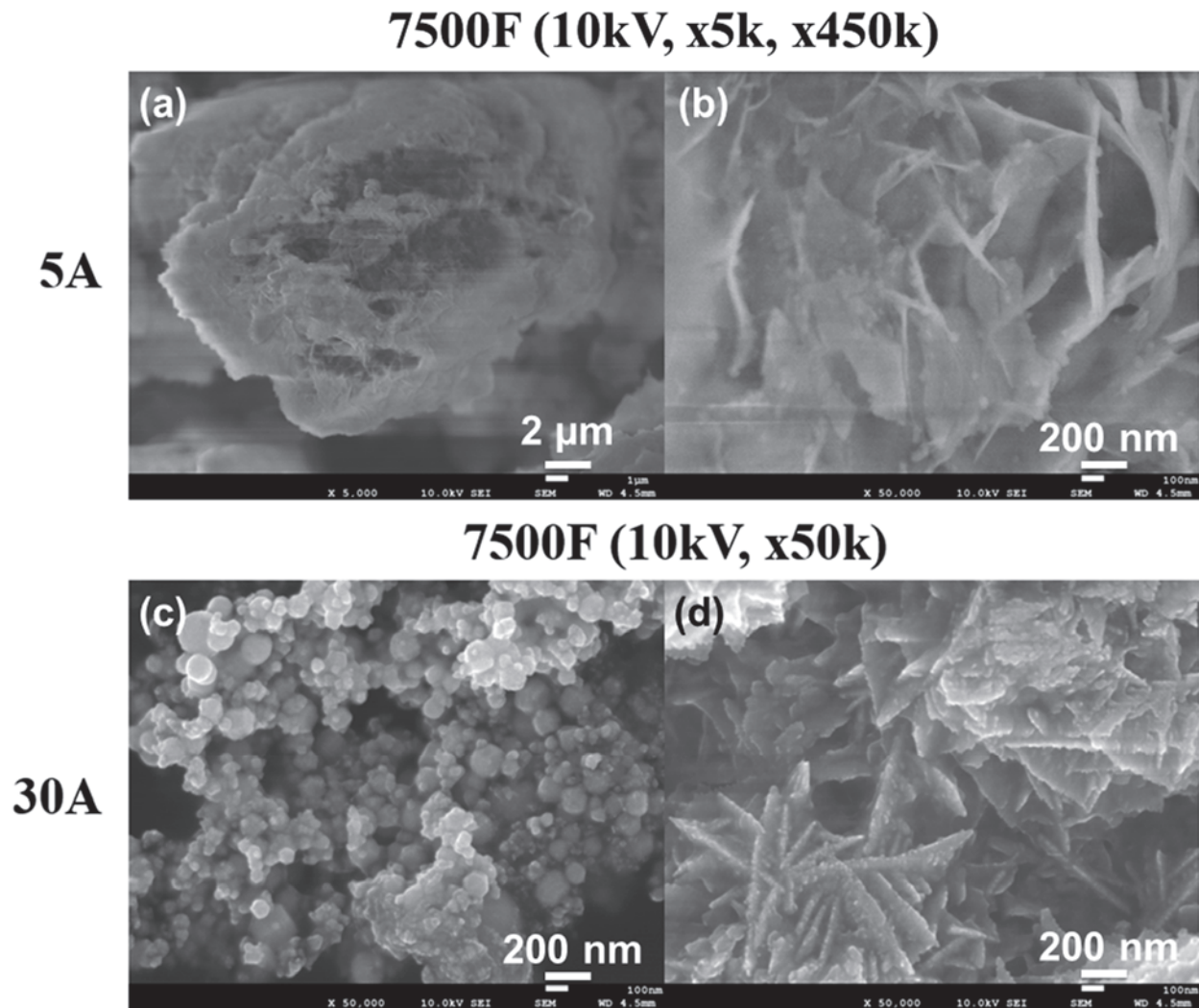
**Table 4-6.** Lattice parameter and nitrogen content of TiN samples

Sample name	Lattice parameter [ $\text{\AA}$ ]	Calculated nitrogen content [at.%]
Ti 5A	4.2201	37.2
Ti 15A	4.2288	42.6
Ti 30A	4.2334	45.3

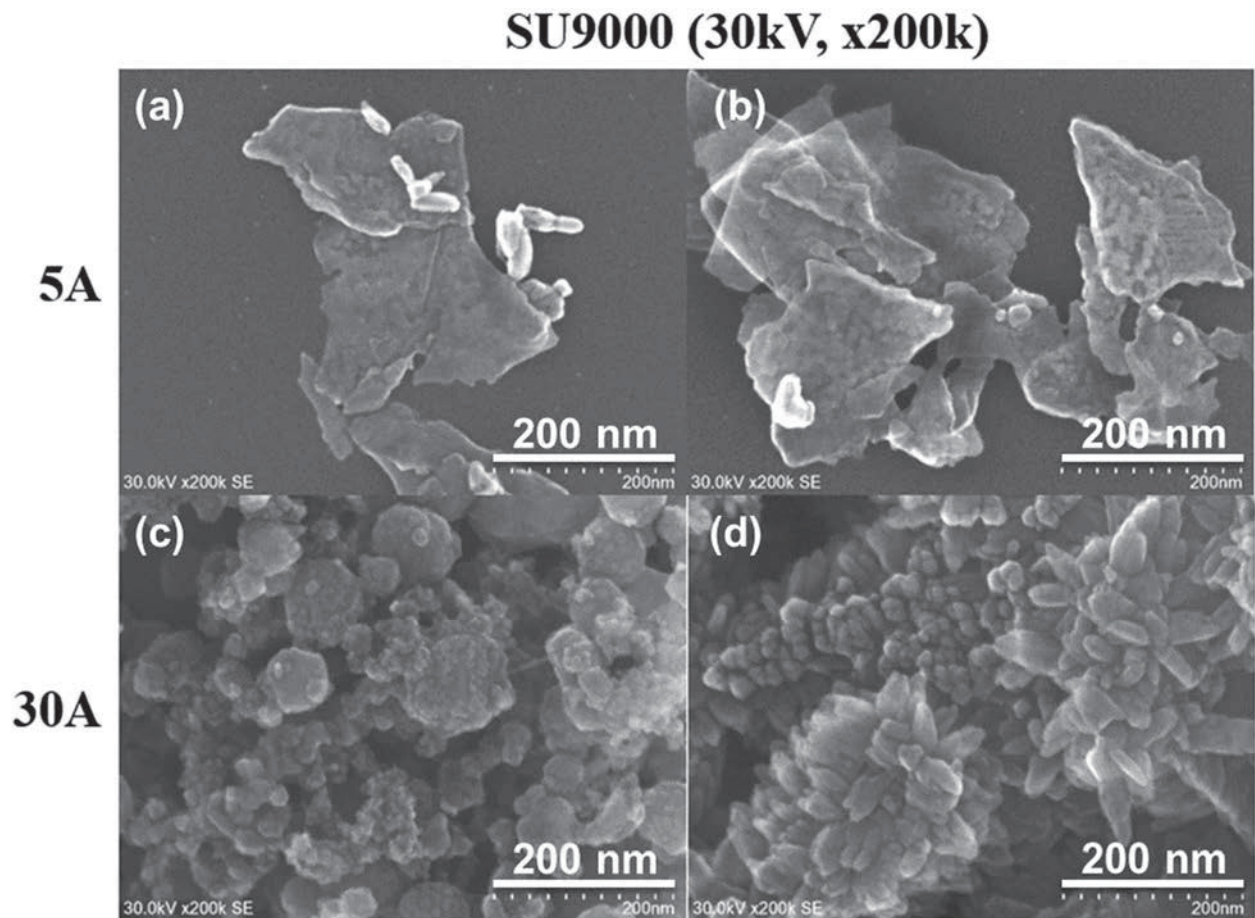
### 4.3.3 Synthesis of Zn/ZnO/Zn<sub>3</sub>N<sub>2</sub> particles

#### 4.3.3.1 Morphologies of the prepared Zn-based nanoparticles

Figure 4-11, 4-12 shows the FE-SEM images of the synthesized particles from the Zn electrodes. By FE-SEM observation using 7500F, the nanosheets with 2~5 nm thickness were observed in low current mode. In the case of the high current mode, spherical particles and aggregated nanosheets were identified. When performed in SU9000 instruments, dispersed sheets and some of the pieces from the nano-rod were observed. In the 30 A condition, spherical particles and grown nano-rods attached to the surface of the sphere particles were observed. We found that sheet-shaped was generally observed in hydrate form [97, 98], while rod-shaped was observed as an oxide form of the zinc [99, 100]. The results of XRD described later in Figure 4-13 indicate the existence of the zinc nitride species. Considering the zinc properties that are easily oxidized and especially in the nanoscale particles.



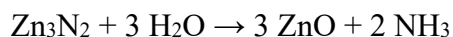
**Figure 4-11.** FE-SEM images of prepared Zn-based nanoparticles. (a, b) the low current mode, Zn 5 A, and (c, d) high current mode, Zn 30 A



**Figure 4-12.** FE-SEM images of prepared Zn-based nanoparticles. (a, b) the low current mode, Zn 5 A, and (c, d) high current mode, Zn 30 A

### 4.3.3.2 Crystallite phase of the synthesized Zn/ZnO/Zn<sub>3</sub>N<sub>2</sub> particles

Figure 4–13 shows the XRD peaks of the synthesized Zn/ZnO/Zn<sub>3</sub>N<sub>2</sub> particles with variable currents of 5 A, 15 A, and 30 A. The peaks of the Zn<sub>3</sub>N<sub>2</sub> (Zinc nitride, PDF #04–015–6960, 2θ=34.28°, 36.73°, 43.36°, 52.92°, 70.73°, 76.66°) appear in all the samples. Among the zinc nitride peaks, the 2θ=52.92° peak appears only in the 30 A condition. Also, in the 30 A condition, one of the peaks of the zinc nitride at 2θ=36.73° is separated from the overlapping main peak and has a clear shoulder, representing the zinc nitride phase component. The intensity of zinc nitride phase peaks is increased with increasing current. On the other hand, the zinc oxide phase is decreased relatively. In the zinc case, it is generally known that zinc nitride is hard to maintain in the nitride phase because zinc nitride is reacting violently with water to form ammonia and zinc oxide. [87, 88]



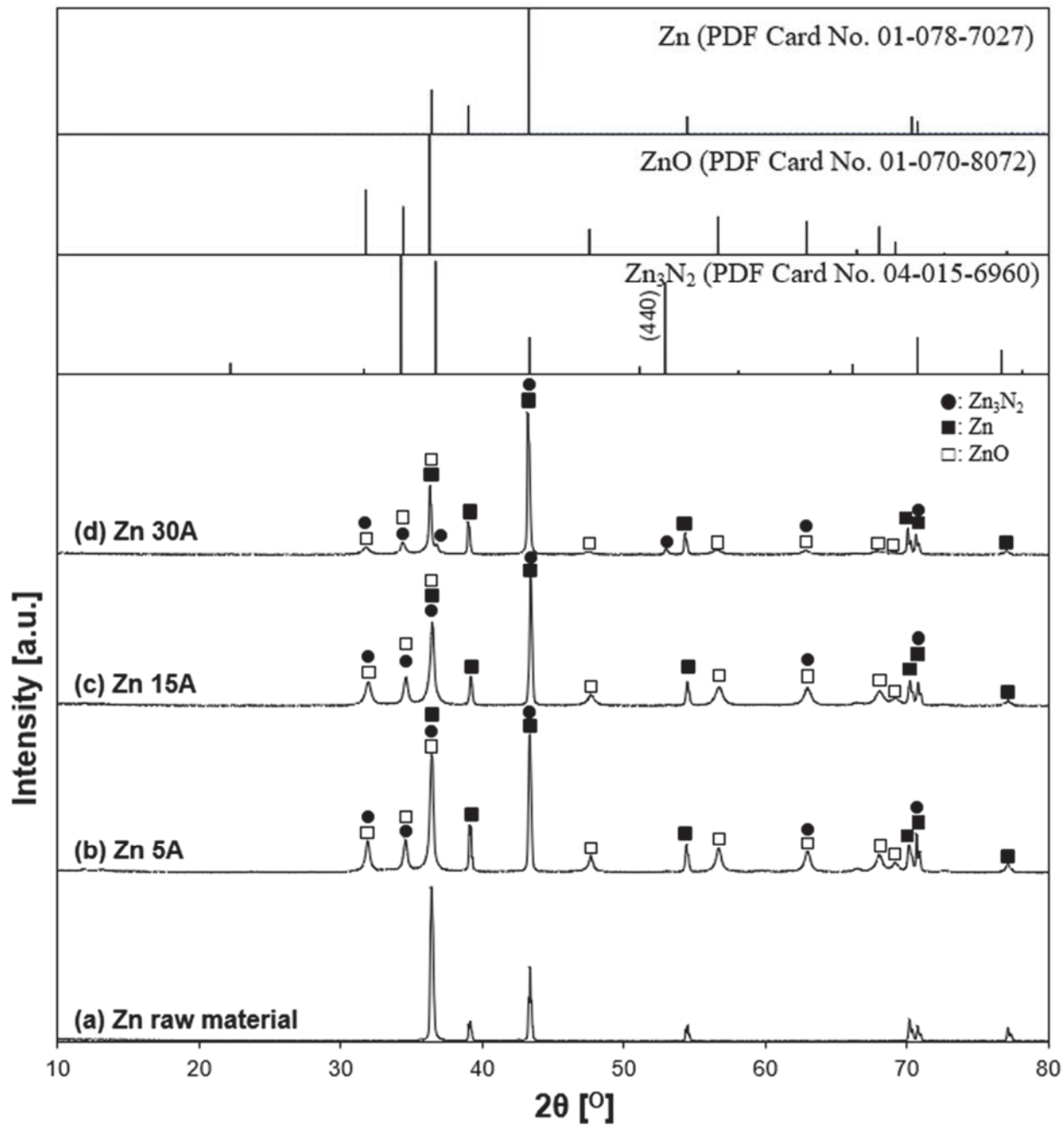


**Figure 4-13.** X-ray diffraction patterns of prepared samples. (a) Zn raw material, (b) Zn 5 A, c) Zn 15 A, (d) Zn 30 A, (●) Zn<sub>3</sub>N<sub>2</sub>, (■) Zn, (□) ZnO



### 4.3.4 Particle preparation using different electrode combinations

The experimental setup is the same as in Chapter 3.2.3. Ti and Cu electrodes are used here. The Ti–Cu experiment refers to Ti as the anode and Cu electrode as the cathode, while the Cu–Ti experiments indicated the opposite combination. The experiments were carried out at an applied current of 30 A.

#### 4.3.4.1 Morphologies of the prepared particles

Figure 4–14 is FE–SEM images of Ti–Cu particles from nano–size to micro–size, which are directly collected from the reactor vessel without dispersing in ethanol. In both nano– and micro–scale, the TiN cubic particle is observed, which indicates the particle is mainly formed from the Ti anode. Most of the cubic particles are observed in aggregated form. In the micro–scale image, few spherical Cu particles are observed, which implies the cathode was melted in the discharge process. In the figure, TiN cubic nano–size particles are attached to the outer surface of the micro–size Cu spherical particle. It is confirmed that it did not affect the internal structure from the particle generation step, corresponding to the XRD results described below. The attached particles are not dispersed homogeneously, just randomly aggregated in the outer surface of the Cu particle. It was confirmed that no trace of the Cu spherical particle and TiN cubic particle reacted with each other, implying that particle formation proceeded independently.

In the case of Cu–Ti configuration, micro–size Cu anode spherical particle was mainly produced. In the nano–scale, either Cu spherical particle and Ti cubic particle were observed. However, there was no micro–size Ti cubic particle in the Cu–Ti experiment.



#### 4.3.4.2 Crystallite phase of the synthesized particles

The XRD patterns of prepared particles, the initial state of Ti anode surface, and the reference patterns of TiN, TiO<sub>2</sub>, and  $\alpha$ -TiN<sub>0.3</sub> are shown in Figure 4–15. The Ti-related peaks are identified at the anode, such as the major peaks of TiN and  $\alpha$ -TiN<sub>0.3</sub> and the minor peaks of TiO<sub>2</sub> whereas the Cu cathode-related peaks are not detected. The XRD patterns indicate that all Ti peaks turned into TiN and an intermediate solid of  $\alpha$ -TiN<sub>0.3</sub>. The high intensity of the TiN peak at 42.7° indicates preferential crystal growth on (200) orientation.

The XRD pattern tendency shows close to the Ti-Ti electrode 15 A and 30 A conditions in Figure 4–10. The calculated lattice parameter is 4.2329 Å, indicating 45 % of nitrogen contents by putting the calculated lattice parameter into Eq (4–3). The value is 1 % lower than in the previous Ti-Ti experiment. In terms of experimental experience, the discharge stability is closely related to the continuous arc discharge, which is one of the factors for particle preparation in this process that affects impurity, reproducibility, and particle production rate. When Cu was used as a cathode, the discharge was relatively unstable compare to the Ti electrode. Comparing the melting points of Cu and Ti, Cu has a lower melting point temperature (1,084 °C) than Ti (1,660 °C). These physical properties of the two materials suggest that when discharge occurs, the Cu cathode melted down more quickly. Compared with the Ti-Ti case, the Ti-Cu anode may not be heated as much as the Ti-Ti anode because the Cu electrode will start to meltdown before heated as Ti-Ti. For this reason, Ti-Cu seems to have a relatively unsustainable discharge behavior compared to the Ti-Ti case. These results may explain the higher XRD intensity of  $\alpha$ -TiN<sub>0.3</sub> intermediates and the lower nitrogen content of the Ti-Cu experiment particles. Figure 4–16 is a melted Cu electrode after the discharge. The tip of the Cu cathode is melted and changed to a rounded shape.

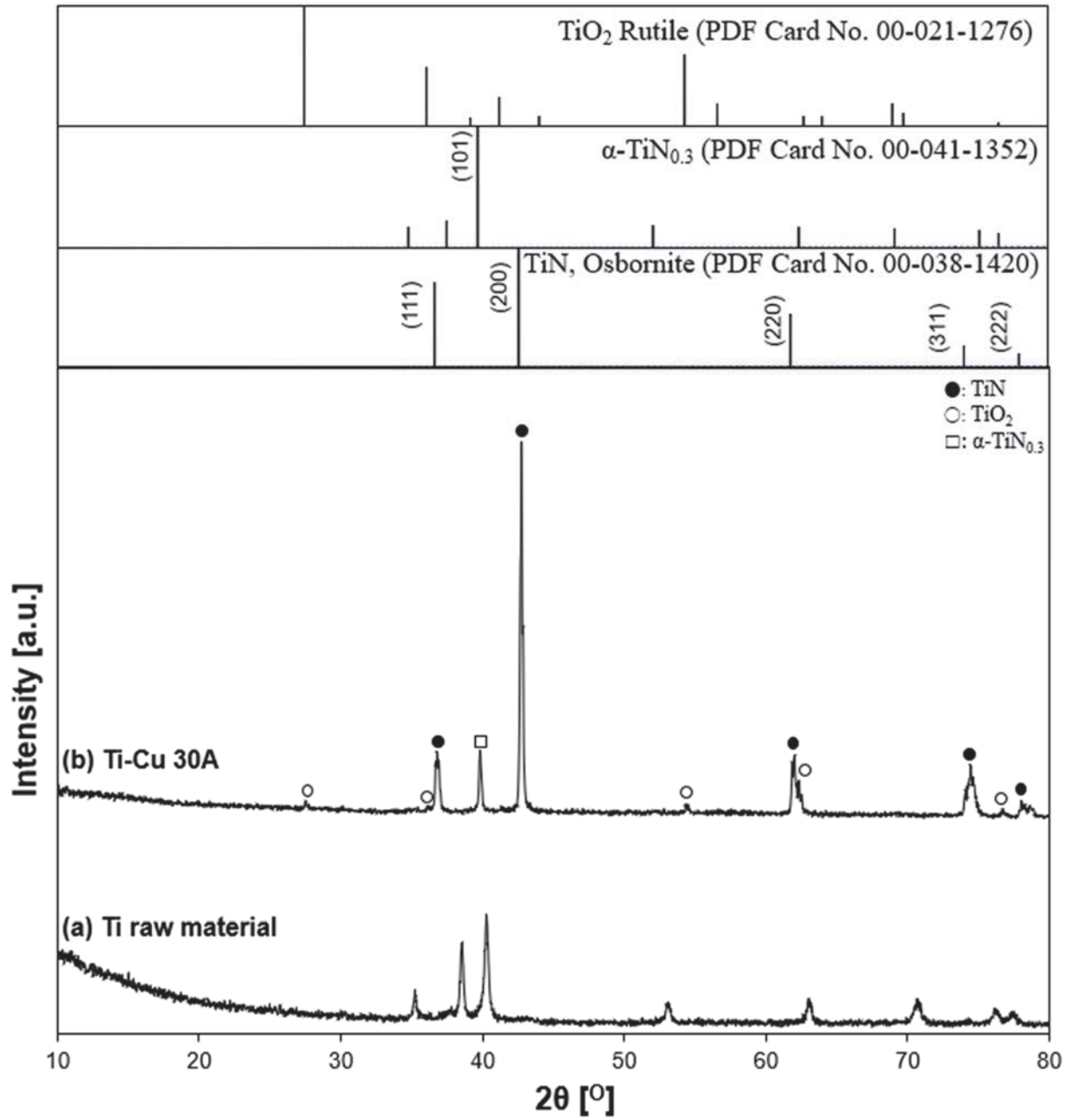


**Figure 4-15.** X-ray diffraction patterns of the Ti-Cu sample. (a) Ti electrode raw material, (b) Ti-Cu 30 A, (●) TiN, (○) TiO<sub>2</sub>, (□)  $\alpha$ -TiN<sub>0.3</sub>

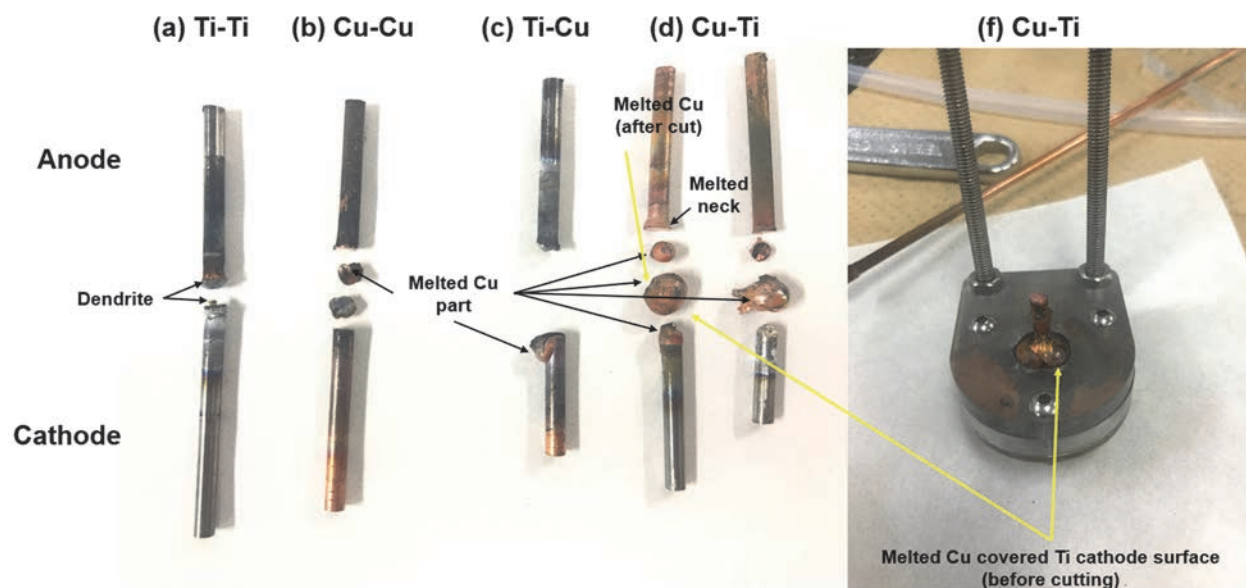


**Figure 4-16.** Melted copper electrode after the 30A reaction (a) Ti-Ti, (b) Cu-Cu, (c) Ti-Cu, (d) Cu-Ti, and (f) Cu-Ti before cutting the melting part

The particle preparation was conducted with a Cu-Ti electrode arrangement. The XRD patterns of prepared particles, the initial state of the Cu anode surface, and the reference patterns of Cu are shown in Figure 4-17. According to the XRD results, Cu is the only component of the prepared particle that was formed. There are no peaks related to the metal alloys.

It is confirmed that the two different electrode materials did not involve each other in the particle generation process. It indicates that the early step of the nucleus did not participate in the chemical reaction with another metal nucleus or metal particle during the discharge. Both results (Ti-Cu and Cu-Ti) show that the particles are synthesized independently ( $\text{Ti} \rightarrow \text{TiN}$ ,  $\text{Cu} \rightarrow \text{Cu}$ ). From the XRD results, the prepared particles are mainly produced from the anode material in this process. In the particle preparation process, each electrode has an independent role. The cathode supplies thermal electrons to the anode, and the heated anode generates ions, which eventually lead to producing the particle. When the Ti electrode is placed on the anode, Ti reacts with ionized nitrogen and produces TiN, while Cu did not react with ionized nitrogen.

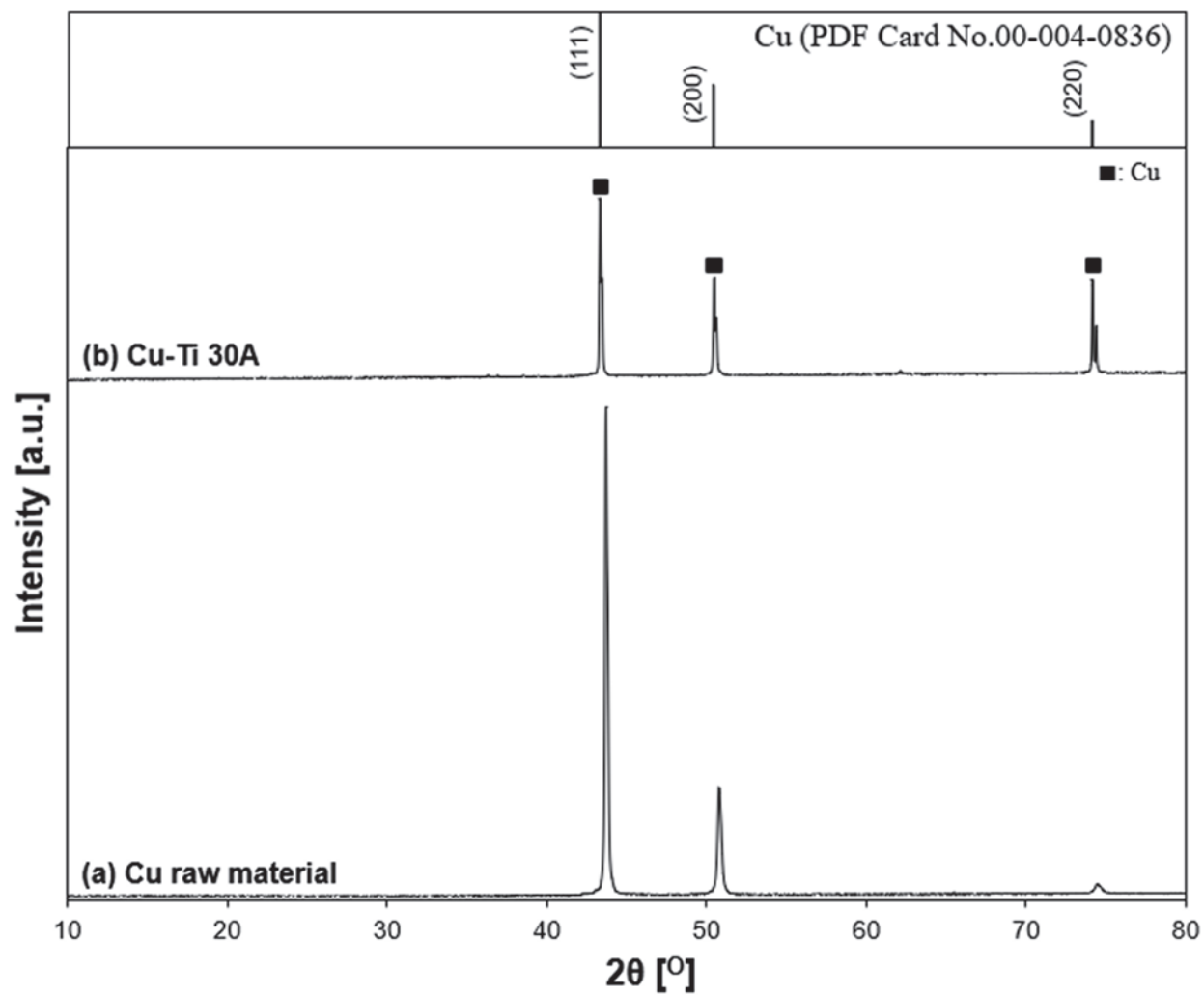


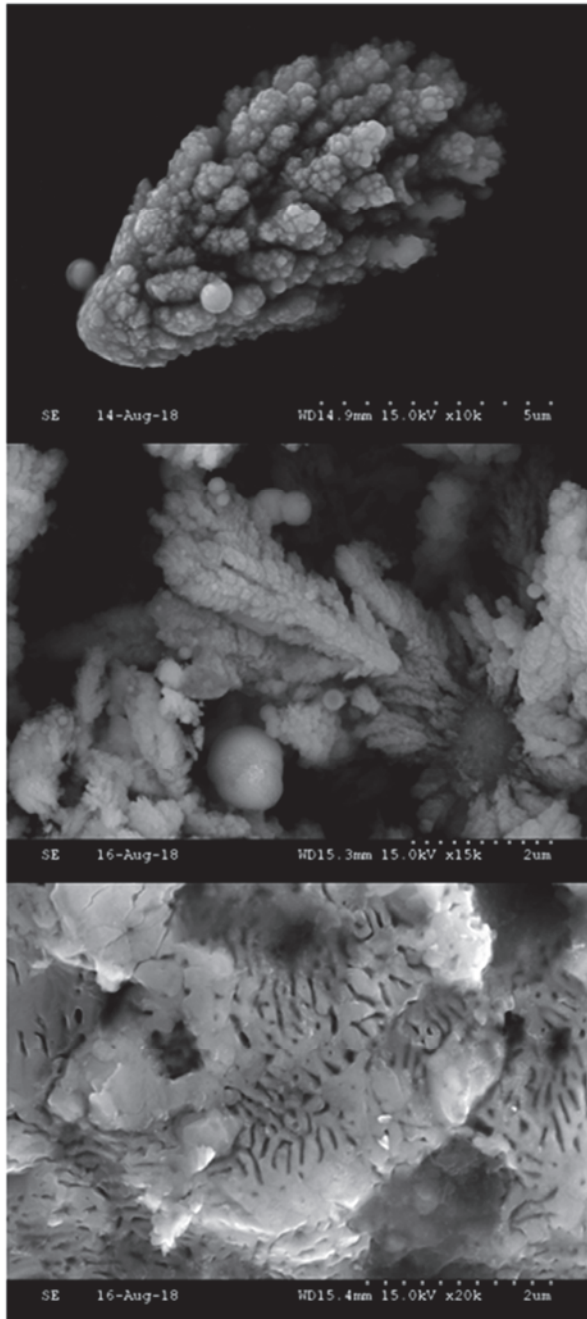
**Figure 4–17.** X–ray diffraction patterns of the Cu–Ti sample. (a) Cu electrode raw material, (b) Cu–Ti 30 A, (■) Cu

#### 4.3.4.3 Generation ratio of the produced particle

According to the XRD results and the FE-SEM observation, it is confirmed that the particle is mainly produced from the anode. In the arc discharge process, the thermion came out from the cathode and collided with the anode surface. Then from the heated anode surface, the molten droplet and the metal vapor are produced. In this study, the molten droplet is collected as a coarse particle in size range around the micro-scale, and the vapor is finally collected as a fine particle with a nano-size scale. The produced debris, droplets, and vapors are rapidly quenched by the surrounding liquid nitrogen. Since the surrounding temperature is low and in a relatively pressurized atmosphere with liquid nitrogen, a lot of quenched particles were deposited on the electrode surface. In some parts, deposited particles form a dendrite structure, which is one of the growth patterns of molten metal in the undercooling process. Figure 4-18 shows the images of the dendrite structure on the electrode surface after arc discharge. Figure 4-19 is an illustration of the arc discharge behavior considering the arc generation mechanism.



**(a) Cu**



**(b) Ti**

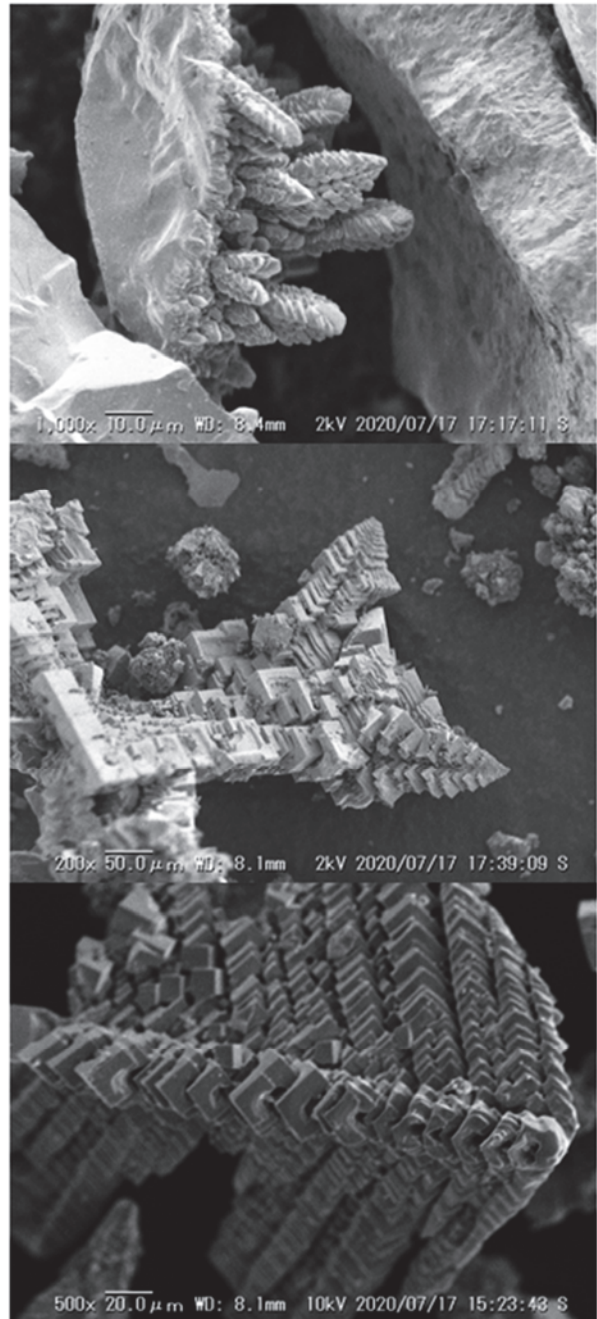


**Figure 4–18.** Dendrite structure of the coarse particle and debris.



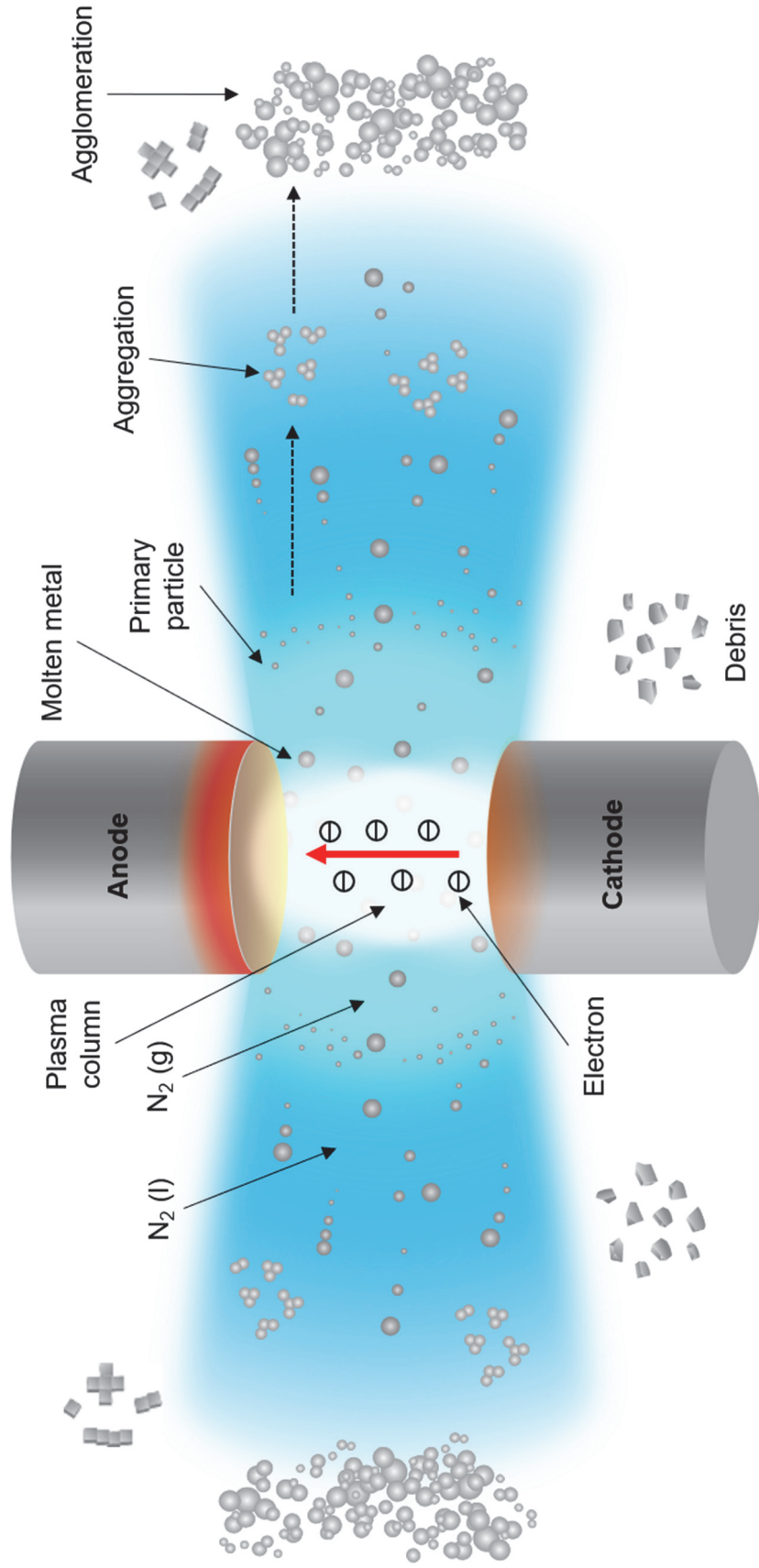


Figure 4–19. Illustration of the arc discharge mechanism in this reaction

#### Chapter 4. Variation in metal electrodes for the particle preparation using liquid nitrogen discharge

The particle generation ratio of the product was calculated using an electrical scale that measures up to four decimal digits. The yield was calculated by comparing the initial electrode weight before and after the discharge and the weights of debris and coarse particles produced. The following equation is the yield in this study. The  $w$  is a measured weight of sample. For example,  $w_{coarse\ particle}$  is a measured weight of produced coarse particle.  $w_{anode\ initial}$  is a measured weight of the initial state of the anode, and  $w_{cathode\ discharge}$  is a measured weight of cathode after discharge procedure is done.

$$\text{yield [\%]} = \left( \frac{w_{coarse\ particle} + w_{debris}}{w_{anode\ initial} - w_{anode\ discharge} + w_{cathode\ initial} - w_{cathode\ discharge}} \right) \times 100 \quad (4-1)$$

Yield includes debris, while the particle generation ratio only considers produced coarse particles. The weight of the fine particles is excluded in this calculation. In addition, the particles that were blown away from the drastic vaporization of the liquid nitrogen and arc shockwave, and those remained fine particles in the vessel and cell were considered as a loss.

**Table 4–7.** Particle generation ratio and loss of the particle formation process

electrode configuration (+)-(–)	yield [%]	particle generation ratio [%]	loss [%]
Ti–Cu	54	21	46
Cu–Ti	87	43	13

In Table 4–7, the loss rate of the Ti–Cu particle is much higher than Cu–Ti. One reason is that Ti–Cu discharge mainly produced fine Ti particles while Cu–Ti discharge mainly produced relatively larger micro–sized Cu particles. Due to the heat from the discharge inside the liquid nitrogen, many bubbles were drastically generated in a short time. It is believed that a large

#### Chapter 4. Variation in metal electrodes for the particle preparation using liquid nitrogen discharge

number of fine particles were lost together with the evaporation of nitrogen. In our experimental conditions, the particle preparation of Cu seems to mainly depend on the melting process, which forms micro-sized particles rather than the vaporization process producing nano-sized particles. Compared to other Al, Ti, and Zn particles, micro-size particles are mainly produced using Cu electrodes.

The production of the particle depends mainly on the physical properties of the materials, such as melting points and boiling points, and also on the continuity of the discharge which can be related to the treatment time in this process. The produced amount of the particle in this study was in the order of  $Zn > Al > Ti \gg Cu$ . In the Cu electrode case, although it has a lower melting point and a boiling point than Ti, Cu generates fewer particles than Ti. We tried to find out the reason from the Cu material properties. According to Table 2-2 and Table 4-2, the Cu material has around 18 times higher thermal conductivity compared to Ti (Cu: 401 W/(m·K), Ti: 21.9 W/(m·K)). However, the molar heat capacity of the four materials is similar to each other (Cu: 24.4 J/(mol·K), Ti: 25.06, Al: 24.2, Zn: 25.47). Since the particle formation in this process uses a liquid nitrogen medium, the heat generated from the electrode surface is relatively difficult to maintain the temperature. As the anode surface temperature, in the view of the production of the particle, might be insufficient to reach to vaporize the metal than melting. And as the cathode surface temperature, in the view of the electron supplier, might be insufficient to emitting the electron stably. A detailed explanation of the cathode and continuous discharge will be described in Chapter 5. It might be one reason why the Cu electrode shows a relatively unsustainable discharge compared to Ti electrodes. It is closely related to continuous discharge and the particle preparation process.

In the case of an Al and Zn electrode with a lower melting point and boiling point, the production ratio of the particle by discharge time appears bigger than Ti and Cu electrodes. Even with a short time of discharge, the electrode is heated and begins to meltdown, producing a lot of debris, coarse particles, and fine particles.

## 4.4 Summary

Prior to summing up this chapter, the findings related to the characterization results of the prepared particle are summarized in Table 4–8.

**Table 4–8.** Summary of characteristic observation on the prepared particle in this study

	Cu	Al	Ti	Zn
Nitride	×	○	○	○
Oxide	△	×	△	○
Nitride peaks intensity in XRD (5 A → 30 A)	n/a	↑	↑	↑
Oxide peaks intensity in XRD (5 A → 30 A)	↓	↓	↓	↓
Particle generation ratio (5 A → 30 A)	4th	2nd	3rd	1st
Particle shape (5 A → 30 A)	sphere	sphere	5 A: mainly sphere 30 A: cubic	nano–sheet, rod sphere
Particle size (5 A → 30 A)	↓	↑	↑	n/a

A liquid nitrogen discharge experiment was conducted to synthesize the particles utilizing DC power at two operating conditions: lower current mode (5 A) and the high current

#### Chapter 4. Variation in metal electrodes for the particle preparation using liquid nitrogen discharge

mode (30 A), which enabled generate arc discharge. Three kinds of electrodes, Al, Ti, and Zn, were examined in this chapter. Through the discharge experiments, micro- to nano-size particles were successfully obtained from each of the electrodes, respectively. According to the XRD analysis results, it was confirmed that the crystallinity of the product crystal phase and the phase component changed as the current varied. This implied that the experiment variable as a current influenced the crystallinity of the synthesized products. From the XRD patterns, nitride phases were confirmed in all the conditions using Al, Ti, and Zn electrodes. The FE-SEM image showed that the majority of the product particles were aggregated to each other.

Ti electrodes experiment showed a clear difference in the shape of the product particle as the applied current changed. In the low current mode, which showed low crystallinity in XRD patterns, the particles are spherical with an average size of 30.04 nm. On the other hand, in the high current mode, a clear cubic TiN particle with an average size of 43.16 nm was identified. The nitrogen content was enhanced 22% by increasing the current condition, low mode 5 A into high mode 30 A, which corresponds to the initial value 37.2 at.% into final 45.3 at.%.

In Al electrodes, a large number of spherical particles, having an average size of 25.77 nm in low current mode and an average 46.31 nm size in high current mode, were observed. It is hard to distinguish Al and AlN by the particle shape of the image. XRD results confirmed that AlN was produced in a liquid nitrogen discharge experiment.

The thin sheets having 2~5 nm thickness, were produced in the Zn electrode experiment. In the high current case, nano-rods were observed grown on the spherical particle surface. From the XRD analysis, the presence of zinc oxide and zinc nitride was confirmed. Not only nitrides but also oxides were produced in Ti and Zn experiments. This is because of the sampling procedure, and the metal samples were easily oxidized when exposed to the air. The special care is required to maintain the nitride formed in the sampling procedure until analyzing the sample. It seems to be challenging to maintain the nitride form in normal conditions.

According to the experimental results of different metal electrode combinations, it was confirmed that anode generates most of the particles in this process. The XRD results showed that the metal alloy was not observed, while the Ti electrode produces TiN particle and the Cu electrode produced Cu particle. Based on the phenomena, it is determined that each of the

#### Chapter 4. Variation in metal electrodes for the particle preparation using liquid nitrogen discharge

electrodes performed an independent role without interfering with other electrodes in the particle generation.

The yield of the Ti–Cu and Cu–Ti experiments was measured. Ti–Cu shows 54 % while Cu–Ti shows 87 %. The generation ratio of the coarse particle was measured. Ti–Cu shows 21 %, while Cu–Ti shows 43 %. A big portion of the loss was found from the calculation. Ti produces a number of nano–sized particles, and it seems to be a quite large portion of the produced particles are blown away when liquid nitrogen drastically vaporizing. In the Cu case, a large portion of particles was recovered. It is plausible that Cu mainly produces micro–sized particles, so it might be hard to blow away like Ti nanoparticles.

Production of the particle is closely related to the boiling point and melting point of the electrode materials. The produced amount of the particle in this study was in the order of  $Zn > Al > Ti \gg Cu$ . In the case of an Al and Zn, even with a short time of discharge, the electrode produces many particles. Although Cu has a lower melting point and a boiling point than Ti, Cu generates fewer particles than Ti. The unstable arc discharge is suggested as one reason.

# CHAPTER 5

## Mechanism of particle formation

## 5.1 Introduction

In previous chapters, particles were synthesized from Al, Cu, Ti, and Zn electrodes using arc discharge in liquid nitrogen. The morphologies of the synthesized particles were investigated by FE-SEM. The XRD analyses were performed for the characterization of the particles. According to the experimental results of different metal configurations, we found that most of the particles are produced from the anode. While the cathode role as an electron supplier when discharge occurs. The illustration of the arc mechanism in this process was provided in Chapter 4. Based on the phenomena, it is concluded that anode and cathode performed an independent role without interfering with each other during the discharge for particle generation.

In this chapter, a thermodynamic calculation is carried out to explain the formation of the nitride particles. Moreover, we investigated the anode and cathode focused on their role in the arc discharge in liquid nitrogen for particle preparation. First, an electron supplier as a cathode for sustaining the arc discharge is discussed based on the relationship between the physicochemical properties of the cathode materials and the arc discharge behavior in liquid nitrogen. Second, the surface morphology of the anodes was investigated by SEM. The particle formation mechanism is proposed based on the morphologies of the anode surface and synthesized particles.

## 5.2 Thermodynamic approach to the nitridation

### 5.2.1 Analysis

Previously, Al, Cu, Ti, and Zn electrode are used for particle preparation in liquid nitrogen discharge experiments. The crystalline phase of the product is summarized in Table 5-1.

**Table 5-1.** The crystalline phase of the synthesized particle



Metal electrode	Product
Al	Al/AlN
Cu	Cu
Ti	TiN
Zn	Zn/ZnO/Zn <sub>3</sub> N <sub>2</sub>

In order to explain the formation of the nitride particles, the thermodynamic approach is introduced. The Gibbs standard free energy of the electrode material and the synthesized metal nitrides are calculated using the chemical thermodynamics computing program (FactSage version 5.1, Thermfact/CRCT, Montreal, Canada and GTT-Technologies, Aachen, Germany). The equilibrium constant ( $K_{eq}$ ) is calculated using the software with the stoichiometry and temperature profile of the reaction. The calculated  $K_{eq}$  was put into Eq (5-1), which was the equation for calculating Gibbs standard free energy.  $R$  is a gas constant of 8.31451 [kJ/mol·K], and the temperature in the range of 77 K to 4000 K was investigated.

$$\Delta G^0 = -RT \ln K_{eq} \quad (5-1)$$

### 5.2.2 Gibbs standard free energy calculation

Figure 5-1 shows the Gibbs standard free energy ( $\Delta G^0$ ) change as a function of temperature for synthesizing AlN, TiN, and Zn<sub>3</sub>N<sub>2</sub> from the electrode material. Cu is excluded from the figure because there was no database of nitrides. The marked circle is the melting point of the electrode materials, and a blank circle is the boiling point of the electrodes. The three kinds of nitridation reactions in Figure 5-1 spontaneously occur when the state of the  $\Delta G^0$  is negative ( $\Delta G^0 < 0$ ). According to Figure 5-1, the nitridation of Al and Ti materials shows the negative  $\Delta G^0$  until around their boiling point temperature, respectively. This indicates that Al and Ti are reacting with nitrogen and synthesize nitrides. In the case of Zn, Gibbs standard free energy shows negative only

within the narrow range from 77 K to 122 K. In this study, it might be possible that zinc nitride was synthesized under the liquid nitrogen temperature (77K).

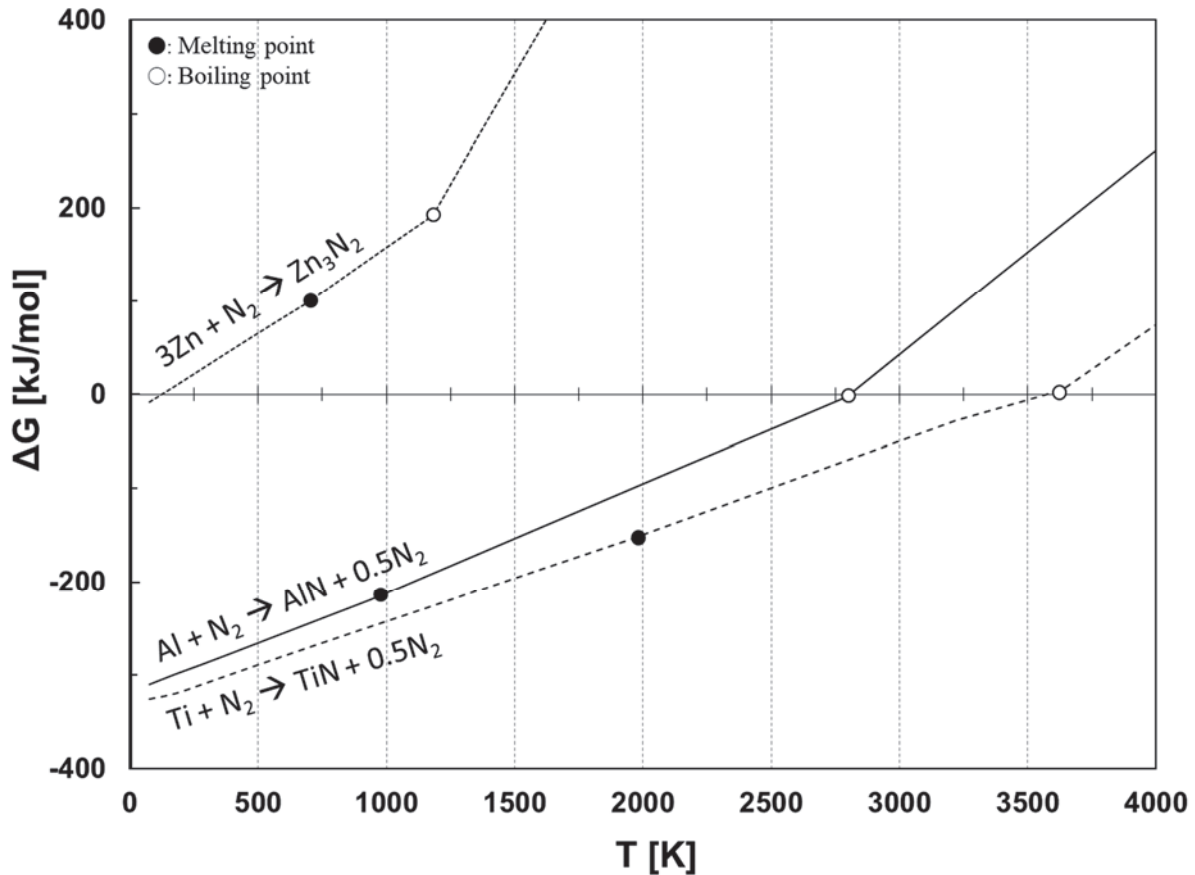


Figure 5–1. Gibbs standard free energy for synthesizing nitrides from Al, Ti, and Zn electrodes

### 5.3 Sustainable arc discharge for stable particle preparation process

In this section, we discussed the electron emission role of the cathode for sustaining the arc discharge. The cathode has no direct relation to particle formation since the particles mainly come from the anode. However, it could be possible to improve the continuity of the particle preparation

process. Furthermore, it gives a better understanding of the interaction between the electrode and the arc discharge behavior.

Ti has a high melting point and boiling point, so as an aspect of continuous discharge, Ti enables to maintain a stable discharge longer time which leads to the high production rate of the particle than Al, Cu, and Zn electrode.

Cu shows a similar trend to Ti, which has a relatively high melting, boiling point, and maintains successive discharge longer than Al and Zn electrodes. However, the production amount of the particle is lower than Al, Ti, and Zn. This reason was mentioned in the previous chapter 4.3.4.3.

As an important factor for sustainable arc discharge, the cathode has to provide a proper number of thermal electrons, and it should have a high melting point and boiling point to endure the heat. Based on the experimental data, the stability for the successive discharge was in the order of  $Ti \gg Cu > Al > Zn$ .

Ushio et al. investigated the correlation between arc discharge stability and cathode thermal electron emission [101]. The Eq (5-2) is a Richardson–Dushman equation for the thermal electron emission density at the cathode [102–104]. Where  $T$  [K] is cathode temperature,  $W$  [eV] is a work function, and  $k_B$  [J/K] is a Boltzmann constant. ( $1 \text{ eV} = 1.60219 \times 10^{-19} \text{ J}$ ).  $J$  [ $\text{A}/\text{m}^2$ ] is the current density at the cathode. The minimum value of the current density required for maintaining arc discharge is  $10^6$  [ $\text{A}/\text{m}^2$ ] reported in many references [57, 101]. The proper current density ( $J$ ) of arc discharge is known to be  $10^6 \sim 10^8 \text{ A}/\text{m}^2$  [101]. In the equation, “ $A$ ” is a thermionic emission coefficient, generally using a value of  $6 \times 10^5$  [ $\text{A}/\text{m}^2 \cdot \text{K}^2$ ]. Accordingly, in Eq (5-2), the value of  $W$  can be calculated when we know  $J$ ,  $A$  values and by putting the temporary temperature. Based on the calculation, the linear dot line can be described in Figure 5-2.

Figure 5-2 shows the functional relationship between temperature and work function of the materials. The linear dot line in the middle is a minimum current density ( $J=10^6 \sim 10^8 \text{ A}/\text{m}^2$ ) for maintaining stable arc discharge. The individual sphere mark indicates thermionic emission at a work function. The color describes the boiling or melting point of the materials. The work function has different values between the plane orientation, so some materials are expressed in the range. The work function values of each material were referred from the various references [105–110].

The upper part region from the dotted line indicates that the stable arc discharge can be maintained. The bottom part from the dotted line indicates that unstable arc discharge generates by the lack of current density. For example, Zn electrodes, the discharge maintains only few seconds since the electrode melting and vaporizes.

$$J = AT^2 \exp\left(-\frac{W}{k_B T}\right) \quad (5-2)$$

In order to emit the thermion, the temperature of the cathode should be maintained at a certain level. At the boiling point of a material, the metal vaporizes and could not supply electrons. Thus, it is concluded that the boiling point of the material could be the upper limit of the temperature. So, in Figure 5-2, the boiling point of the electrode materials and melting point of TiN and AlN are listed. In the case of TiN and AlN, melting temperature is already in the stable region. However, zinc nitride is known to decompose around 700 °C, so it is not described in the figure.

According to Figure 5-2, Al, Cu, and Zn seem to be unsuitable as a cathode for sustaining stable arc discharge. Ti could be a suitable cathode in this study. According to the Figure 5-2, the suitable cathode for sustaining arc discharge can be classified as follows, stable Ti electrode and unstable Cu, Al, and Zn electrode. In the comparison of Cu and Al, both have a similar boiling point. However, the melting point of Al (933 K) is much lower than Cu (1,357 K) and Ti (1,933 K). The meltdown speed of the Al electrode occurs in much earlier step than Cu electrode. When the electrode starts to melt, the maintaining the gap distance was quite hard.

During the arc discharge, the tip of the Ti electrodes turned into golden yellow, which was an appearance color of TiN. Figure 5-3 shows a produced golden yellow color of TiN covered on the tip of the Ti electrode. In the data of Figure 5-2, TiN is also positioned in the stable arc discharge region. TiN requires less work function than Ti, which indicates TiN requires less energy to emitting thermion from the cathode. In other words, TiN can initiate arc discharge at a lower temperature than Ti. It was confirmed that TiN synthesized on the Ti electrode surface provides a more stable arc discharge for the particle preparation process.

A similar discharge behavior was observed in the initial stage of the Al 30 A experiment. The white to pale-yellow AlN particles covered both electrodes were observed. However, as Al has a low melting point (933 K), the heated anode started melting drastically and hindered AlN formation's effect on the cathode tip. When the melting started, the gap distance was hard to manage, causing the arc discharge to be maintained only for a few seconds. In the case of the Al electrode, proper experiment condition is required for the particle preparation process. It can be concluded that the stability of the arc discharge was affected by the work function, cathode temperature, and thermal properties of the electrode materials.

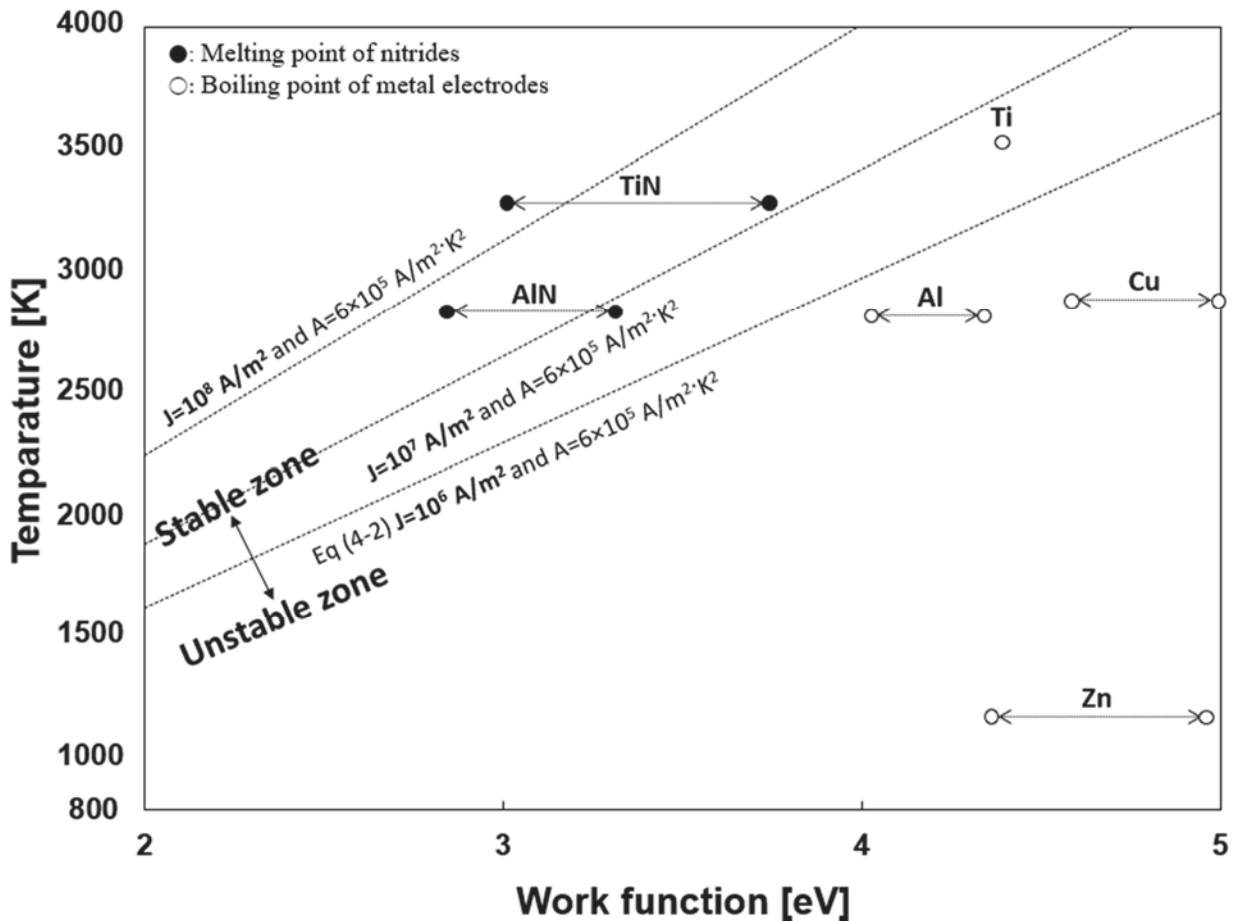


**Figure 5-2.** Linear function of minimum current density for stable arc discharge and the relationship between temperature and work function. Individual sphere mark indicates thermionic emission at a work function, and the color describes the boiling or melting point of the materials.

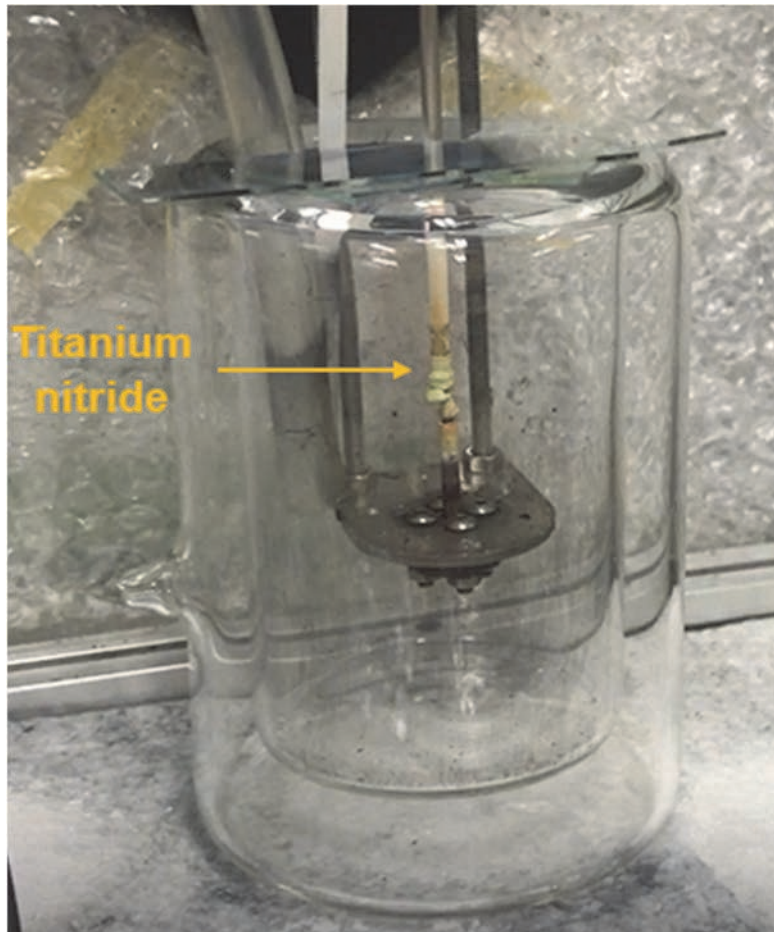


**Figure 5–3.** After the reaction, the titanium electrode was covered with the golden or yellowish color of titanium nitride

## **5.4 Particle formation mechanism**

### **5.4.1 Surface morphologies of Al, Cu, Ti, and Zn anode**

In this section, we discussed the surface structure of the anode, which played a role in generating particles in this process. By comparing the morphology of the anode surface and the morphology of the produced particle, we tried to understand the particle formation process.

Figure 5–4 (a) shows the observation of the Al anode tip surface after the discharge at low magnification. There are many melted regions caused by heat, which is generated from colliding with the thermo–electrons in the plasma channel. Around the melted region, the generating particles are in aggregated form. Figure 5–4 (b) and (c) are the images of the generated particles observed from the electrode surface at high magnification. Inside Figure 5–4 (b) and (c), the spherical particles were adhered to the electrode surface and stacked up in a vertical direction. It seems to be an evaporated Al material from the plasma column, quenched rapidly and condensed on an electrode surface. It was confirmed that the morphology of spherical particles in (b) and (c), which is formed on the electrode surface, corresponding to the produced particle (d) and (e), which is sampled from the micro–sized particle, and (f) and (g) which is sampled from the nano–sized fine particle.

The image arrangement is similar to Figure 5–4, from Figure 5–5 to 5–7 representing the Cu, Ti, Zn electrodes, respectively. The first low (a), (b), and (c) indicates an electrode surface structure. (a) is a low magnification image of the anode tip surface after the discharge. (b) and (c) is a high magnification image of the anode surface structure. Images on the second row start from (d) are produced micro–sized coarse particles, and images on the third row are generated nano–sized fine particles.

In Figure 5–5, copper anode generates spherical particles. Cu did not form nitride. Thus, the particles were obtained directly by the physical impact on the electrode without any nitride reaction involved. The contents are discussed in Chapter 3.

The surface of the Ti 30 A anode tip after the discharge was shown in Figure 5–6 (a) to (c), in Figure 5–6 (b) the generated micro–sized cubic TiN particles were observed next to the melted region in Figure 5–6 (a), suggesting that the partially melted Ti reacted with nitrogen atoms and formed on the electrode surface. The generated micro–cubic particles were found in a dendrite growth structure due to the rapid cooling of gas and liquid. The size and shape of the dendrite structure particles correspond to the size and shape of the coarse particles collected. Consequently, it is thought that the coarse particles were directly derived from the detachment of those micro sizes of cubic dendrites on the electrode during discharge, which was most likely caused by physical force such as an arcing shockwave.

In Figure 5-7 (b) and (c), the observation image on the Zn anode surface indicating that the initial forming particles are in a shape of spherical. However, the morphology of the produced Zn sample is quite different. Only some parts of particles show spherical. As in Figure 5-7 (g) and (h), it was observed that the rod-shaped particles seem to be growing on the spherical particle surface. The crystal growth proceeds in the produced particle surface and forms a cluster. It seems to react with the moisture of the surroundings and transformed into oxide forms.

According to the SEM images of the Al, Cu, Ti, and Zn electrode surface, the unique features of the particles were observed from the anode surface. In the observation, the shape of the structure in the anode surface corresponds to the produced particle in each metal experiment. These findings suggest that the particle formation in this process could be explained by the formation of the anode surface structure shown in Figure 5-4 to Figure 5-7 and the particle formation was mainly caused on the anode.



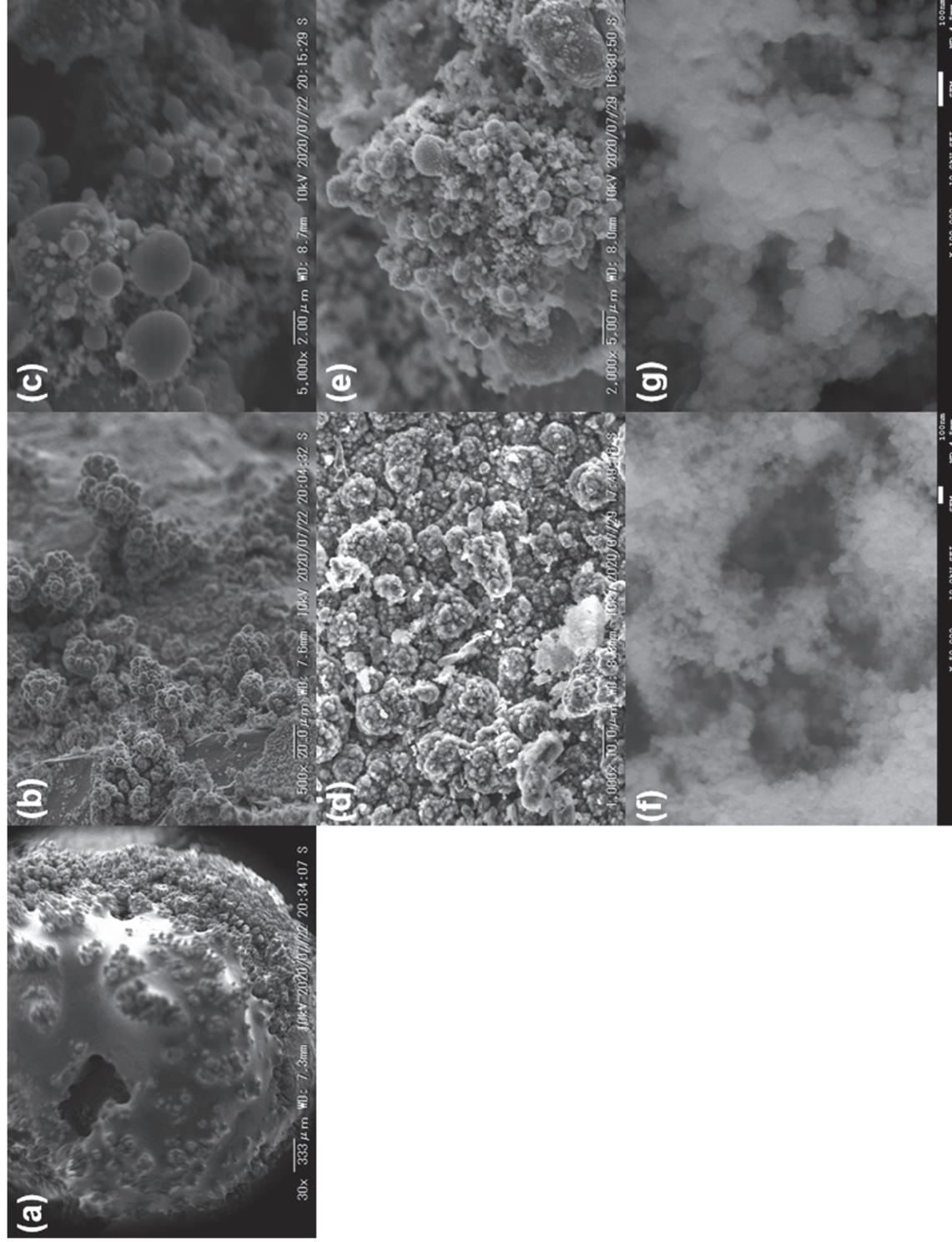
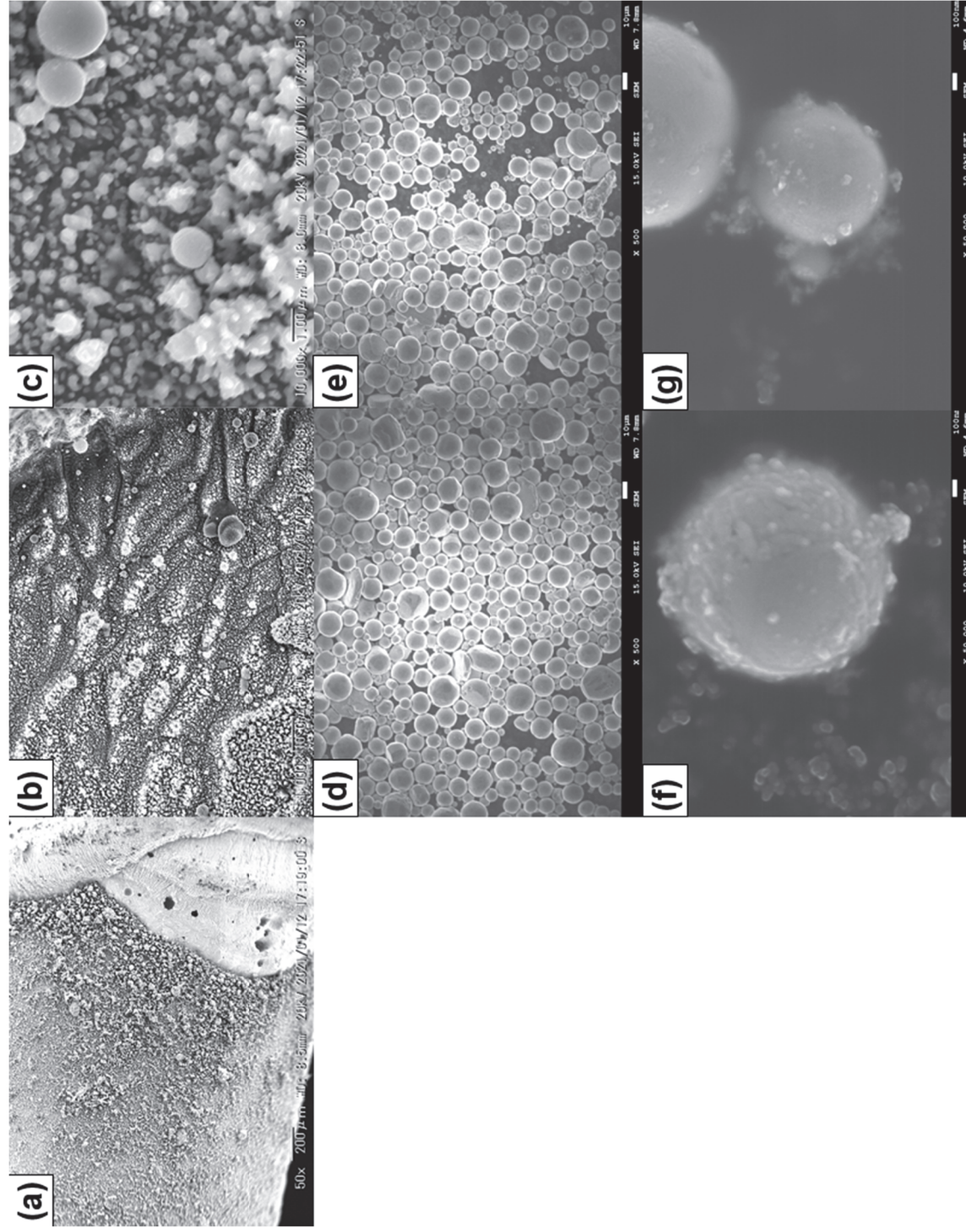


Figure 5-4. Al particle forming on the anode surface (a), (b), (c), Al coarse particle (d), (e), Al fine particle (f), (g).



**Figure 5-5.** Cu particle forming on the anode surface (a), (b), (c), Cu coarse particle (d), (e), and Cu fine particle (f), (g).



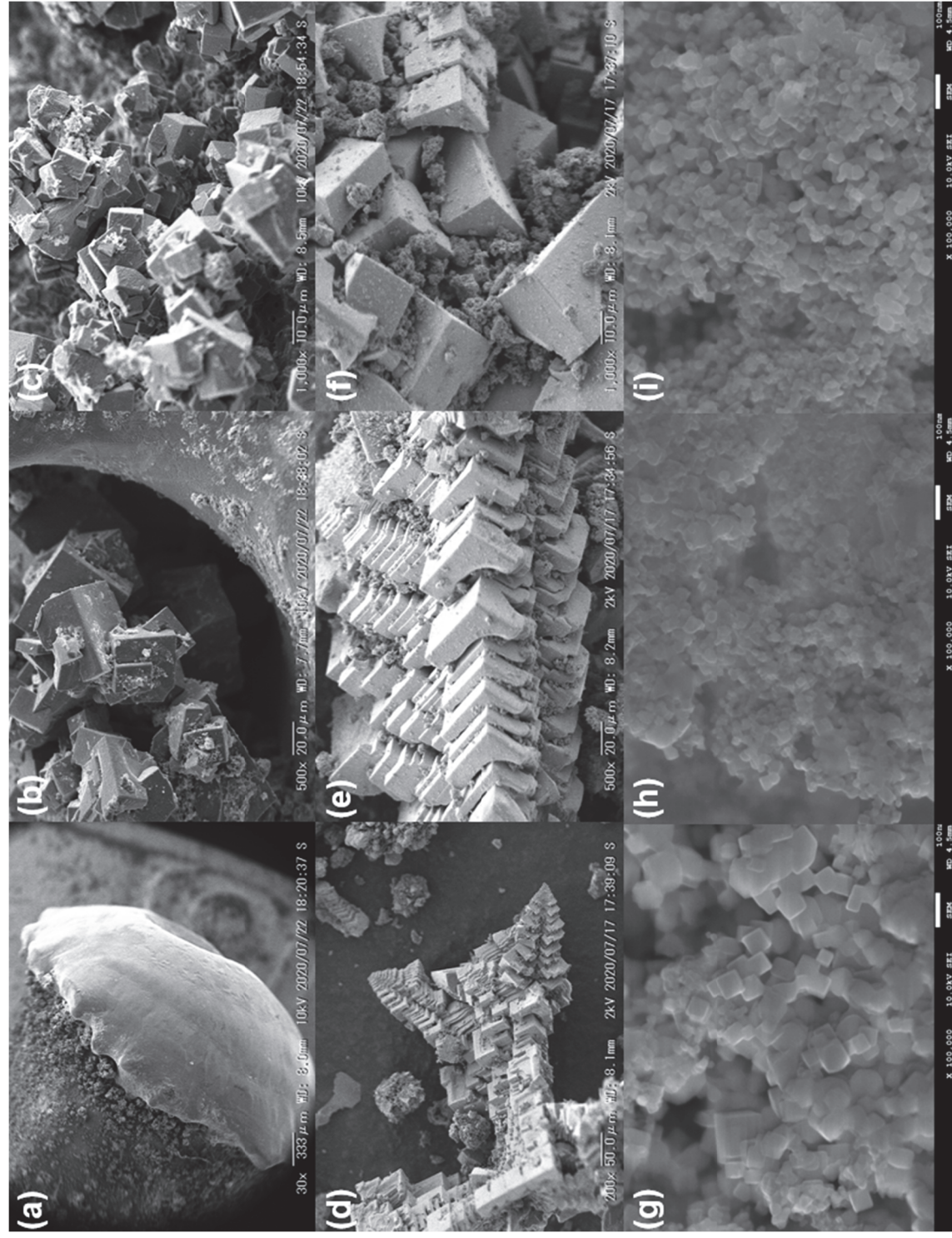


Figure 5-6. Ti particle forming on the anode surface (a), (b), (c), Ti coarse particle (d), (e), (f), and Ti fine particle (g), (h), (i).

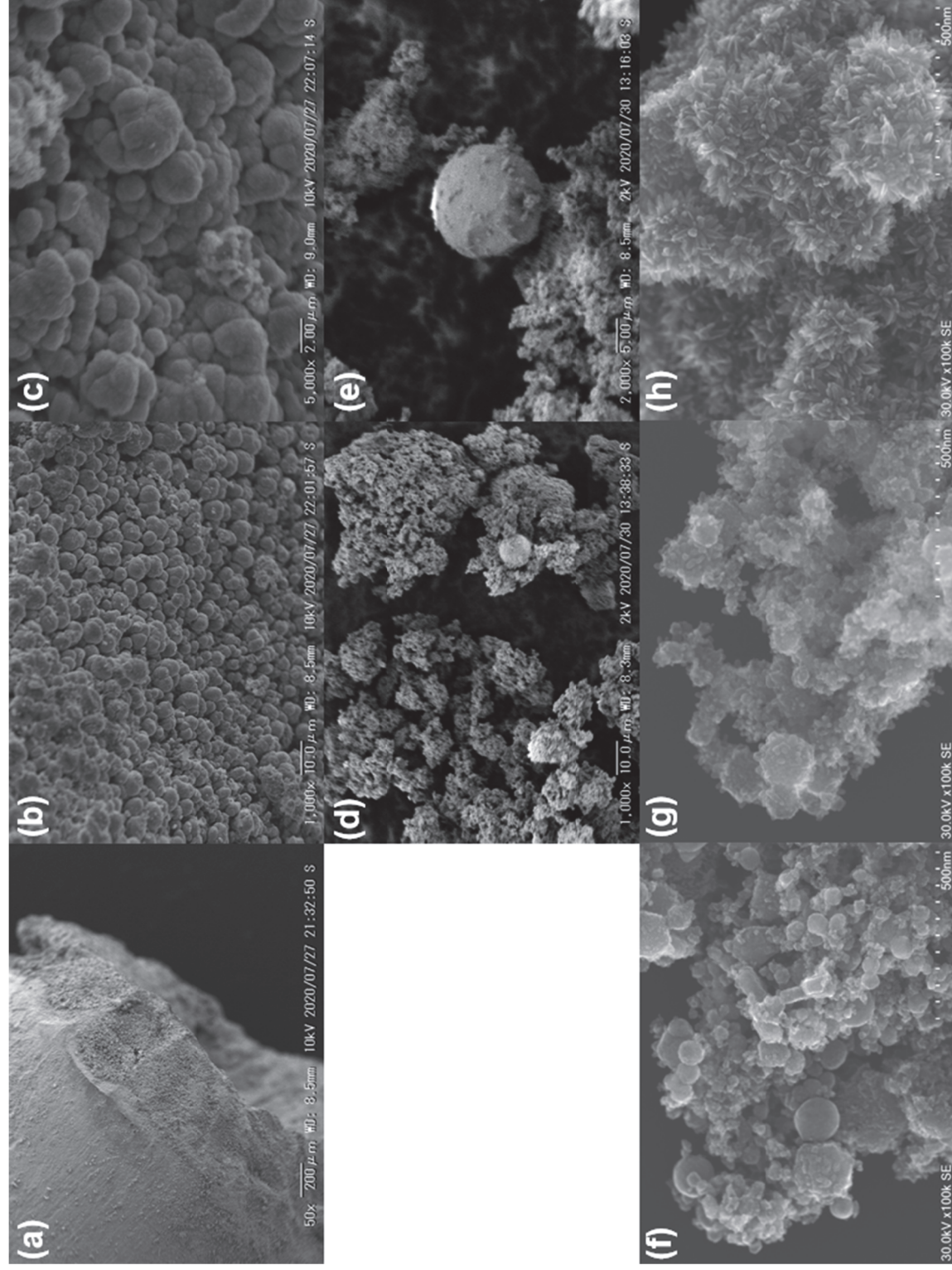


Figure 5-7. Zn particle forming on the anode surface (a), (b), (c), Zn coarse particle (d), (e), and Zn fine particle (f), (g), (h).



## 5.4.2 Formation phenomena of synthesized particles in liquid nitrogen

### discharge

Figure 5–8 and Figure 5–9 depict a proposed mechanism for nitride particle formation and the illustration of the arc discharge process in liquid nitrogen for preparation of the particle. Based on the FE–SEM and XRD results, it is clear that the anode generates the particles in this process. Particles are produced from the heated anode surface by melting and vaporizing the anode material. The arc plasma's temperature is thought to be high enough to melt and evaporate the arc spot at the electrode. When the arc initiates discharge between the electrodes, a specific gas bubble area, as depicted in the white zone in Figure 5–9, is most likely formed between the electrodes. Inside the bubble, there is a lot of nitrogen gas. Because the arc discharge persists in the plasma column, the generated thermion can continuously dissociate nitrogen molecules into atoms as long as the arc discharge persists. Atomic nitrogen can react with Al and Ti metals to form metal nitrides. The SEM observation of the Ti anode surface confirmed this phenomenon. As mentioned it in above, it is thought that the coarse particles were directly derived from the detachment of those micro sizes of cubic dendrites on the electrode during discharge. Once the leached metal vapor was generated, it was rapidly quenched by the surroundings. During the supercooling process, the nucleation proceeds by condensation and formed metal nanoclusters. The dissociated nitrogen atoms also reacted with generated metal nanoclusters to form nitrides. For example, the TiN nanoclusters grew in a cubic crystal. Furthermore, produced TiN primary particles were aggregated by colliding with each other. In Similar, in the DI water case in chapter 2, dissolved oxygen in DI water reacts with copper nanoclusters to form copper oxides. The size of the synthesized metal and metal nitride cluster is considered growing with the Ostwald ripening mechanism. Ostwald ripening is a phenomenon that small crystals or sol particles dissolve and deposit to larger crystals or particles [111]. This process generally leads to a decreased number of particles, coarsening of the particle size [112, 113]. Both Ti and Zn are easy to be oxidized when the samples are exposed to the air. Once the nitrides are formed, TiN does not proceed to be oxidized. Meanwhile,  $Zn_3N_2$  is oxidized when it is exposed to humidity. In all the samples, prepared particles showed the behavior of aggregation and agglomeration.

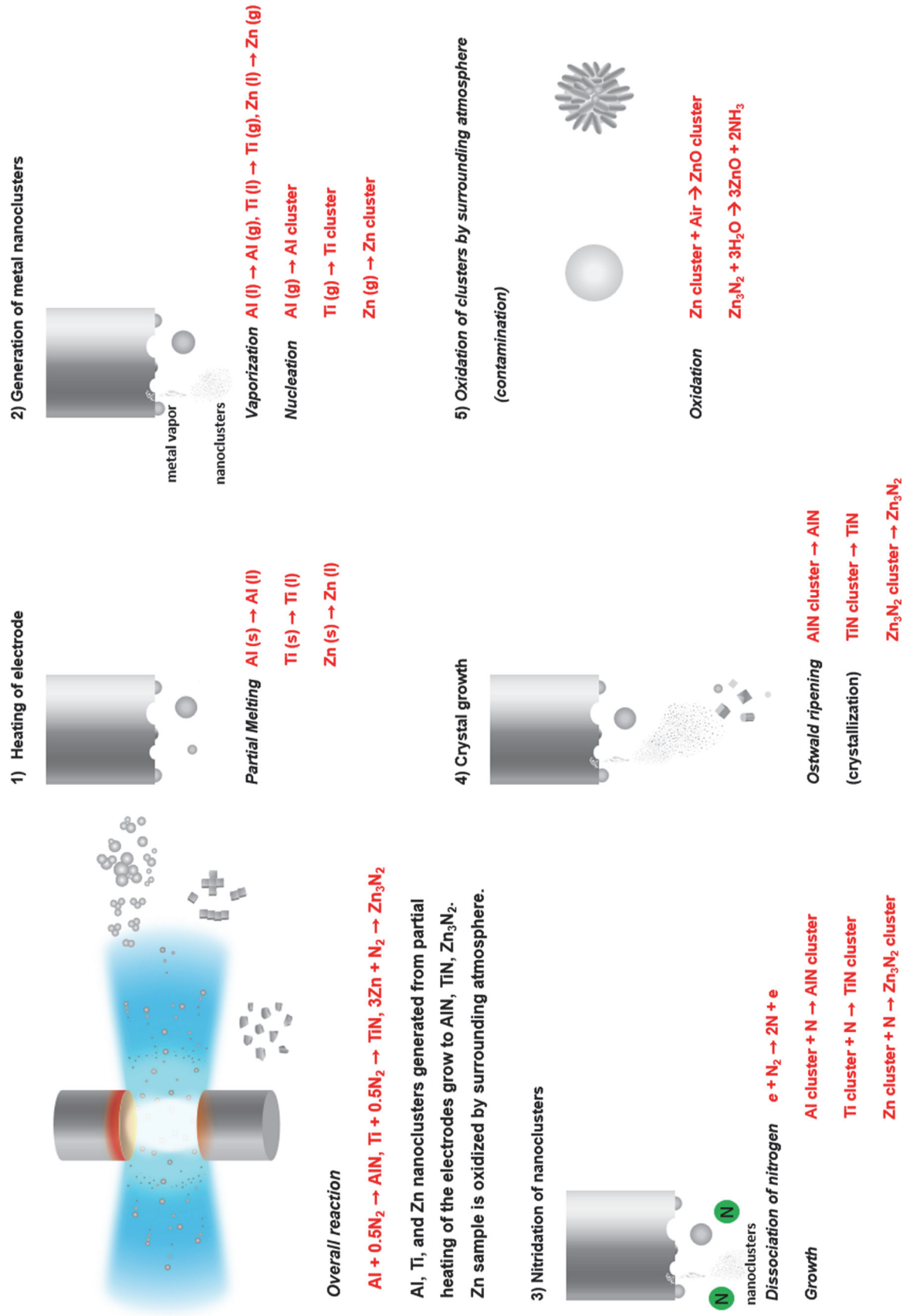
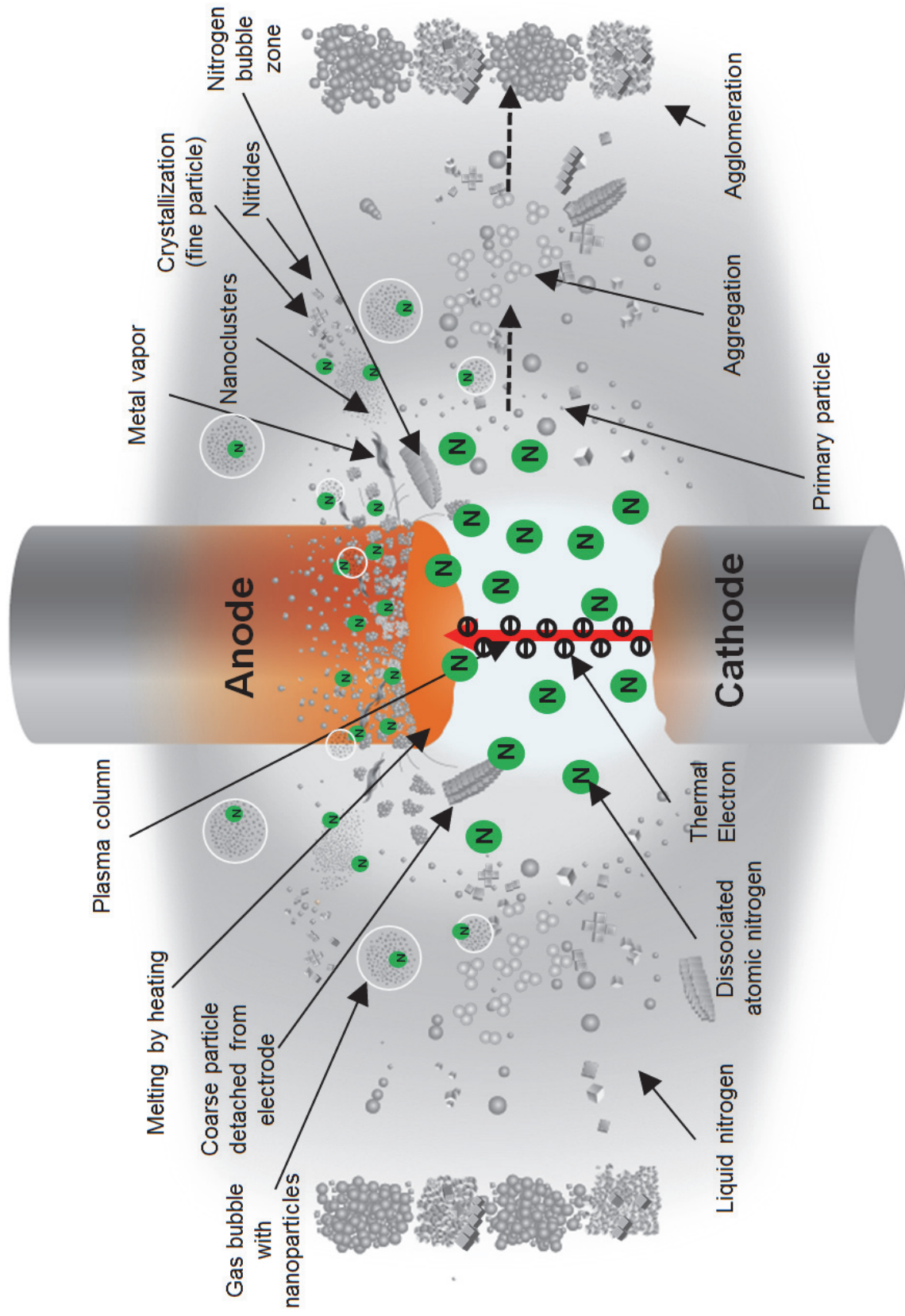


Figure 5-8. Mechanism of the nitride particle formation



**Figure 5-9.** Illustration of the particle formation in the submerged arc discharge process.

## 5.5 Summary

Prior to summing up this chapter, the findings related to the characteristic results of the prepared particle are organized in Table 5–2.

**Table 5–2.** Summary of characteristic observation on prepared particle in this study

	Cu	Al	Ti	Zn
$\Delta G$	n/a	$\Delta G < 0$	$\Delta G < 0$	$\Delta G > 0$
Continuous discharge stability at 30 A condition	unstable	unstable	stable	unstable

In this chapter, the following three things were discussed for the system of particle preparation in liquid nitrogen discharge. At first, the Gibbs standard free energy was calculated to demonstrate the results of the nitride formation depending on electrode material. The calculation revealed that the Al, Ti, and Zn could synthesize nitrides. However, Zn reacts within a very narrow range of temperature around liquid nitrogen.

Next, the continuous arc discharge was discussed, which is considered to be the main parameter for continuous particle production in this process. The work function of the electrode material is relatively compared with the reference of minimum current density for the stable arc discharge. The stability of sustainable arc discharge depends on the thermal properties of the metal electrode, work function, and whether the electrode forming nitride. Ti cathode seems to be the promising candidate for sustaining the stable arc discharge, while Al, Cu, and Zn electrode are not.

Finally, the particle formation mechanism using Al, Ti, and Zn electrode materials was presented. Here, it is supposed that the metal vapor and dissociated atomic nitrogen synthesize the metal nitrides and grows with Ostwald ripening mechanism.



# CHAPTER 6

## Conclusion

## 6.1 Concluding remarks

In this chapter, the conclusions of the present work are remarked. The submerged arc discharge process has been developed for the preparation of the particles. The main objective of this work was to investigate the specific features of the particles prepared by an electrical discharge under liquid nitrogen and to further understanding particle formation phenomena in liquid nitrogen discharge. As a dielectric media, DI water was investigated in chapter 2. The effect of AC, bipolar pulse, DC power supplies on Cu particle generation has been examined in chapter 3. Al, Ti, and Zn electrodes were applied for particle preparation in liquid nitrogen discharge in chapter 4. The particle formation mechanism was discussed in chapter 5.

In Chapter 2, particle preparation in DI water was performed as a comparison study for discharge in liquid nitrogen. The electrical discharge was successfully maintained under deionized water using the bipolar pulse power supply. Nano-size of copper oxide particles were synthesized using a copper electrode as a raw material without any electrolyte. The needle-like and clipped nail-like shapes of the copper oxides are synthesized at low-power mode and high-power mode, respectively. Based on the SEM images of electrode surface and particles, the particle generation mechanism was proposed. At the low-power mode, the obtained fine particles were considered to be generated on the electrode surface, which implies the electrochemical reaction occurs between the water and copper surface. In the high-power mode, both physical and chemical process combined together. In the physical process, the particles were considered to be generated by melting and evaporation of the copper electrode. And the chemical process is same mechanism in low-power mode.

In Chapter 3, the electrical discharge with Cu electrodes was successfully maintained under liquid nitrogen at specific power operating conditions. The micro-size of a spherical metallic copper particle was obtained. While the nano-size of a copper particle seem to be oxidized. Regardless of the variation of the power supplies, there was no significant difference between the prepared particles. The produced particle has a spherical shape in common when discharge occurred in liquid nitrogen. The particle formation mechanism is considered to proceed by local melting and partial vaporization. The micro-size spherical coarse particles may directly be

detached from the molten surface of the electrode. Moreover, the nano-size spherical fine particles could be generated by partial vaporization from the electrode. DC shows excellent performance on particle preparation in this process as compared with AC and bipolar pulse power supply.

In Chapter 4, three kinds of electrodes, Al, Ti, and Zn, were applied for particle preparation in liquid nitrogen discharge using a DC power supply. From the XRD patterns, nitride phases were confirmed in all the conditions using Al, Ti, and Zn electrodes. Moreover, it was confirmed that the experiment variable as an applied current influenced the crystallinity of the synthesized products. In the high current mode, an average particle size of 43 nm cubic TiN, 46 nm spherical Al/AlN were obtained. According to the experimental results of different metal electrode combinations, it was confirmed that anode generates most of the particles in this process. The XRD results showed that the metal alloy was not observed, while the Ti electrode produces TiN particle and the Cu electrode produced Cu particle. It is determined that each of the electrodes performed an independent role without interfering with another electrode in the particle generation. The arc discharge mechanism was also presented.

In Chapter 5, Gibbs' standard free energy was calculated to explain the results of the nitride formation. The thermodynamic calculations indicated that the nitridation of Al and Ti electrodes is spontaneous. In the case of the Zn electrode, the limited range of the temperature near liquid nitrogen temperature is spontaneous. In this study, we learned that the anode produces particles and cathode supplies electrons for arc discharge. For a better understanding of the interaction between discharge and the particle preparation process. The cathode and anode was discussed based on their role in this process. The sustainable stability of the arc discharge behavior was discussed based on thermal properties of the cathode materials. The Ti electrode shows the best stable properties for sustaining the arc discharge during an experiment. According to the SEM observation of anode surface, we found that the particle forming on the anode surface and morphology of the produced particle corresponds to each other. Based on this result, the particle formation mechanism was proposed. Here, we suggest that the metal vapor and dissociated atomic nitrogen synthesize the metal nitrides.

This works presents a point of view on particle preparation using submerged arc discharge in liquid nitrogen. The dielectric media, power supply, and electrode material are important factors for particle preparation formation. In conclusion, a simple process to synthesize metal, metal oxide,

and metal nitride particles were introduced using electrical discharge in liquid nitrogen. This method has the potential for simple preparation process of nitride fine particles.

## 6.2 Recommendations for future studies

The present work is an early step revealing the simple particle preparation process using arc discharge in liquid nitrogen. Therefore, there are still a number of possible directions to extend in order to understand and improve the process. The followings are the recommendations for future works.

- 1) This study considered the effect of several process parameters, including applied voltage, applied current, power supplies, electrode materials. However, we believe that there are several other parameters, such as electrode diameter, electrode shape, electrode configurations, using a bimetal electrode, which can have an impact on the particle formation mechanism.
- 2) The current sampling system can be more improved. In order to prevent the side reaction, several methods could be proceeds. One method is an experiment carried out in a glove box, which is purged in a nitrogen state. Alternatively, we can apply the chemicals to etching the oxide layer of the particle.
- 3) Since the dissociated nitrogen and dissolved oxygen reacts with metal nanoclusters. The different dielectric medium, such as liquid argon can be considered to investigate to see the difference between the liquid nitrogen.
- 4) The different types of electrode raw material can be further investigated to find the promising candidates for synthesize the fine nitride particles.

# REFERENCES

- [1] D.A. Gerdeman and N.L. Hecht, Arc plasma technology in materials science, vol. 3, Springer Science & Business Media, 2012.
- [2] H.K. Choi, Thermal plasmas in chemical processings, Chemical Industry and Technology 6, no. 2 (1988), 176–188.
- [3] Alfred Grill, Cold Plasma Materials Fabrication: From Fundamentals to Applications, 978-0-780-94714-4, John Wiley & Sons, Inc., New York (1994)
- [4] H. Conrads and M. Schmidt, Plasma generation and plasma sources, Plasma Sources Science and Technology 9, no. 4 (2000), 441.
- [5] A.Bogaerts, E.Neyts, R.Gijbels, J.Mullen, Gas discharge plasma and their applications, *Spectrochimica Acta Part B*, **57**, 2002, pp.609–658
- [6] P. H. Yih and V. Saxena, “A review of SiC reactive ion etching in fluorinated plasmas,” *Physica Status Solidi.*, 202 (1997) 605–642.
- [7] P. Pleshko, N. Apperley, L. L. Zimmerman, K. A. Pearson, T. A. Sherk, E. J. St.Pierre, B. Hairabedian, F. Bradney, and R. L. J. Foster: “Design of a plasma flat panel large screen display for high volume manufacture,” *Displays*, 5 (1984) 21–32.
- [8] J. Wilden, J. P. Bergmann and H. Frank: “Plasma transferred arc welding—modeling and experimental optimization,” *J. Therm. Spray Tech.*, 15 (2006) 779–784.
- [9] M.A. Lieberman and A.J. Lichtenberg, Principles of plasma discharges and materials processing, MRS Bulletin 30 (1994), 899–901.
- [10] A.B.Murphy, Plasma destruction of gaseous and liquid wastes, Ann.NY Acad. Sci., 891, 1999, pp.106–123
- [11] H.S.Park, S.J.Kim, Analysis of a plasma melting system for incinerated ash, J.Ind.Eng.Chem. 11, 2005, pp.657–665
- [12] X.Chen, J.M.Badie, G.Flamant, Dynamics of complex chemical system vaporization at high temperature. Application to the vitrification of fly ashes by thermal plasma, *Chem.Eng.Sci.*, **52**, 1997, pp.4381–4391
- [13] M.A.Lieberman, Plasma discharge for material processing and display application in

- Advanced Technologies Based Wave and Beam Generate Plasmas, *NATO Science Series 3 : High technology*, **67**, 1999, pp.1–22
- [14] D.M.Manos, D.L.Flamm, Plasma etching: Introduction, Academic Press, New York, 1989
- [15] H.K.Yasuda, Plasma Polymerization and Plasma Interactions with Polymeric Materials, Wiley, New York, 1990
- [16] Maher I. Boulos, Pierre Fauchais, and Emil Pfender, *Thermal Plasmas: Fundamentals And Applications. Volume I*, 978-0-306-44607-3, Plenum Press, New York (1994) pp 452
- [17] Tetso Iijima, Nobukazu Kondo, Takashi Aoyama, 初めてのプラズマ技術, 978-4-627-78611-0, 森北出版, 2011
- [18] Conrads, H., & Schmidt, M. (2000). Plasma generation and plasma sources. *Plasma Sources Science and Technology*, *9*(4), 441.
- [19] J. Reece Roth, "Industrial Plasma Engineering", Institute of Physics, 1 (1995), 366–404
- [20] S. Horikoshi and N. Serpone. In-liquid plasma: a novel tool in the fabrication of nanomaterials and in the treatment of wastewaters, *RSC Adv.*, 2017, *7*, 47196–47218
- [21] Claire Tendero, Christelle Tixier, Pascal Tristant, Jean Desmaison, Philippe Leprince, Atmospheric pressure plasmas: A review, *Spectrochimica Acta Part B*, *61*, (2006), 2 – 30
- [22] Nagahiro Saito, Maria Antoaneta Bratescu and Kazuo Hashimi, *Solution plasma: A new reaction field for nanomaterials synthesis*, *Jpn. J. Appl. Phys.*, **57**, 2018, 0102A4
- [23] J. S. Clements, M. Sato and R. H. Davis, Preliminary investigation of pre-breakdown phenomena and chemical reactions using a pulsed high-voltage discharge in water, *IEEE Trans. Ind. Appl.*, 1987, IA-23, 224–235.
- [24] T. Namihira, S. Sakai, T. Yamaguchi, K. Yamamoto, C. Yamada, T. Kiyan, T. Sakugawa and S. Katsuki, Electron temperature and electron density of underwater pulsed discharge plasma produced by solid-state pulsedpower generator, *IEEE Trans. Plasma Sci.*, 2007, *35*, 614–618.
- [25] T. Watano, K. Kurosawa and K. Mizuno, Effect of plasmadischarge in water on wire electrode, Aichi center, Indus. Sci. Technol., 2008.
- [26] R. J. Goldston and P. H. Rutherford, Introduction to plasma physics, Taylor & Francis, New York, 1995, ch. 1.
- [27] Ahmad Hamdan, Cedric Noel, Jaafar Ghanbaja and Thierry Belmonte, Comparison of Aluminium Nanostructures Created by Discharges in Various Dielectric Liquids, *Plasma*

Chem Plasma Process (2014) 34:1101–1114

- [28] A. E. Berkowitz and J. L. Walter, Spark erosion: A method for producing rapidly quenched fine powders, *J. Mater. Res.* (1987) 2 (2), 277
- [29] Naveen Beri, Sachin Maheshwari, Chitra Sharma, and Anil Kumar, Technological Advancement in Electrical Discharge Machining with Powder Metallurgy Processed Electrodes: A Review, *Materials and Manufacturing Processes*, (2010) 25, 1186–1197
- [30] G. Eoker, *Electrode components of the arc discharge*, Springer, (1961) 33
- [31] Sung–Il Jo, Byeong–Joo Lee and Goo–Hwan Jeong, Effect of Graphite Electrode Geometry and Combination on Nanocarbon Synthesis using Underwater Discharge Plasma, *J. Korean Inst. Surf. Eng.* (2017) 50, 2, 108
- [32] P Wang, D J Swaffield, P L Lewin and G Chen, Thermal Bubble Behaviour in Liquid Nitrogen between Inclined Plane Electrodes, Annual Report Conference on Electrical Insulation and Dielectric Phenomena, Conference on Electrical Insulation and Dielectric Phenomena, Canada. (2007) 596–599
- [33] Isidor Sauers, Randy James, Alvin Ellis, Enis Tuncer, Georgios Polizos and Marshall Pace, Breakdown in Liquid Nitrogen in the Presence of Thermally Generated Bubbles for Different Electrode Geometries, Annual Report Conference on Electrical Insulation and Dielectric Phenomena, Conference on Electrical Insulation and Dielectric Phenomena, Canada. (2009) 319–322
- [34] G. Saito and T. Akiyama, Nanomaterial Synthesis Using Plasma Generation in Liquid, *Journal of Nanomaterials*, Volume 2015, Article ID 123696
- [35] Q. Chen, J. Li and Y. Li, A review of plasma–liquid interactions for nanomaterial synthesis, *Journal of Physics D: Applied Physics*, Volume 48, 2015, 424005
- [36] R. Wang, S. Zuo, D. Wu, *et al.*, Microplasma-Assisted Synthesis of Colloidal Gold Nanoparticles and Their Use in the Detection of Cardiac Troponin I (cTn-I), *Plasma Processes and Polymers*, Volume 12, 2014, 380
- [37] T. Yan, X. Zhong, A. E. Rider, *et al.*, Microplasma–chemical synthesis and tunable real–time plasmonic responses of alloyed AuAg<sub>1–x</sub> nanoparticles, *Chemical Communications*, Volume 50, 2014, 3144
- [38] D. Mariotti, J. Patel, V. Svrcek, *et al.*, Plasma–Liquid Interactions at Atmospheric Pressure for Nanomaterials Synthesis and Surface Engineering, *Plasma Processes and Polymers*,



Volume 9, 2012, 1074–1085

- [39] X. Z. Huang, X. X. Zhong, Y. Lu, *et al.*, Plasmonic Ag nanoparticles via environment–benign atmospheric microplasma electrochemistry, *Nanotechnology*, Volume 24, 2013, 095604
- [40] I. G. Koo, M. S. Lee, J. H. Shim, *et al.*, Platinum nanoparticles prepared by a plasma–chemical reduction method, *Journal of Materials Chemistry*, Volume 15, 2005, 4125
- [41] Q. Chen, T. Kaneko and R. Hatakeyama, Synthesis of Superfine Ethanol–Soluble CoO Nanoparticles via Discharge Plasma in Liquid, *Applied Physics Express*, Volume 5, 2012, 096201
- [42] S. J. Kim, B.H. Kim and M.C. Chung, The Synthesis of Nickel Nanoparticles by Liquid Phase Plasma Processing, *Journal of Nanoscience and Nanotechnology*, Volume 13, 2013, 1997
- [43] V. S. Burakov, N. A. Savastenko, N. V. Tarasenko, *et al.*, Synthesis of nanoparticles using a pulsed electrical discharge in a liquid, *Journal of Applied Spectroscopy*, Volume 75, 2008, 114
- [44] G. Saito, S. Hosokai and M. Tsubota, *et al.*, Synthesis of copper/copper oxide nanoparticles by solution plasma, *Journal of Applied Physics*, Volume 110, 2011, 023302
- [43] C. Richmonds and R. Mohan Sankaran, Plasma–liquid electrochemistry: Rapid synthesis of colloidal metal nanoparticles by microplasma reduction of aqueous cations, *Applied Physics Letters*, Volume 93, 2008, 131501
- [46] N. Tarasenko, A. Nevar and M. Nedelko, Properties of zinc-oxide nanoparticles synthesized by electrical-discharge technique in liquids, *Physica Status Solidi (a)*, Volume 207, 2010, 2319
- [47] H. Kabbara, C. Noël, J. Ghanbaja, K. Hussein, D. Mariotti, V. Švrček & T. Belmonte, Synthesis of nanocrystals by discharges in liquid nitrogen from Si–Sn sintered electrode, *Scientific Reports*, Volume 5, 2015, 17477
- [48] T. Belmonte, A. Hamdan, F. Kosior, *et al.*, Interaction of discharges with electrode surfaces in dielectric liquids: Application to nanoparticle synthesis, *Journal of Physics D Applied Physics*, Volume 47(22), 2014, 224016
- [49] A. Allagui, E. A. Baranova and R. Wüthrich, Synthesis of Ni and Pt nanomaterials by cathodic contact glow discharge electrolysis in acidic and alkaline media, *Electrochimica Acta*, Volume 93, 2013, 137
- [50] Y. Toriyabe, S. Watanabe, S. Yatsu, T. Shibayama and T. Mizuno, Controlled formation of metallic nanoballs during plasma electrolysis, *Appl. Phys. Lett.*, 2007, 91, 041501.
- [51] Ruoyu Han, Jiawei Wu, Aici Qiu, Weidong Ding, and Yongmin Zhang, Electrical explosions

- of Al, Ti, Fe, Ni, Cu, Nb, Mo, Ag, Ta, W, W–Re, Pt, and Au wires in water: A comparison study, *J. Appl. Phys.* 124, 043302 (2018)
- [52] Elseddik M. Abdelkader, Paul A. Jelliss, Steven W. Buckner, Main group nanoparticle synthesis using electrical explosion of wires, *Nano–Structures & Nano–Objects* 7 (2016) 23–31
- [53] Xin Gao, Pengwan Chen, Xiaoguang Wang, Chunxiao Xu, Qiuzhi Song and Hao Yin, Production of AlN Nanopowders by Electrical Wire Explosion in Liquid Nitrogen, *Materials Science Forum*, Vol. 910, pp 46–51
- [54] C. H. Lo, T. T. Tsung and L. C. Chen, Shape–controlled synthesis of Cu–based nanofluid using submerged arc nanoparticle synthesis system (SANSS), *Journal of Crystal Growth*, Volume 277, 2005, 636
- [55] S. Y. Xie, Z. J. Ma, C. F. Wang, *et al.*, Preparation and self–assembly of copper nanoparticles via discharge of copper rod electrodes in a surfactant solution: a combination of physical and chemical processes, *Journal of Solid State Chemistry*, Volume 177, 2004, 3743
- [56] W. T. Yao, S. H. Yu, Y. Zhou, *et al.*, Formation of Uniform CuO Nanorods by Spontaneous Aggregation: Selective Synthesis of CuO, Cu<sub>2</sub>O, and Cu Nanoparticles by a Solid–Liquid Phase Arc Discharge Process, *The Journal of Physical Chemistry B*, Volume 109, 2005, 14011
- [57] C. M. Du and M. D. Xiao, Cu<sub>2</sub>O nanoparticles synthesis by Microplasma, *Scientific Reports*, Volume 4, 2014, 7339
- [58] P. Pootawang, N. Saito and S. Y. Lee, Discharge time dependence of a solution plasma process for colloidal copper nanoparticle synthesis and particle characteristics, *Nanotechnology*, Volume 24, 2013, 055604
- [59] S Fink, M Noe, V Zwecker<sup>1</sup> and T Leibfried, Lightning impulse breakdown voltage of liquid nitrogen under the influence of heating, 9<sup>th</sup> European Conference on Applied Superconductivity, *Journal of Physics: Conference Series* 234 (2010) 032011
- [60] S. Fink, H.–R. Kim, R. Mueller, M. Noe, and V. Zwecker, AC Breakdown Voltage of Liquid Nitrogen Depending on Gas Bubbles and Pressure, *ICHVE International Conference on High Voltage Engineering and Application*, 2014
- [61] Toshitaka Satsuta, Masashi Hasegawa, Nobumichi Harada and Shigeo Asai, Preparation of Metal Powders Utilizing Electric Discharge in Liquid Nitrogen, *J, Japan, Inst. Metals*, 57, 1993, 3, 296–300

- [62] H. Kabbara, J. Ghanbajaa, C. Noël, T. Belmonte, Synthesis of Cu@ZnO core-shell nanoparticles by spark discharges in liquid nitrogen, *Nano-Structures & Nano-Objects* 10 (2017) 22–29
- [63] Mahmoud Trad, Alexandre Nominé, Cédric Noël, Jaafar Ghanbaja, Malek Tabbal and Thierry Belmonte, Evidence of alloy formation in CoNi nanoparticles synthesized by nanosecond-pulsed discharges in liquid nitrogen, *Plasma Process Polym.* 2020;e1900255
- [64] T Belmonte, H Kabbara, C Noël and R Pflieger, Analysis of Zn I emission lines observed during a spark discharge in liquid nitrogen for zinc nanosheet synthesis, *Plasma Sources Sci. Technol.* 27 (2018) 074004
- [65] H. Kabbara, J. Ghanbaja, C. Noël and T. Belmonte, Nano-objects synthesized from Cu, Ag and Cu<sub>28</sub>Ag<sub>72</sub> electrodes by submerged discharges in liquid nitrogen, *Materials Chemistry and Physics* 217 (2018) 371–378
- [66] Mahmoud Trad, Alexandre Nominé, Natalie Tarasenko, Jaafar Ghanbaja, Cédric Noël, Malek Tabbal, Thierry Belmonte, Synthesis of Ag and Cd nanoparticles by nanosecond-pulsed discharge in liquid nitrogen, *Front. Chem. Sci. Eng.* 2019, 13(2): 360–368
- [67] Levchenko, I.; Bazaka, K.; Baranov, O.; Sankaran, R. M.; Nomine, A.; Belmonte, T; Xu, S. Lightning under water: Diverse reactive environments and evidence of synergistic effects for material treatment and activation. *Appl. Phys. Rev.* **2018**, 5, 021103
- [68] Ahmad Hamdana, Hiba Kabbara, Cédric Noël, Jaafar Ghanbaja, Abdelkrim Redjaimia, Thierry Belmonte, Synthesis of two-dimensional lead sheets by spark discharge in liquid nitrogen, *Particuology*, Volume 40, 2018, 152–159
- [69] Noriaki Sano, Shin-ichiro Ukita, One-step synthesis of Pt-supported carbon nanohorns for fuel cell electrode by arc plasma in liquid nitrogen, *Materials Chemistry and Physics* 99 (2006) 447–450
- [70] T. Charinpanitkul, W. Tanthapanichakoon, N. Sano, Carbon nanostructures synthesized by arc discharge between carbon and iron electrodes in liquid nitrogen, *Current Applied Physics* 9 (2009) 629–632
- [71] M. Cao, C. Hu Y. Wang, *et al.*, A controllable synthetic route to Cu, Cu<sub>2</sub>O, and CuO nanotubes and Nanorods, *Chemical Communications*, Volume 15, 2003, 1884
- [72] G. H. Du and G. Van Tendeloo. Cu(OH)<sub>2</sub> nanowires, CuO nanowires and CuO nanobelts, *Chemical Physics Letters*, Volume 393, 2004, 64

- [73] Y. Cudennec and A. Lecerf, The transformation of  $\text{Cu}(\text{OH})_2$  into  $\text{CuO}$ , revisited, *Solid State Sciences*, Volume 5, 2003, 1471
- [74] Wenwen Dou, Jiajia Wu, Tingyue Gu, Peng Wang and Dun Zhang, Preparation of super-hydrophobic micro-needle  $\text{CuO}$  surface as a barrier against marine atmospheric corrosion, *Corrosion Science* 131 (2018) 156–163
- [75] G Filipi and U Cvelbar, Copper oxide nanowires: a review of growth, *Nanotechnology* 2012 23 194001
- [76] Sengen Anantharaj, Hisashi Sugime and Suguru Noda, Ultrafast Growth of a  $\text{Cu}(\text{OH})_2$ - $\text{CuO}$  Nanoneedle Array on Cu Foil for Methanol Oxidation Electrocatalysis, *ACS Appl. Mater. Interfaces* 2020, 12, 27327–27338
- [77] Feng Xiao, Shaojun Yuan, Bin Liang, Guanqiu Li, Simo Olavi Pehkonen and TieJun Zhang, Superhydrophobic  $\text{CuO}$  nanoneedle-covered copper surfaces for anticorrosion, *J. Mater. Chem. A*, 2015, 3, 4374
- [78] Kittaka Shigeharu and Morimoto Tetsuo, Spherical Particles and Their Surface Properties. III. Formation of Spherical Particles of Metal Oxides by  $\text{O}_2$ - $\text{H}_2$  Flame Fusion, *Bull. Chem. Soc. Jpn.*, 54, 2882–2885 (1981)
- [79] T.I. Barry, R.K. Bayliss, and L.A. Lay, Mixed oxides prepared with an induction plasma torch, *J. Mater. Sci.*, 3, 229 (1968)
- [80] G. Saito, Y. Nakasugi, and T. Akiyama, Excitation temperature of a solution plasma during nanoparticle synthesis, *Journal of Applied Physics*, Volume 116, 2014, 083301
- [81] R. Schlessler, R. Dalmau, D. Zhuang, R. Collazo, Z. Sitar, Crucible materials for growth of aluminum nitride crystal, *J. Cryst. Growth* 281 (2005) 75–80.
- [82] I. M. Watson, “Metal organic vapour phase epitaxy of  $\text{AlN}$ ,  $\text{GaN}$ ,  $\text{InN}$  and their alloys: a key chemical technology for advanced device applications”, *Coord. Chem. Rev.* 257 (2013) 2120–2141.
- [83] M. A. Dubois, P. Muralt, Properties of aluminum nitride thin films for piezoelectric transducers and microwave filter applications, *Appl. Phys. Lett.* 74 (1999) 3032–3034.
- [84] T. Suehiro, N. Hirosaki, K. Komeya, Synthesis and sintering properties of aluminium nitride nanopowder prepared by the gasreduction-nitridation method, *Nanotechnology* 14 (2003) 487–491.
- [85] Pierson, Hugh O., ed. (1996). *Handbook of Refractory Carbides and Nitrides: Properties*,

- characteristics, processing, and applications. William Andrew. p. 193. ISBN 978-0-8155-1392-6 – via Google Books.
- [86] Wang, Wei-E (1996). "Partial thermodynamic properties of the Ti-N system". *Journal of Alloys and Compounds*. 233 (1-2): 89-95.
- [87] Roscoe, H. E.; Schorlemmer, C. (1907) [1878]. *A Treatise on Chemistry: Volume II, The Metals* (4th ed.). London: Macmillan. pp. 650-651. Retrieved 2007-11-01.
- [88] Bloxam, C. L. (1903). *Chemistry, Inorganic and Organic* (9th ed.). Philadelphia: P. Blakiston's Son & Co. p. 380. Retrieved 2007-10-31.
- [89] Lowry, M. T. (1922). *Inorganic Chemistry*. Macmillan. p. 872. Retrieved 2007-11-01.
- [90] Maile, E.; Fischer, R. A. (Oct 2005), "MOCVD of the Cubic Zinc Nitride Phase, Zn<sub>3</sub>N<sub>2</sub>, Using Zn[N(SiMe<sub>3</sub>)<sub>2</sub>]<sub>2</sub> and Ammonia as Precursors", *Chemical Vapor Deposition*, 11 (10): 409-414
- [91] Wonbaek Kim, Je-shin Park, Chang-yul Suh, Sung-wook Cho, Sujeong Lee and In-Jin Shon, Synthesis of TiN Nanoparticles by Explosion of Ti Wire in Nitrogen Gas, *Materials Transactions*, Vol. 50, No. 12 (2009) pp. 2897 to 2899
- [92] Kazuyuki Hokamotoa, Naoyuki Wada, Ryuichi Tomoshige, Shoichiro Kai, Yasuhiro Ujimoto, Synthesis of TiN powders through electrical wire explosion in liquid nitrogen, *Journal of Alloys and Compounds* 485 (2009) 573-576
- [93] Dong Hun Shin, Yong Cheol Hong, and Han Sup Uhm, Production of Nanocrystalline Titanium Nitride Powder by Atmospheric Microwave Plasma Torch in Hydrogen/Nitrogen Gas, *J. Am. Ceram. Soc.*, 88 [10] 2736-2739 (2005)
- [94] H. A. Wriedt and J. L. Murray, The N-Ti (Nitrogen-Titanium) system, *Bull. Alloy Phase Diagrams* 8 (1987) 378-388.
- [95] U. C. Oh and Jung Ho Je, Effects of strain energy on the preferred orientation of TiN thin films, *Journal of Applied Physics* 74, 1692 (1993)
- [96] J P Zhao, X Wang, Z Y Chen, S Q Yang, T S Shi and X H Liu, Overall energy model for preferred growth of TiN films during filtered arc deposition, *J. Phys. D: Appl. Phys.* 1997, 305
- [97] Chuan Jing, Dr. Biqin Dong, Dr. Yuxin Zhang, Chemical Modifications of Layered Double Hydroxides in the Supercapacitor, *Energy Environ. Mater.* 2020, 3, 346-379
- [98] Xiaodong Guo, Quanzhong Zhao, Ruxin Li, Huaihai Pan, Xiaoyang Guo, Anyuan Yin, and Weilin Dai, Synthesis of ZnO nanoflowers and their wettabilities and photocatalytic

- properties, *Optics Express*, Vol. 18, Issue 17, pp. 18401–18406 (2010)
- [99] Ye Zhang, Hongbo Jia, Xuhui Luo, Xihong Chen, Dapeng Yu, and Rongming Wang, Synthesis, Microstructure, and Growth Mechanism of Dendrite ZnO Nanowires, *J. Phys. Chem. B* 2003, 107, 33, 8289–8293
- [100] A Umar, S Lee, Y H Im and Y B Hahn, Flower-shaped ZnO nanostructures obtained by cyclic feeding chemical vapour deposition: structural and optical properties, *Nanotechnology*, Volume 16, Number 10 2462
- [101] Ushio, M. Arc discharge and electrode phenomena, *Pure & Appl. Chem.* **1988**, 60, 5, 809–814
- [102] Crowell, C.R. The Richardson constant for thermionic emission in Schottky barrier diodes, *Solid-State Electron.* **1965**, 8, 395–399
- [103] Koeck, F.A.M.; Nemanich, R.J. Low temperature onset for thermionic emitters based on nitrogen incorporated UNCD films, *Diam. Relat. Mater.* **2009**, 18, 232–234
- [104] Dilip, K.D.; Olukunle, C.O. Modified Richardson–Dushman equation and modeling thermionic emission from monolayer graphene, *Proceedings Volume 9927*, Nanoengineering: Fabrication, Properties, Optics, and Devices XIII; 99270E, San Diego, United States, 15 September 2016
- [105] David, R. L. Section 12: Properties of solids, Electron work function of the elements. In *Handbook of Chemistry and Physics, 89th ed.*; CRC press: Boca Raton, Florida, USA, 2008; pp. 12–124.
- [106] Wolf, B. Handbook of ion sources. CRC Press, 1995. ISBN 0849325021, 9780849325021. p.27,11
- [107] Smithells, J.C.J. 18 Electron emission, In. *Metals Reference Book, 7th ed.*; Butterworth-Heinemann, London, 1967, 737ff.
- [108] Michaelson, H.B. The work function of the elements and its periodicity. *J. Appl. Phys.* 1977, 48, 4729
- [109] Patsalas, P.; Kalfagiannis, N.; Kassavetis, S.; Abadias, G.; Bellas, D.V.; Lekka, Ch.; Lidorikis, E. Conductive nitrides: Growth principles, optical and electronic properties, and their perspectives in photonics and plasmonics. *Mater. Sci. Eng. R Rep.* 2018, 123, 1-55
- [110] Mezzi, A.; Soltani, P.; Kaciulis, S.; Bellucci, A.; Girolami, M.; Mastellone, M.; Trucchi, D.M. Investigation of work function and chemical composition of thin films of borides and

- nitrides. *Surf Interface Anal.* 2018, 50, 1138-1144
- [111] MCNAUGHT, A. D. & MCNAUGHT, A. D. 1997. *Compendium of chemical terminology*, Blackwell Science Oxford.
- [112] MOKARI, T., SZTRUM, C. G., SALANT, A., RABANI, E. & BANIN, U. 2005. Formation of asymmetric one-sided metal-tipped semiconductor nanocrystal dots and rods. *Nature Materials*, 4, 855–863.
- [113] HORNYAK, G. L., DUTTA, J., TIBBALS, H. F. & RAO, A. 2011. *Introduction to nanoscience*, CRC Press.

# Acknowledgements

First of all, I would like to express my gratitude to my supervisor, Professor Hidetoshi Sekiguchi, for giving me the opportunity to experience and studying in Japan and research in his laboratory. And deeply appreciate his patience in waiting for me a long journey to finish my doctoral thesis.

Next, I am very thankful to Assistant Professor Satoshi Kodama for helping me design the electrode holder using a milling machine.

I appreciate Professor Masatoshi Kubouchi, Professor Yusuke Shimoyama, Associate Professor Shinsuke Mori, and Associate Professor Saiko Aoki for examining my thesis and giving me valuable comments. Especially for Professor Masatoshi Kubouchi and Associate Professor Shinsuke Mori, I really appreciate lending me a liquid nitrogen container and giving me a warm greeting whenever we met.

During the work on my thesis, I really appreciate Nada and Boom, who were supporting and helping me with the research even if the topic was completely different from theirs. Besides, I would like to thank all members of the Sekiguchi laboratory for having me with kindness. And I really appreciate Dr. Dong-Wook Kim for having a fruitful discussion with me in the initial stage of my study.

In addition, I would like to acknowledge the ‘Tatsunoko foundation (竜の子財団)’ for financial support during my doctoral course study.

Finally, I would like to give my sincere love to my family and all of my friends who believed in me and always keep supporting me on my side.